UNIVERSITY UTRECHT

Measurement of Higgs effective coupling parameters in the ggF production and $W^{\pm}W^{\mp *} \rightarrow l^{-}\bar{\nu}_{l}l'^{+}\nu_{l'}$ decay mode at $\sqrt{s} = 13$ TeV with the ATLAS Experiment

by

P.J. Verschuuren

A thesis submitted in fulfillment for the
degree of Master of Science

in the
Faculty of Science
Department of Physics

August 2018

Declaration of Authorship

I, Pim Jordi Verschuuren, declare that this thesis titled, 'Measurement of Higgs effective coupling parameters in the ggF production and $W^{\pm}W^{\mp *} \to l^{-}\bar{\nu}_{l}l'^{+}\nu_{l'}$ decay mode at $\sqrt{s} = 13$ TeV with the ATLAS Experiment' and the work presented in it are my own. I confirm that:

- This work was done wholly or mainly while in candidature for a research degree at this University.
- Where any part of this thesis has previously been submitted for a degree or any other qualification at this University or any other institution, this has been clearly stated.
- Where I have consulted the published work of others, this is always clearly attributed.
- Where I have quoted from the work of others, the source is always given. With the exception of such quotations, this thesis is entirely my own work.
- I have acknowledged all main sources of help.
- Where the thesis is based on work done by myself jointly with others, I have made clear exactly what was done by others and what I have contributed myself.

Signed: ____

Date: ____

“I… a universe of atoms, an atom in the universe’

Richard Feynman

UNIVERSITY UTRECHT

Abstract

Faculty of Science
Department of Physics

Master of Science

by P.J. Verschuuren

This thesis presents and discusses measurement of effective field theory couplings of the Higgs boson to weak vector bosons. The analysis uses data collected during the LHC Run 2 data taken at $\sqrt{s} = 13$ TeV by the ATLAS detector corresponding to a total integrated luminosity of 36.07 fb^{-1}. The measurement focuses on the gluon fusion production mode, targeting $H \to W^{\pm}W^{\mp *} \to l^{-}\bar{\nu}_{l}l'^{+}\nu_{l'}$ decays. The SM Higgs boson observed signal strength was measured as $\mu = 1.258^{+0.208}_{-0.200}$ with an observed and expected significance of $Z_{\text{obs.}} = 6.6\sigma$ and $Z_{\text{exp.}} = 5.3\sigma$.[1] With the use of an Effective Lagrangian Morphing interpolation technique a CP-even and a CP-odd Higgs to W boson effective coupling parameter was measured. Both the signal strength and effective coupling parameter measurement show no significant deviation from the Standard Model.

Acknowledgements

I would like to thank prof. dr. Wouter Verkerke for the opportunity to contribute to the research of the ATLAS group of Nikhef. It has been a great experience to work with its group of distinguished physicists and get to know the science community of the CERN.

I would like to thank my supervisor dr. Carsten Burgard for his great guidance throughout my research. Textbooks and papers go a long way but were nearly not as valuable as his direct teachings and advice. Not only in physics and research but also his technical skills showed him as an extremely capable physicist from which I learned a lot.

Special thanks for Adam Kaluza and Ralf Gugel for their help with the use of the Effective Lagrangian Morphing code and Common Analysis Framework. Their help made these complex frameworks manageable.

Special thanks to prof. dr. Eric Laenen for the sparring sessions on Quantum Field Theory concepts. The discussions made it possible for me to get a grasp on the theory and connect it with measurement.

Thanks to the rest of the ATLAS group at Nikhef for their discussions on topics such statistics, programming, particle detection and theory. The sharing of a common passion for particle physics set a great working environment and have made my project very enjoyable.

Lastly, I want to thank my parents as they have always supported me in my studies and related endeavours. They are given full credit for how far I have come and remain indispensable throughout my work.

Contents

Declaration of Authorship i

Abstract iii

Acknowledgements iv

List of Figures viii

List of Tables xi

Abbreviations xii

Physical Constants xiv

Symbols xv

1 Introduction 1

2 Theoretical Framework 4
- 2.1 The Standard Model of Particle Physics . . . 5
- 2.2 Lagrangian formalism . . . 6
  - 2.2.1 Principle of Least Action . . . 7
  - 2.2.2 Path Integrals in Quantum Mechanics . . . 7
  - 2.2.3 Free Scalar Field Theory . . . 9
  - 2.2.4 Perturbation Theory . . . 12
- 2.3 Gauge Symmetries . . . 15
- 2.4 Brout-Englert-Higgs mechanism . . . 20
- 2.5 Cross section and Luminosity . . . 25
- 2.6 Effective Field Theory . . . 26
  - 2.6.1 Fermi theory . . . 27
  - 2.6.2 Higgs Characterization Model . . . 29
  - 2.6.3 Effective Lagrangian Morphing . . . 30
- 2.7 Beyond the Standard Model . . . 32
  - 2.7.1 Issues of the Standard Model . . . 32
  - 2.7.2 Higgs Sector Extensions . . . 34

3 Large Hadron Collider and ATLAS detector 36
- 3.1 Large Hadron Collider 37
- 3.2 The ATLAS detector 38
  - 3.2.1 Inner Detector 39
  - 3.2.2 Calorimeters 41
  - 3.2.3 Muon Spectrometer 42
  - 3.2.4 Magnet System 44
- 3.3 Trigger system of ATLAS 44
- 3.4 Monte Carlo Generators & Simulation 45
  - 3.4.1 Monte Carlo Event Generation 45
  - 3.4.2 ATLAS Detector Simulation 47

4 Object Reconstruction and Particle Identification 48
- 4.1 Tracks and Vertices 48
  - 4.1.1 Track Reconstruction 48
  - 4.1.2 Primary Vertex Reconstruction 50
- 4.2 Electrons and Photons 51
- 4.3 Muons 52
- 4.4 Jets 53
- 4.5 Taus 54
- 4.6 Missing Transverse Energy 55

5 Higgs Physics at the LHC 57
- 5.1 Production Modes 57
- 5.2 Decay Modes 59
- 5.3 Higgs Properties 61
  - 5.3.1 Signal Strength 61
  - 5.3.2 EFT Couplings 62

6 Signal Strength Analysis 65
- 6.1 Data and Monte Carlo Samples 65
  - 6.1.1 Signal Samples 65
  - 6.1.2 Background Samples 66
- 6.2 Object Selection 66
  - 6.2.1 Electrons 67
  - 6.2.2 Muons 67
  - 6.2.3 Jets 67
- 6.3 Event Selection 68
  - 6.3.1 Pre-selection 68
  - 6.3.2 Signal Region 69
  - 6.3.3 Control and Validation 70
- 6.4 Uncertainty Treatment 73
  - 6.4.1 Experimental Uncertainty 73
  - 6.4.2 Theoretical Uncertainty 73
- 6.5 Signal Measurement 73
  - 6.5.1 Maximum-likelihood estimator $\hat{\mu}$ 74
  - 6.5.2 Significance 75

6.5.3 Results . . . 76

7 EFT Coupling Analysis **77**
7.1 Modeling at the LHC . . . 77
7.1.1 Matrix Element Reweighting . . . 78
7.1.2 Vertical Morphing . . . 79
7.1.3 Moment Morphing . . . 80
7.2 Effective Lagrangian Morphing . . . 81
7.2.1 A Simple Showcase . . . 82
7.3 Experimental Strategy . . . 84
7.4 Base and Validation Samples . . . 84
7.5 Base Sample Optimization . . . 86
7.6 Results . . . 89

8 Conclusions and Outlook **94**
8.1 Signal Strength Analysis . . . 94
8.2 EFT Coupling Analysis . . . 94

A Theoretical Derivations **96**
A.1 Free Scalar Field Generating Functional . . . 96
A.2 Wick's Theorem . . . 97
A.3 Vector Boson Masses . . . 98

B Optimization Plots **100**

C Signal Region Fit Distributions **102**

D Validation Plots **105**

E Cut Flow **106**
E.1 Signal Strength Signal Cut Flow . . . 106
E.2 EFT Coupling Signal Cut Flow . . . 106
E.3 Shared Background Cut Flow . . . 106

Bibliography **108**

List of Figures

2.1 The Standard Model of Particle Physics[2] 6
2.2 Different paths through configuration space. The red line indicates the path for which $\delta S = 0$[3] 8
2.3 Feynman diagram of a Feynman propagator representing a particle creation and destruction 11
2.4 Feynman diagrams of a 4-point correlation function representing all possible particle creations and destructions 12
2.5 Feynman diagrams of a 4-point correlation function representing all possible particle creations and destructions including self-interactions. The first entails one of the free scalar correlation functions, the second introduces a loop interaction and the third a 4-point interaction 14
2.6 The leading order contributions to the amplitude of the $W^{\pm}W^{\mp} \to W^{\pm}W^{\mp}$[4] 22
2.7 β-decay mediated by a W-boson as described by electroweak theory . . . 27
2.8 β-decay contracted to a 4-point interaction as described by Fermi theory . 28

3.1 The CERN accelerator complex[5] 38
3.2 Schematic of the ATLAS detector[6] 39
3.3 Schematic of the Inner Detector[6] 40
3.4 Schematic of the Inner Detector cross section[7] 41
3.5 Schematic of the calorimeter system[8] 42
3.6 Schematic of the Muon spectrometer[9] 43
3.7 Schematic of the magnet system of the ATLAS detector[10] 44
3.8 Overview of ATLAS LHC Computing Grid CPU[left] and disk[right] usage.[11] 47

4.1 Illustration of (left) single-particle pixel clusters and (right) a merged pixel cluster due to very collimated charged particles. The colours indicate energy deposits of different charged particles.[12] 49
4.2 Schematic of vertex topologies during a proton-proton bunch crossing.[13] 51

5.1 Leading order Feynmann diagrams for the dominant production modes at the LHC. a) Gluon fusion b) Vector boson fusion c) Higgs-strahlung d-f) Associated production with top or bottom quarks [14]. 58
5.2 Theoretical predictions on Standard Model Higgs boson production cross sections including uncertainty [14]. 59
5.3 Theoretical predictions branching ratios for Standard Model Higgs boson decay modes including uncertainty [14]. 60

5.4 Results for the production (left) and decay (right) signal strengths from the combination of ATLAS and CMS. The results for each experiment are superimposed. The error bars indicate the 1σ (thick lines) and 2σ (thin lines) intervals. [15]. . . . 61
5.5 Observed (solid black line) and SM expected (dashed blue line) negative log-likelihood scans for (a) κ_{Agg}, (b) κ_{HVV} and (c) κ_{AVV} coupling parameters using 36.1 fb^1 of data at $\sqrt{s} = 13$ TeV. The horizontal lines indicate the value of the profile likelihood ratio corresponding to the 68% and 95% CL intervals for the parameter of interest[16]. . . . 63
5.6 Observed (black) and SM expected (blue) contours of the two-dimensional negative log-likelihood at 95% CL for the κ_{HVV} and κ_{AVV} coupling parameters with 36.1 fb^1 of data at $\sqrt{s} = 13$ TeV. The coupling κ_{Hgg} is fixed to the SM value of one in the fit. The coupling κ_{SM} is (a) fixed to the SM value of one or (b) left as a free parameter of the fit (b).[16]. . . . 63
5.7 The sensitivity obtained in this analysis for the parameter scan of (a) $\cos\alpha$ with an Asimov dataset created for the SM CP even Higgs boson, (b) $\cos\alpha$ with an Asimov dataset created for a CP mixed Higgs boson and (c) the ratio $\frac{\kappa_{Agg}}{\kappa_{Hgg}}\tan\alpha$ for an Asimov dataset created for the SM CP even Higgs boson. The green lines indicate the 1σ confidence interval and the blue lines indicate the 2σ confidence interval.[17] . . . 64

6.1 Distributions of the transverse mass for $N_{jet} = 0$(left) and $N_{jet} = 1$(right) after signal selection criteria are applied (See table 6.2). . . . 70
6.2 Distributions of the transverse mass for $N_{jet} = 0$(left) and $N_{jet} = 1$(right) after control selection criteria are applied (See table 6.4) for $q\bar{q}/gg \rightarrow WW \rightarrow l\nu l\nu$ background normalization. . . . 71
6.3 Distributions of the transverse mass for $N_{jet} = 0$(left) and $N_{jet} = 1$(right) after control selection criteria are applied (See table 6.4) for $Z \rightarrow \tau\tau$ background normalization. . . . 71
6.4 Distributions of the transverse mass for $N_{jet} = 0$(left) and $N_{jet} = 1$(right) after control selection criteria are applied (See table 6.4) for $t\bar{t}$ leptonic background normalization. . . . 71
6.5 Scan of the logarithmic difference between a fixed signal strength value(x-axis) and the unconditional likelihood fit value. Shown are the curves corresponding to fits on the observed data (red) and the expected asimov data(green) representing the Standard Model prediction of $\mu = 1$. . . . 76

7.1 A likelihood function for two parameters of interest g_{SM} and g_{BSM}. The likelihood can be minimized by evaluating it for a discrete set of samples (left) or with a continuous likelihood function based on a discrete set of samples (right). [18]. . . . 78
7.2 An example of morphing between two samples of which the PDF is a normal distribution. The statistical moments change for different values for some parameter m. The morphing result is given for both the vertical and the moment morphing [19]. . . . 80
7.3 A graphical depiction of Effective Lagrangian Morphing in a simple showcase [20]. . . . 83
7.4 Parameter configuration overview of the initial base and validation samples. 86
7.5 Morphing result and relative uncertainty before optimization . . . 88

7.6 Morphing result and relative uncertainty after one optimization 88
7.7 Morphing result and relative uncertainty after two optimizations 88
7.8 Morphing result and relative uncertainty after three optimizations 89
7.9 Contour plot of the expected SM two-dimensional negative log-likelihood scan for the κ_{HWW} and κ_{AWW} coupling parameters. 91
7.10 Contour plot of the observed two-dimensional negative log-likelihood scan for the κ_{HWW} and κ_{AWW} coupling parameters. 91
7.11 Surface plot of the expected SM two-dimensional negative log-likelihood scan for the κ_{HWW} and κ_{AWW} coupling parameters. 92
7.12 Surface plot of the observed two-dimensional negative log-likelihood scan for the κ_{HWW} and κ_{AWW} coupling parameters. 92
7.13 Observed (red) and expected SM (green) one-dimensional negative log-likelihood scan for the κ_{AWW} coupling parameter. 93
7.14 Observed (red) and expected SM (green) one-dimensional negative log-likelihood scan for the κ_{HWW} coupling parameter. 93

B.1 Morphing result and relative uncertainty after three optimizations 100
B.2 Morphing result and relative uncertainty after three optimizations 100
B.3 Morphing result and relative uncertainty after three optimizations 101
B.4 Morphing result and relative uncertainty after three optimizations 101

C.1 Fit distributions of signal region 1(left) and 2(right) as defined in table 6.3 for $N_{jet} = 0$ 102
C.2 Fit distributions of signal region 3(left) and 4(right) as defined in table 6.3 for $N_{jet} = 0$ 102
C.3 Fit distributions of signal region 5(left) and 6(right) as defined in table 6.3 for $N_{jet} = 0$ 103
C.4 Fit distributions of signal region 7(left) and 8(right) as defined in table 6.3 for $N_{jet} = 0$ 103
C.5 Fit distributions of signal region 1(left) and 2(right) as defined in table 6.3 for $N_{jet} = 1$ 103
C.6 Fit distributions of signal region 3(left) and 4(right) as defined in table 6.3 for $N_{jet} = 1$ 104
C.7 Fit distributions of signal region 5(left) and 6(right) as defined in table 6.3 for $N_{jet} = 1$ 104
C.8 Fit distributions of signal region 7(left) and 8(right) as defined in table 6.3 for $N_{jet} = 1$ 104

D.1 Validation plots for the base samples in signal region 3 as defined in table 6.3 for $N_{jet} = 1$ 105
D.2 Validation plots for the base samples in signal region 3 as defined in table 6.3 for $N_{jet} = 1$ 105

E.1 Cut flow of the signal samples of the signal strength analysis 106
E.2 Cut flow of the signal samples of the EFT coupling analysis 107
E.3 Cut flow of the background samples 107

List of Tables

2.1 Classification and properties of the Standard Model fermions in the $SU(2)_L$-representation 18

2.2 Values in units of v taken in by the couplings $g_{Xyy'}$ with $C = \sqrt{\frac{\alpha_{EM} G_F m_Z^2}{8\sqrt{2}\pi}}$[21] 30

5.1 Best fit values for the coupling parameters κ_{Agg}, κ_{AVV} and κ_{HVV} as obtained from the negative log likelihood scans performed with 36.1 fb^{-1} of data at $\sqrt{s} = 13$ TeV collected at the ATLAS experiment.[16] 62

6.1 Included signal and background processes, corresponding Monte Carlo generators, cross sections and precisions 66

6.2 Event selection criteria for the two signal region categories 69

6.3 Signal regions for both jet categories that are used in the likelihood fit. . 69

6.4 Event selection criteria used to define the control regions 70

6.5 Summary of experimental systematic uncertainties used in this analysis . 72

6.6 Summary of theoretical systematic uncertainties used in this analysis . . . 72

7.1 Values of the coupling parameters for the base and validation samples . . 85

7.2 The impact of the optimization on the relative uncertainty in terms of the average and the lowest of the whole parameter range. 89

7.3 Maximum likelihood estimators of the two-dimensional likelihood scans for the coupling parameters κ_{AWW} and κ_{HWW} for both observed and Asimov data. 90

Abbreviations

SM	**S**tandard **M**odel
BSM	**B**eyond **S**tandard **M**odel
LO	**L**eading **O**rder
NLO	**N**ext-to-**L**eading **O**rder
QED	**Q**uantum **E**lectro**D**ynamics
QCD	**Q**uantum **C**hromo**D**ynamics
BEH	**B**rout **E**nglebert **H**iggs
VEV	**V**acuum **E**expectation **V**alue
LHC	**L**arge **H**adron **C**ollider
CoM	**C**enter-**o**f-**M**ass
QFT	**Q**uantum **F**ield **T**heory
EFT	**E**ffective **F**ield **T**heory
CERN	**C**onseil **E**uropeen pour la **R**echerche **N**ucleaire
ATLAS	**A** **L**arge **T**oroidal **L**HC **A**pparatu**S**
LINEAC	**LINE**ar **AC**celerator
PS	**P**roton **S**ynchrotron
SPS	**S**uper **P**roton **S**ynchrotron
ID	**I**nner **D**etector
IBL	**I**sertable **B**-**L**ayer
PD	**P**ixel **D**etector
SCT	**S**emi**C**onductor **T**racker
TRT	**T**ransition **R**adiation **T**racker
ECAL	**E**lectromagnetic **CAL**orimeter
HCAL	**H**adronic **CAL**orimeter
MS	**M**uon **S**pectrometer

MDT	**M**uon **D**rift **T**ube
CS	**C**athode **S**trip
TG	**T**hin **G**ap
L1T	**L**evel-**1** **T**rigger
HLT	**H**igh-**L**evel **T**rigger
NEWT	**NEW** **T**racking
CCA	**C**onnected **C**omponent **A**nalysis
RoI	**R**egion **o**f **I**nterest
GSF	**G**aussian **S**um **F**ilter
BDT	**B**oosted **D**ecision **T**ree
MET	**M**issing transverse energy($\boldsymbol{E_T}$)
SR	**S**ignal **R**egion
CR	**C**ontrol **R**egion
VR	**V**alidation **R**egion
PDF	**P**robability **D**istribution **F**unction
PoI	**P**arameter **o**f **I**nterest
NP	**N**uisance **P**arameter
MC	**M**onte **C**arlo
TOE	**T**heory **O**f **E**verything
GUT	**G**rand **U**nified **T**heory

Physical Constants

Speed of Light $c = 2.997\ 924\ 58 \times 10^{8}$ ms$^{-\mathrm{S}}$

Planck constant $h = 6.62606957(29) \times 10^{34}$ J s

Planck constant, reduced $\hbar \equiv h/2\pi = 1.054571726(47) \times 10^{34}$ J s

Electron charge magnitude $e = 1.602176565(35) \times 10^{19}$ C

Fine-structure constant $\alpha = \frac{e^2}{4\pi\eta_0\hbar c} = 7.2973525698(24) \times 10^{3}$

Fermi coupling constant $G_F/(\hbar c)^3 = 1.1663787(6) \times 10^{5}$ GeV^{-2}

Weak-mixing angle $\sin^2\theta(M_Z) = 0.231\ 26(5)$

$W^{\pm}$ boson mass $m_W = 80.385(15)$ GeV/c^2

Z^0 boson mass $m_Z = 91.1876(21)$ GeV/c^2

Strong coupling constant $\alpha_S(m_Z) = 0.1185(6)$

Symbols

L	Lagrangian
$\mathcal{L}$	Lagrangian Density
∂_μ	Covaiant derivative
$\square$	d'Alembert operator
k	Wavenumber
m	mass
ψ	Spinor field
phi	Scalar field/azimuthal angle
I_3	Weak isospin
Y_W	Weak hypercharge
Q	Electric charge
$\mathcal{M}$	Matrix element
σ	cross section
$\sqrt{s}$	Center of mass energy
p_T	Transverse momentum
E_T^{miss}	Missing transverse momentum
κ	Coupling modifier

For/Dedicated to/To my…

Chapter 1

Introduction

Science has taken on an increasingly important role in our current society. It has been incorporated in industry, health care, technology and has even influenced the way we think over the past decades. With this entwinement of science and society it is easy to see the pragmatic motivations of fundamental research. However, if particle physicists are asked if they do what they do for the practical use they will almost definitely say no. It is because of their curiosity for the fundamental workings of nature and passion for exploring the unknown that makes particle physicists very driven scientists and brought us to the point of understanding at which we are now.

The well-known philosophers of Ancient Greece such as Aristoteles, Plato and Archimedes made one of the first attempts to describe the nature of the world around us. The many different ideas and philosophies resulted in a broad variety of ”scientific” findings that were not always accurate. However, a good basis for a scientific method was formed which survived the intellectual low of the dark ages and continued its development again during the Renaissance. In the 1700’s science became the systematic study based on observation and experiment as we know it today and resulted in an outburst of scientific discoveries.

Many of these scientific discoveries were made in physics but any form of particle physics was still unknown to the scientific community. Even though the concept of the atom can be traced back to 400 B.C., it is only in the early 1900’s that modern particle physics took shape. Quantum theory emerged and together with an increase in technological innovation gave access to a new view on the microscopic world. Particle accelerators made it possible to probe further than the nuclei and eventually gave rise to the status quo of modern particle physics, the Standard Model.

During the second half of the 20th century the Standard Model gained support from the scientific community after more measurements seemed to agree with it. Eventually it showed to be an elegant and accurate description of nature on its smallest scales but was incomplete up until only recently. Pressing problems of the Standard Model such as the origin of mass were only solved with the introduction of a new particle, the Higgs boson.[22, 23] It seems with the discovery(2012) and confirmation(2013) of a new particle fitting the Higgs profile that the last piece of the puzzle has been found.

However, as finalizing this may sound, the Standard Model including the Higgs boson still leaves a lot of questions unanswered. The first denotes the clash between the very small and the very large scale physics. General relativity(GR) describes how the fundamental interaction of gravity can be described by the geometric properties of space and time. However, when one tries to reconcile the concepts of GR with quantum mechanics the resulting theory becomes non-renormalizable, a necessity in quantum theories to get physical predictions.[24] Several quantum gravity theories that pose a solution for this problem are string theory[25] and loop quantum gravity[26] but remain experimentally unproven until this day.

Another issue addresses the fact that from all the energy in our universe, less than 5% is ordinary matter. Roughly 27% of the universe is made up from dark matter and about 68% from dark energy, two phenomena that are still as obscure as their names indicate. The main evidence for dark matter is that the gravitational force of galaxies would not overcome the centrifugal force caused by their rotation if it was not for additional unseen mass. Many dark matter particles have been postulated but remain unobserved.[27, 28] A recent publicated theory even proposed a description of gravity that removes this dark matter necessity.[29] Dark energy was proposed as a solution to the unexpected accelerating expansion of the universe. The most accepted dark energy explanation is the Einstein's cosmological constant, Λ, which is physically equivalent to the quantum vacuum energy. However, there are many other offered solutions.[30]

The incorporation of gravity, the origin of dark energy/matter and matter/anti-matter asymmetry are some of the issues of the Standard Model that demand extensions. One way of probing these new theories is by studying the properties of the Higgs boson. Several new theories predict extensions of the Higgs sector that can be characterized with certain Higgs properties. Measurements on these properties can therefore open the door to new physics.

To make such precision measurements particle physics research had to transform substantially in the past decades. One of the most characteristic developments is the indispensability of computers. Especially within the scientific community of CERN many computational resources are available for storage and analysis of data but more efficient usage is always needed. This thesis therefore presents a modelling technique in the context of Higgs properties measurement that reduces computational effort.

The thesis is structured as follows: Chapter 2 introduces the theoretical framework. Chapter 3 presents the structure and workings of the Large Hadron Collider and the ATLAS Experiment. Chapter 4 describes how observed and simulated data are reconstructed to physical objects such as particles or jets. Chapter 5 presents an overview of currently known Higgs properties and dominant Higgs production and decay modes at the LHC. Chapter 6 presents the measurement of the signal strength and chapter 7 of the effective Higgs coupling parameters. Chapter 8 summarizes the results and discusses future study prospects.

Chapter 2

Theoretical Framework

Over the years many theorists have shown great creativity and effort in the development of theories that describe the fundamental character of matter. The goal of these theories is to model nature in a mathematical framework with calculable observable quantities that can also be measured in experiment.

For a long time the Newtonian laws of motion and Maxwell's theory of electromagnetism dictated the dynamics of the world around us. However, in the early 20th century the theory of quantum mechanics was introduced and gave new revelations on the subatomic scale. The theory entails the quantization of physics in which system quantities such as energy are not continuous but may be restricted to a discrete set of values. Additional to that is the duality of particles which states that a particle can be described by a wave function containing the probabilities of different states the particle might be in. Measuring an observable quantity such as position or momentum will force the particle into one of these states corresponding to one of the possible discrete values for this quantity. Together with the Heisenberg's uncertainty principle, the principle that you can not know certain quantities to an arbitrary precision simultaneously, these concepts profoundly changed our deterministic view on nature but have shown great success in describing non-relativistic subatomic physics.

Parallel to the development of quantum mechanics the theory of special relativity emerged. The theory was postulated by Albert Einstein who described in his theory how time and distance are affected by movement and included his famous mass-to-energy relation $E = mc^2$. The first combination theories of relativistic quantum mechanics were created in the late 1920s and posed an improvement with respect to quantum mechanics on handling subjects such as anti-matter and spin. However, the theories remained an approximation as they did not describe how particles can be created or annihilated.

Quantum Field Theory (QFT) was born in the necessity to improve the concepts of relativistic quantum mechanics. In the 1920s Paul Dirac took the first steps by quantizing classical electromagnetic fields in an attempt to describe the creation and annihilation of particles. However, it was only in the 1950s that Richard Feynman reformulated Diracs theory of Quantum Electrodynamics (QED) into one with calculable quantities. This resulted in the first complete QFT and laid the foundation for the Standard Model of Particle Physics as we know it today.

This chapter will start with a brief superficial introduction on the Standard Model. The subsequent section will continue with basic concepts in QFT and how it is used to compute measurable quantities in particle physics. After that the different types of QFT's that make up the Standard Model are discussed with an extra focus on the Higgs boson and how it plays a role in this picture. Additionally some concepts of Effective Field Theory are introduced to facilitate a model for the effective coupling measurement and the Effective Lagrangian Morphing technique that is used for this measurement.

2.1 The Standard Model of Particle Physics

The Standard Model of Particle Physics is the model that describes the most fundamental building blocks of the universe and the interactions between them. This section will entail a simplified conceptual description to give a general but superficial idea of its constituents and workings. After that the view is expanded with concepts on quantum field theories and the mathematical machinery behind it all to give a more detailed and complete description of the Standard Model.

In figure 2.1 you can find an overview of all the currently known elementary particles along with their mass, color charge, electric charge and spin. The latter is a quality that divides the elementary particles into the first two groups, the fermions with half integer spin and bosons with integer spin. The fermions consist of the quarks and leptons which make up all matter around us whilst the gluons, photons, Z^0 and $W^{\pm}$ bosons mediate resp. the strong, electromagnetic and the weak force. The Higgs boson does mediate the interaction with the Higgs field but does not result in a new gauge symmetry like the before mentioned bosons. Instead the Higgs field ”gives” particles mass through the Higgs mechanism.

At the bottom right of figure 2.1 a space is left blank for the hypothesized graviton particle which should mediate the gravitational force. No particle with fitting characteristics has yet been found to support a theory of quantum gravity. However, in the upcoming sections the gravitational force can be neglected as its strength is negligible on sub-nuclear scales.

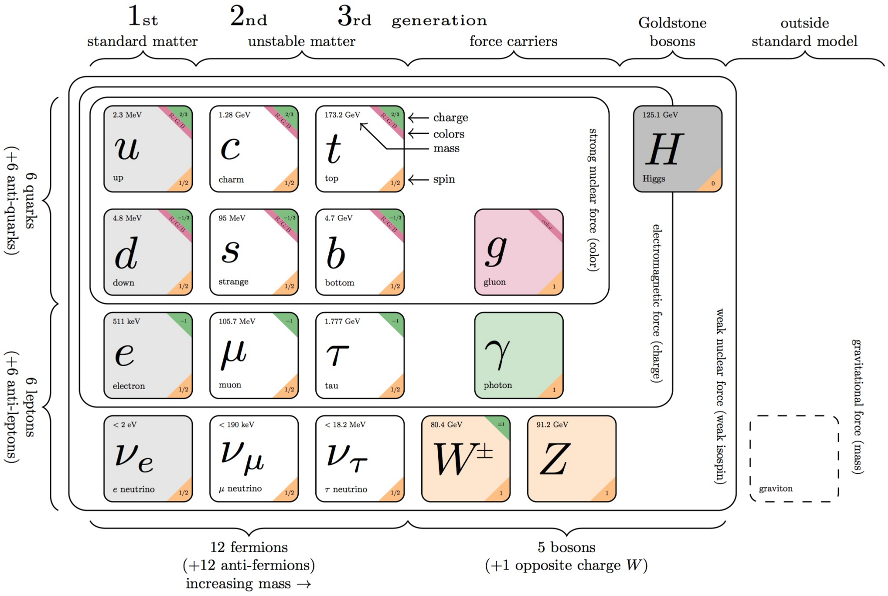

Figure 2.1: The Standard Model of Particle Physics[2]

The Standard Model is described by a renormalizable quantum field theory. This is a very effective mathematical framework in which particles are considered to be excitations of fields and their dynamics are described by the Lagrangian formalism and gauge symmetries.

2.2 Lagrangian formalism

The Lagrangian formalism initially was a reformulation of the Newtonian classical mechanics. However, in this section we will show how the concepts of this mathematical framework can be used to describe particles with fields in a quantum field theory. There are two different ways to generalize the classical Lagrangian formalism to a quantum field theory: the path integral description and canonical quantization.

The latter is similar to the *first quantization* of classical mechanics to non-relativistic quantum mechanics where coordinates are upgraded to operators, appropriate commutation rules are applied and quantum states are introduced that describe a system.

In the *second quantization* the classical fields are similarly upgraded to quantum operator valued fields and the single-particle quantum mechanical states are replaced with the Fock states that can describe a quantum mechanical many-body system. However, this framework requires a very detailed and extenive description of quantum field theory. The path integral description description might be a bit more obscure in its workings but in the end gives an elegant and convenient approach to quantum field theory. It couples easy to experimental observation and is therefore chosen over canonical quantization to fit the theoretical needs of this thesis. Additional information on the Lagrangian formalism can be found in the following references [31–34].

2.2.1 Principle of Least Action

The path integral description starts with the principle of least action. This is a variational principle that, when applied to the action, gives the equations of motion of a system. The action is defined as

$$\mathcal{S}[\mathbf{q}(t)] = \int_{t_1}^{t_2} L(\mathbf{q}(t), \dot{\mathbf{q}}(t)) dt. \tag{2.1}$$

The action is a time integral over the Lagrangian $L(q(t), \dot{q}(t))$ which is a function of a set of generalized coordinates $q(t)$ and their time derivates $\dot{q}(t)$. The evolution from one state at time t_1 to another at t_2 can go along different paths in configuration space. The *principle of least action* states that the path taken by the system is the one for which the action is stationary to the first order, i. e. $\delta\mathcal{S} = 0$, as depicted in figure 2.2. From this the Euler-Lagrange equation can be derived

$$\frac{d}{dt}\Big(\frac{\partial L}{\partial \dot{q}}\Big) - \frac{\partial L}{\partial q} = 0. \tag{2.2}$$

The equations of motion of a system can be derived from the Euler-Lagrange equation by defining an appropriate Lagrangian.

2.2.2 Path Integrals in Quantum Mechanics

The previous subsection shows that if the Lagrangian is known the system will choose a definite path through configuration space and thus define the time evolution of the system. The world of subatomic physics is however not deterministic but probabilistic in nature. Each path that is possible between an initial to a final quantum state comes with a probabilistic amplitude $e^{i\mathcal{S}}$, where $\mathcal{S}$ is the previously introduced action. The

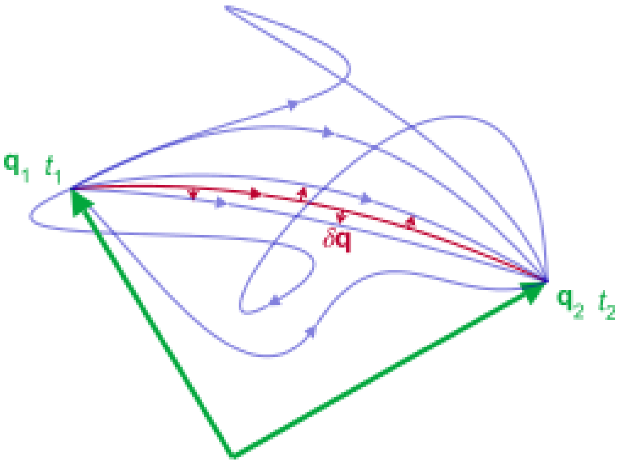

FIGURE 2.2: Different paths through configuration space. The red line indicates the path for which $\delta S = 0$[3]

sum of these amplitudes results in the probability that this transition will occur. For an initial $|q_i, t_i\rangle$ to a final quantum state $|q_f, t_f\rangle$ this probability is defined as

$$P(q_f, t_f; q_i, t_i) = |\langle q_f, t_f | q_i, t_i \rangle|^2 \tag{2.3}$$

with the probability amplitude

$$\langle q_f, t_f | q_i, t_i \rangle = \int \mathcal{D}q(t) e^{i/\hbar \int_{t_i}^{t_f} dt L(q, \dot{q})} \tag{2.4}$$

where $\mathcal{D}q(t)$ denotes an integral taken over all possible paths between q_f and q_i. The goal in the upcoming sections is to give a mathematical description of these probability amplitudes as they can be used to relate the probability of these transitions to a measurable quantity known as the cross section. (See section 2.5).

When studying a quantum mechanical system it is preferable to influence the system with an external source and observe the impact. To this experimental end the Lagrangian is adjusted accordingly with an additional term.

$$L(q, \dot{q}) \rightarrow L(q, \dot{q}) + J(t)q(t) \tag{2.5}$$

Here the time-dependent and coordinate independent source J(t) is introduced. The result is a new functional also known as the *generating functional* that will show to be a practical mathematical tool for computing probability amplitudes in QFT.

$$Z[J] = \int \mathcal{D}q(t)e^{i/\hbar \int_{t_i}^{t_f} dt(L(q,\dot{q})+J(t)q(t))} \tag{2.6}$$

2.2.3 Free Scalar Field Theory

The idea of particles as point-like objects is perhaps easy to imagine and a good approximation for certain scenarios. However, this classical description is not the most profound one and eventually breaks down on increasing smaller scales. The fundamental fabric of nature are fields that permeate all space and excited states or quanta of these fields are the particles that we observe. To generalize the Lagrangian formalism to field theory the generalized coordinate q is replaced with a field at a certain point in space-time $\phi(x, y, z, t)$ and the Lagrangian L with the *Lagrangian density* $\mathcal{L}$. The principle of least action, the action and Euler-Lagrange equations are resp. redefined as

$$\frac{\delta \mathcal{S}}{\delta \phi} = 0 \tag{2.7}$$

$$\mathcal{S}[\phi(x, y, z, t)] = \int \mathcal{L}(\phi, \partial_\mu \phi) d^4x \tag{2.8}$$

$$\partial_\mu \Big(\frac{\delta \mathcal{L}}{\delta(\partial_\mu \phi)} \Big) - \frac{\delta \mathcal{L}}{\delta \phi} = 0 \tag{2.9}$$

which introduces the four-gradient $\partial_\mu = (\frac{1}{c}\frac{\partial}{\partial t}, \vec{\nabla})$ and the scalar field ϕ. The simple free scalar field is chosen for didactic purposes but particles can also be represented by other fields such as vector or tensor fields and can added to the framework accordingly. Recall, the functional of equation 2.6 which can be adjusted with the concepts of fields to

$$Z[J] = \frac{1}{Z_0} \int \mathcal{D}\phi e^{i/\hbar \int d^4x(\mathcal{L}(\phi)+J(x)\phi)} \tag{2.10}$$

where the source is dependent on space-time coordinate x but not on the field ϕ.

The term Z_0 is a normalization term and is defined as

$$Z_0 = \int \mathcal{D}\phi e^{i/\hbar \int d^4x \mathcal{L}(\phi)}. \tag{2.11}$$

Note that just like in classical mechanics all the physics is still encoded in the Lagrangian. Thus, the first step in the construction of a quantum field theory is defining the appropriate Lagrangian of which is expected to describe the physical system and result in finite probability amplitudes. The Lagrangian of the Standard Model will be handled in the upcoming sections. For now the *free scalar field Lagrangian* representing a free, i. e. excluding any interactions, spin-0 particle is chosen for didactic purposes.

$$\mathcal{L} = \frac{1}{2}\partial_\mu \phi \partial^\mu \phi - \frac{1}{2} m^2 \phi^2 \tag{2.12}$$

The Euler-Lagrange equations result in the *homogeneous Klein-Gordon equation* that is defined as

$$(\Box + m^2)\phi = 0 \tag{2.13}$$

where $\Box = \partial^\mu \partial_\mu$ is the d'Alembert operator. However, because the source term was introduced the Euler-Lagrange equations result in the *heterogeneous Klein-Gordon equation.*

$$(\Box + m^2)\phi = J(x) \tag{2.14}$$

This equation can be solved by introducing the Feynman propagator $G(x, y)$ that satisfies,

$$(\Box + m^2)G(x, y) = \delta^4(x - y). \tag{2.15}$$

The Feynman propagator is a type of Green's function and can be obtained by solving equation 2.15 in Fourier space.

$$G(x, y) = \int \frac{d^4k}{(2\pi)^4} \frac{e^{ik\cdot(x-y)}}{k^2 - m^2} \tag{2.16}$$

By using equations 2.11, 2.12, 2.13, 2.14, 2.15 and 2.16 in a formal derivation, which can be found in appendix A.1, a final expression of the functional $Z[J]$ is obtained.

$$Z[J] = \exp\left[-\frac{i}{2}\int J(x)G(x,y)J(y)d^4xd^4y\right] \tag{2.17}$$

This expression is very useful for the calculation of *time ordered products* i. e. probability amplitudes. Time ordered products, also known as *n-point correlation functions*, are defined as,

$$\langle 0|T[\phi(x_1)...\phi(x_n)]|0\rangle = \frac{1}{i^n}\frac{\delta^n Z[J]}{\delta J(x_1)...J(x_n)}\bigg|_{J=0}. \tag{2.18}$$

By taking the second order functional derivative of $Z[J]$ evaluated at $J = 0$ the *2-point correlation function* can be calculated in terms of Feynman propagators.

$$\langle 0|T[\phi(x_1)\phi(x_2)]|0\rangle = \frac{1}{i^2}\frac{\delta^2 Z[J]}{\delta J(x_1)\delta J(x_2)}\bigg|_{J=0} = iG(x_1,x_2) \tag{2.19}$$

The Feynman propagator can be depicted graphically through what is also known as a Feynman diagram as shown in figure 2.3.

FIGURE 2.3: Feynman diagram of a Feynman propagator representing a particle creation and destruction

The Feynman diagrams give a simple visualization that prove to be helpful in the calculation of the probability amplitudes. The probability amplitude that it represents here is of the creation of a particle at x_1 and later destruction at x_2. This can be extended to a *4-point correlation function*.

$$\begin{aligned}\langle 0|T[\phi(x_1)\phi(x_2)\phi(x_3)\phi(x_4)]|0\rangle = \frac{1}{i^4}\frac{\delta^4 Z[J]}{\delta J(x_1)\delta J(x_2)\delta J(x_3)\delta J(x_4)}\bigg|_{J=0} &= iG(x_1,x_2)iG(x_3,x_4)\\ &+iG(x_1,x_3)iG(x_2,x_4)\\ &+iG(x_2,x_3)iG(x_1,x_4)\end{aligned} \tag{2.20}$$

Again these Feynman propagators can be depicted with Feynman diagrams as shown in figure 2.4.

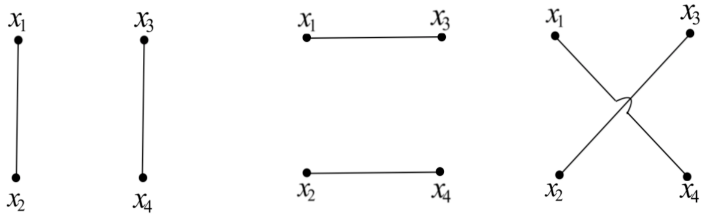

Figure 2.4: Feynman diagrams of a 4-point correlation function representing all possible particle creations and destructions

As expected is the probability amplitude the sum of all the permutations of particle creation and destruction with respect to space-time points x_1, x_2, x_3 and x_4. Correlation functions give non-trivial results if n is even which means that each line in a Feynman diagram is connected to a source(creation) and a sink(destruction). The previous correlation functions show a pattern for an expression of which the derivation can be found in Appendix A.2.

$$\langle 0|T[\phi(x_1)...\phi(x_{2n})]|0\rangle = \sum_{\sigma} iG(x_{\sigma_1}, x_{\sigma_2})...G(x_{\sigma_{2n-1}}, x_{\sigma_{2n}}) \tag{2.21}$$

Here the sum runs over all possible pairings of $1, 2, ..., 2n$. This formula is also known as *Wick's theorem* [33].

2.2.4 Perturbation Theory

In the previous section it is shown how the generating functional $Z[J]$ is an elegant tool to calculate probability amplitudes in terms of Feynman propagators. To introduce interactions the appropriate terms need to be added to the Lagrangian. The perturbation theory adds a ϕ^4-term that represents the self-interaction between scalar fields in one point and is defined as

$$\mathcal{L}_{\text{int}}(\phi) = -\frac{\lambda}{4!}\phi^4. \tag{2.22}$$

The additional interaction term makes the previous procedure in calculating n-point correlation functions troublesome. The extra quartic interaction term makes the reformulation of $Z[J]$ to equation 2.17 not possible. However, by assuming that the factor λ remains small it is possible to construct a *weak coupling perturbation theory.* The generating functional is redefined as

$$Z[J] = \frac{1}{Z_0} \int \mathcal{D}\phi e^{i/\hbar \int d^4x (\mathcal{L}_0(\phi) + \mathcal{L}_{int}(\phi) + J(x)\phi)} \tag{2.23}$$

where $\mathcal{L}_0$ is the previously introduced free scalar Lagrangian. It is possible to expand the exponent in the interaction term $\mathcal{L}_{int}$ if λ is small enough.

$$Z[J] = \frac{\int \mathcal{D}\phi e^{i/\hbar \int d^4x (\mathcal{L}_0(\phi) + J(x)\phi)} \Big[1 + \frac{i}{\hbar}\Big(-\frac{\lambda}{4!}\Big) \int d^4y \phi(y)^4 + \mathcal{O}(\lambda^2)\Big]}{\int \mathcal{D}\phi e^{i/\hbar \int d^4x \mathcal{L}_0(\phi)} \Big[1 + \frac{i}{\hbar}\Big(-\frac{\lambda}{4!}\Big) \int d^4y \phi^4(y) + \mathcal{O}(\lambda^2)\Big]} \tag{2.24}$$

Again the n-point correlation function can be acquired by taking the functional derivative of $Z[J]$ with respect to J and evaluating it at $J = 0$.

$$\langle 0|T[\phi(x_1)...\phi(x_n)]|0\rangle = \frac{\int \mathcal{D}\phi e^{i/\hbar \int d^4x \mathcal{L}_0(\phi)} \phi(x_1)...\phi(x_n) \Big[1 + \frac{i}{\hbar}\Big(-\frac{\lambda}{4!}\Big) \int d^4y \phi^4(y) + \mathcal{O}(\lambda^2)\Big]}{\int \mathcal{D}\phi e^{i/\hbar \int d^4x \mathcal{L}_0(\phi)} \Big[1 + \frac{i}{\hbar}\Big(-\frac{\lambda}{4!}\Big) \int d^4y \phi^4(y) + \mathcal{O}(\lambda^2)\Big]} \tag{2.25}$$

Recall that the free scalar n-point correlation function is defined as

$$\langle 0|T[\phi(x_1)...\phi(x_n)]|0\rangle = \frac{1}{i^n} \frac{\delta^n Z[J]}{\delta J(x_1)...J(x_n)}\bigg|_{J=0}. \tag{2.26}$$

This results in the n-point correlation function

$$\begin{aligned} \langle 0|T[\phi(x_1)...\phi(x_n)]|0\rangle = \langle 0|T[\phi(x_1)...\phi(x_n)]|0\rangle_0 + \frac{i}{\hbar}\Big(-\frac{\lambda}{4!}\Big) \int d^4y \langle 0|T[\phi(x_1)...\phi(x_n)\phi^4(y)]|0\rangle_0 \\ -\langle 0|T[\phi(x_1)...\phi(x_n)]|0\rangle_0 \frac{i}{\hbar}\Big(-\frac{\lambda}{4!}\Big) \int d^4y \langle 0|T[\phi^4(y)]|0\rangle_0 + \mathcal{O}(\lambda^2). \end{aligned} \tag{2.27}$$

The n-point correlation function is constructed from n-point correlation functions of the free scalar theory which are denoted with a subscript zero. For illustration lets evaluate the 4-point correlation function.

$$
\begin{aligned}
\langle 0|T[\phi(x_1)\phi(x_2)\phi(x_3)\phi(x_4)]|0\rangle &= \langle 0|T[\phi(x_1)\phi(x_2)\phi(x_3)\phi(x_4)]|0\rangle_0 \\
&+\frac{i}{\hbar}\Big(-\frac{\lambda}{4!}\Big)\int d^4y \langle 0|T[\phi(x_1)\phi(x_2)\phi(x_3)\phi(x_4)]|0\rangle_0 \\
-\langle 0|T[\phi(x_1)\phi(x_2)\phi(x_3)\phi(x_4)\phi^4(y)]|0\rangle_0 &\frac{i}{\hbar}\Big(-\frac{\lambda}{4!}\Big)\int d^4y \langle 0|T[\phi^4(y)]|0\rangle_0 + \mathcal{O}(\lambda^2)
\end{aligned}
\tag{2.28}
$$

With the use of Wick's theorem the free correlation functions can easily be evaluated. Again for each term of the sum an associated Feynman diagram can be drawn as shown in figure 2.5.

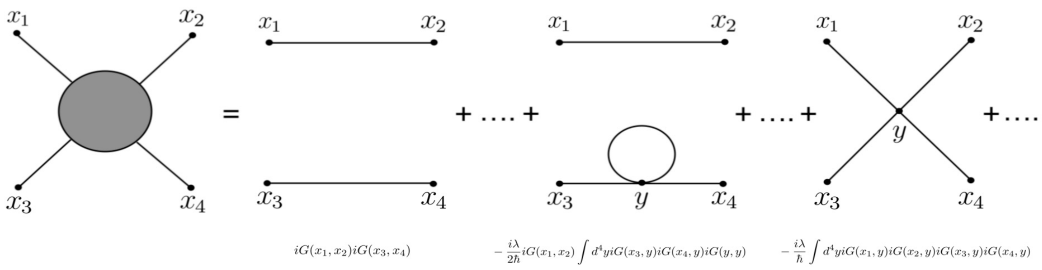

FIGURE 2.5: Feynman diagrams of a 4-point correlation function representing all possible particle creations and destructions including self-interactions. The first entails one of the free scalar correlation functions, the second introduces a loop interaction and the third a 4-point interaction

Even though the many permutations sum up to a lot of terms it is possible to use equation 2.16 and compute the 4-point correlation function. Lets consider the amplitude for a 4-point interaction i. e. the amplitude of the last diagram given in figure 2.5.

$$
\begin{aligned}
&\frac{i\lambda}{\hbar}\int d^4y iG(x_1,y)iG(x_2,y)iG(x_3,y)iG(x_4,y) \\
&= \frac{i\lambda}{\hbar}\int d^4y \int \frac{d^4k_1}{(2\pi)^4}\frac{e^{ik_1\cdot(x_1-y)}}{k_1^2-m^2}\cdots\int\frac{d^4k_4}{(2\pi)^4}\frac{e^{ik_4\cdot(x_4-y)}}{k_4^2-m^2} \\
&= \frac{i\lambda}{\hbar}\int\frac{d^4k_1}{(2\pi)^4}\cdots\int\frac{d^4k_4}{(2\pi)^4}(2\pi)^4\delta^4(k_1+k_2+k_3+k_4) \\
&\quad\times\frac{1}{k_1^2-m^2}\cdots\frac{1}{k_4^2-m^2}e^{ik_1\cdot x_1}\dots e^{ik_4\cdot x_4}
\end{aligned}
\tag{2.29}
$$

Here are $k_1, ..., k_4$ the momenta of the respective particles that interact. In a similar way the contributions of the other diagrams can be calculated for an expansion up to an arbitrary order of λ. In Monte Carlo simulations accuracy in cross section calculation is therefore denoted as *Leading Order (LO)* for expansions up to the first order of λ or *Next-to-Leading Order (NLO)* for up to λ^2-terms.

The above framework shows how from first principles an expression for the amplitude can be derived for simplistic scenarios, the free scalar and ϕ^4-theory. Amplitude computation can be expanded to other fields and types of interactions but is almost never as straightforward as these examples. However, it is shown that the Lagrangian dictates the physical theory you want to describe and results in a cross section that can be measured. The upcoming sections are therefore used for the structure and motivation of the Lagrangian that makes up our Standard Model of Particle Physics.

2.3 Gauge Symmetries

Symmetries play a vital role in physics and are found whenever a system remains unchanged under an applied transformation. In the classical sense this means a transformation in the general coordinates q that leaves the value of the Lagrangian unaffected. Noether's theorem states that if this is the case then such a symmetry corresponds to a conservation law. In this section it is shown how the invariance of a Lagrangian under certain groups of transformations results in the introduction of the fundamental interactions between various fields that represent the particles in the Standard Model. Additional information on gauge symmetries can be found in the following textbooks [4, 35–38].

Quantum Electrodynamics

Quantum Electrodynamics was the first gauge theory constructed for the description of particle physics. In this section it is used to show how a gauge symmetry results in a gauge field that mediates a fundamental interaction, the electromagnetic interaction. Quantum electrodynamics was a successful theory that described the interaction between electrons, positrons and photons. Since electrons and positrons are fermions the Lagrangian for a free spin-$\frac{1}{2}$ particle is introduced.

$$\mathcal{L} = i\bar{\psi}\gamma^\mu\partial_\mu\psi - m\bar{\psi}\psi \tag{2.30}$$

Here γ^μ are the gamma matrices and ψ a four-component spinor field. Now lets apply a $U(1)$ local gauge transformation of which the Lagrangian is required to be invariant under,

$$\psi \rightarrow \psi' = e^{iq\xi(x)}\psi. \tag{2.31}$$

Note that the dependence of the phase $\xi(x)$ on arbitrary space-time coordinates makes the gauge transformation local. This results in the following transformed Lagrangian

$$\mathcal{L} \rightarrow \mathcal{L}' = ie^{iq\xi(x)}\bar{\psi}\gamma^\mu[e^{iq\xi(x)}\partial_\mu\psi + iq(\partial_\mu\xi(x))e^{-iq\xi(x)}\psi] - me^{-iq\xi(x)}\bar{\psi}e^{iq\xi(x)}\psi \tag{2.32}$$

or in terms of the original Lagrangian

$$= \mathcal{L} - q\bar{\psi}\gamma^\mu(\partial_\mu)\psi. \tag{2.33}$$

The Lagrangian is not invariant under this local gauge transformation. To restore the local gauge invariance the derivative needs to be replaced with the *covariant derivative*,

$$\partial_\mu \rightarrow D_\mu = \partial_\mu + iqA_\mu \tag{2.34}$$

where a new four-component gauge field A_μ is introduced. The last addition to complete the gauge invariance is by imposing that the new gauge field transforms in the following way.

$$A_\mu \rightarrow A'_\mu = A_\mu - \partial_\mu\xi(x) \tag{2.35}$$

Only by introducing a new gauge field with very specific transformation properties can the Lagrangian stay invariant under a local gauge transformation. The $U(1)$ local gauge invariant Lagrangian for a spin-$\frac{1}{2}$ fermion therefore reads,

$$\mathcal{L} = \bar{\psi}(i\gamma^\mu\partial_\mu - m)\psi - q\bar{\psi}\gamma^\mu A_\mu\psi \tag{2.36}$$

which shows that the result of imposing a local gauge invariance is an additional interaction term between the fermionic field ψ and gauge field A_μ that can be interpreted as a photon. To make this photon field physical the field strength tensor is defined as

$$F_{\mu\nu} = \partial_\mu A_\nu - \partial_\nu A_\mu \tag{2.37}$$

The term $F_{\mu\nu}F^{\mu\nu}$ is already invariant under the $U(1)$ local gauge transformation. By adding this last kinematic term for a massless spin-1 field we get the final QED Lagrangian.

$$\mathcal{L} = \bar{\psi}(i\gamma^\mu \partial_\mu - m)\psi - q\bar{\psi}\gamma^\mu A_\mu \psi - \frac{1}{4}F_{\mu\nu}F^{\mu\nu} \tag{2.38}$$

The Standard Model Gauge Theory

Now that we saw how a gauge theory is constructed it is possible to extend it to the complete gauge theory of the Standard Model. The Standard Model can be described by the combination of three different gauge groups

$$SU(3)_C \otimes SU(2)_L \otimes U(1)_Y \tag{2.39}$$

where we make the distinction between the $SU(3)_C$ group representing the strong interactions and $SU(2)_L \otimes U(1)_Y$ group for the electroweak interactions, the unified theory of electromagnetic and weak interactions. The subscripts refer to the color charge (C), hyper charge (Y) and left-handed fermions (L). The reason for these subscripts will be addressed in the following sections.

Electroweak interaction

The gauge group $SU(2)_L \otimes U(1)_Y$ is also known as the Glashow-Salam-Weinberg model of electroweak interactions. Again a local gauge transformation is applied, the appropriate gauge fields are added by introducing a covariant derivative and specific transformations are imposed for the corresponding gauge fields to acquire new interactions. A more general form for a local gauge transformation can be defined as

$$U(x) = e^{iA_j(x)B_j} \tag{2.40}$$

where $A_j(x)$ is the space-time coordinate dependent phase parameter and B_j the generator of the gauge group. The number of generators per group equals to the number of phase parameter and is also the same as the dimension of the gauge group. $U(N)$ is the group of unitary $N \times N$ matrices and has dimension N^2.

The $SU(N)$ is the group of special unitary traceless, i. e. with determinant $D = 1$, $N \times N$ matrices and has the dimension of $N^2 - 1$. A group is called *abelian* if the corresponding generators commute and *non-abelian* if otherwise. $SU(2)_L$ is a non-abelian group associated to the weak isospin (I_3) with the Pauli matrices $\vec{\tau} = (\tau_1, \tau_2, \tau_3)$ as generators. Fermions with left-handed chirality have weak isospin $I_3 = \pm\frac{1}{2}$ and are $SU(2)_L$ doublets while fermions with right-handed chirality have $I_3 = 0$ and are $SU(2)_L$ singlets. This means that the associated gauge fields $\vec{W}^i_\mu = (W^1_\mu, W^2_\mu, W^3_\mu)$ only interact with left-handed fermions. Hence the subscript L in the group notation.

The $U(1)_Y$ is an abelian group associated to the weak hypercharge Y_W with generator $B = 1$. It acts on fermions with all chiralities and generates a gauge field B_μ. The weak hypercharge is linked to the electric charge Q and weak isospin I_3 by the relation $Q = I_3 + \frac{Y_W}{2}$. In table 2.1 you can find the $SU(2)_L$ representation of all the fermions in the Standard Model.

Because the $SU(2)_L$ makes a distinction between right-handed ψ_R and left-handed ψ_L fermion fields, two different gauge transformations need to be introduced.

$$\psi_R \to e^{-i\beta(x)\frac{Y_W}{2}}\psi_R \tag{2.41}$$

$$\psi_L \to e^{-i\alpha_i(x)\frac{\tau_i}{2} - i\beta(x)\frac{Y_W}{2}}\psi_L \tag{2.42}$$

	1^{st} gen.	2^{nd} gen.	3^{rd} gen.	I_3	Y_W	Q
Quarks	$\begin{pmatrix} u_L \\ d_L \end{pmatrix}$	$\begin{pmatrix} c_L \\ s_L \end{pmatrix}$	$\begin{pmatrix} t_L \\ b_L \end{pmatrix}$	$\begin{pmatrix} \frac{1}{2} \\ -\frac{1}{2} \end{pmatrix}$	$\begin{pmatrix} \frac{1}{3} \\ \frac{1}{3} \end{pmatrix}$	$\begin{pmatrix} \frac{2}{3} \\ -\frac{1}{3} \end{pmatrix}$
	u_R	c_R	t_R	0	$\frac{4}{3}$	$\frac{2}{3}$
	d_R	s_R	b_R	0	$-\frac{2}{3}$	$-\frac{1}{3}$
Leptons	$\begin{pmatrix} \nu_{e,L} \\ e_L \end{pmatrix}$	$\begin{pmatrix} \nu_{\mu,L} \\ \mu_L \end{pmatrix}$	$\begin{pmatrix} \nu_{\tau,L} \\ \tau_L \end{pmatrix}$	$\begin{pmatrix} \frac{1}{2} \\ -\frac{1}{2} \end{pmatrix}$	$\begin{pmatrix} -1 \\ -1 \end{pmatrix}$	$\begin{pmatrix} 0 \\ -1 \end{pmatrix}$
	e_R	μ_R	τ_R	0	-2	1

TABLE 2.1: Classification and properties of the Standard Model fermions in the $SU(2)_L$-representation

These transformation give rise to two different covariant derivatives resp. defined as

$$D_\mu = \partial_\mu + ig_1\frac{Y_W}{2}B_\mu \tag{2.43}$$

$$D_\mu = \vec{I}(\partial_\mu + g_1\frac{Y_W}{2}B_\mu) + ig_2\frac{\vec{\tau}}{2}\vec{W}_\mu. \tag{2.44}$$

The gauge constants g_1 and g_2 define the coupling strength of the introduced interactions. We now impose the following transformation on the new gauge fields

$$W^i_\mu \rightarrow W^i_\mu + \alpha^j(x)\epsilon^{ijk}W^k_\mu + \frac{1}{g_2}\partial_\mu \alpha^i(x) \tag{2.45}$$

$$B_\mu \rightarrow B_\mu + \frac{1}{g_1}\partial_\mu \beta(x) \tag{2.46}$$

where ϵ^{ijk} is the Levi-civita function and originates from the generator commutation rules $[\sigma_i, \sigma_j] = 2i\epsilon^{ijk}\sigma_k$. Again field strength tensors for the new gauge fields are defined.

$$W^i_{\mu\nu} = \partial_\mu W^i_\nu - \partial_\nu W^i_\mu - g_2\epsilon^{ijk}W^j_\mu W^k_\nu \tag{2.47}$$

$$B_{\mu\nu} = \partial_\mu B_\nu - \partial_\nu B_\mu \tag{2.48}$$

These give the kinematic terms and the final electroweak Lagrangian for the $SU(2)_L \otimes U(1)_Y$ group.

$$\mathcal{L}_{EW} = \sum_{\psi_L} \bar{\psi_L} i\gamma^\mu D_\mu \psi_L + \sum_{\psi_R} \bar{\psi_R} i\gamma^\mu D_\mu \psi_R - \frac{1}{4}W^{\mu\nu}_i W^i_{\mu\nu} - \frac{1}{4}B_{\mu\nu}B^{\mu\nu} \tag{2.49}$$

Strong interaction

The $SU(3)_C$ group is the last part of the Standard Model gauge theory and describes the strong interaction. The gauge group is non-abelian and is associated with the color charge (C) which can take either the direction *green, blue* or *red.* The eight generators of this $SU(3)_C$ symmetry are called the Gell-Mann matrices λ_i.

$$\lambda_1 = \begin{pmatrix} 0 & 1 & 0 \\ 1 & 0 & 0 \\ 0 & 0 & 0 \end{pmatrix}, \lambda_2 = \begin{pmatrix} 0 & -i & 0 \\ i & 0 & 0 \\ 0 & 0 & 0 \end{pmatrix}, \lambda_3 = \begin{pmatrix} 1 & 0 & 0 \\ 0 & -1 & 0 \\ 0 & 0 & 0 \end{pmatrix}, \lambda_4 = \begin{pmatrix} 0 & 0 & 1 \\ 0 & 0 & 0 \\ 1 & 0 & 0 \end{pmatrix} \tag{2.50}$$

$$\lambda_5 = \begin{pmatrix} 0 & 0 & -i \\ 0 & 0 & 0 \\ 0 & 0 & i \end{pmatrix}, \lambda_6 = \begin{pmatrix} 0 & 0 & 0 \\ 0 & 0 & 1 \\ 0 & 1 & 0 \end{pmatrix}, \lambda_7 = \begin{pmatrix} 0 & 0 & 0 \\ 0 & 0 & -i \\ 0 & i & 0 \end{pmatrix}, \lambda_8 = \frac{1}{\sqrt{3}}\begin{pmatrix} 1 & 0 & 0 \\ 0 & 1 & 0 \\ 0 & 0 & -2 \end{pmatrix} \tag{2.51}$$

Quarks are the only fermions with color charge so the associated gauge fields G^i_μ do not interact with leptons.

The quarks are arranged in triplets in the $SU(3)_C$ representation and are transformed in the following way.

$$q^f \rightarrow q^f e^{-i\alpha_a(x)\frac{\lambda_a}{2}} \tag{2.52}$$

These transformations give rise to a new covariant derivative

$$D_\mu = \partial_\mu + ig_3 \frac{\lambda_a}{2} G^a_\mu \tag{2.53}$$

where g_3 is the strong coupling constant and the 8 gauge fields G^i_μ correspond to the gluon gauge bosons. To reinstate the symmetry again the following gauge field transformation is imposed.

$$G^a_\mu \rightarrow G^a_\mu + \alpha^b(x) f^{abc} G^c_\mu + \frac{1}{g_3}\partial_\mu \alpha^a(x) \tag{2.54}$$

Here f^{abc} are the structure constants of the $SU(3)_C$ group which originate from the generator commutation rules $[\lambda_a, \lambda_b] = 2if^{abc}\lambda_c$. We define the field strength tensors for the new gauge fields as

$$G^a_{\mu\nu} = \partial_\mu G^a_\nu - \partial^a_\nu - g_3 f^{abc} G^b_\mu G^c_\nu \tag{2.55}$$

which again results in the kinetic term and the final Quantum Chromodynamic (QCD) Lagrangian.

$$\mathcal{L}_{QCD} = \sum_i \bar{q}^f_i (i\gamma_\mu D^\mu - m_f) q^f_i - \frac{1}{4} G^a_{\mu\nu} G^{\mu\nu}_a \tag{2.56}$$

2.4 Brout-Englert-Higgs mechanism

The local gauge principle provides an elegant description of the interactions in the Standard Model and have many high-precision measurements that agree with it. But until recently this picture of the subatomic world was not yet complete and dealt with some serious problems.

Particle masses

The fundamental interactions require that the Standard Model is invariant under transformations of any of the before mentioned gauge groups. However, this symmetry is broken when any mass terms are added to the Standard Model Lagrangian. Let us consider a fermionic field mass term $-m_f\bar{\psi}\psi$ and decompose the expression in helicity states.

$$-m_f\bar{\psi}\psi = -m_f(\bar{\psi}_R\psi_L + \bar{\psi}_L\psi_R) \tag{2.57}$$

However, equation 2.41 and 2.42 state that the helicity states behave differently under a $SU(2)_L \otimes U(1)_Y$ transformation.

$$-m_f(\bar{\psi}_R\psi_L + \bar{\psi}_L\psi_R) \rightarrow -m_f(\bar{\psi}_R e^{i\alpha_i(x)\frac{\tau_i}{2}}\psi_L + \bar{\psi}_L e^{-i\alpha_i(x)\frac{\tau_i}{2}}\psi_R) \neq -m_f\bar{\psi}\psi \tag{2.58}$$

The mass terms show that an arbitrary fermionic field breaks the electroweak gauge invariance. This is a problem as it is experimentally proven that fermions such as electrons or quarks have mass. A similar argument is made for the bosons. Consider a boson field mass term $\frac{1}{2}m_\gamma^2 A_\mu A^\mu$ for the photon. The theory of Quantum Electrodynamics required a local gauge invariance that imposed a specific gauge field transformation.

$$\frac{1}{2}m_\gamma^2 A_\mu A^\mu \rightarrow \frac{1}{2}m_\gamma^2(A_\mu + \partial_\mu\xi(x))(A^\mu + \partial^\mu\xi(x)) \neq \frac{1}{2}m_\gamma^2 A_\mu A^\mu \tag{2.59}$$

Of course it is known that the photon and gluon are massless but the broken symmetry also holds for the massive Z^0- and $W^\pm-$bosons.

Violating unitarity

Violating unitarity refers to the divergence of a scattering amplitude with increasing energy. The probability associated with the process the scattering amplitude represents can become arbitrarily large. This is the case for longitudinal polarized weak bosons. When bosons are longitudinal polarized their spin z-component is perpendicular to their moving vector.

A polarization four vector for longitudinal polarization can be defined as

$$\epsilon_L = \frac{1}{m_V}\begin{pmatrix} p_z \\ 0 \\ 0 \\ E \end{pmatrix}. \tag{2.60}$$

This can be used to describe the scattering amplitude of a $W_L^+W_L^+ \to W_L^+W_L^+$ process. In lowest order, this process will depent on three processes, the four-point interaction and the t-channel γ/Z exchanges. The Feynman diagrams of the leading order contributions to the scattering amplitude are shown in figure 2.6.

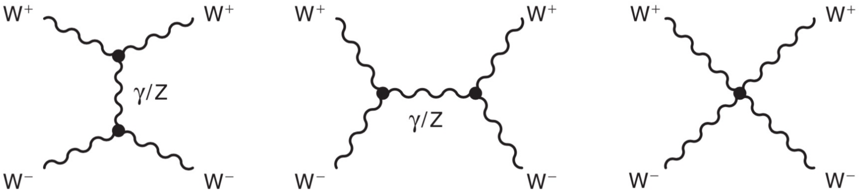

FIGURE 2.6: The leading order contributions to the amplitude of the $W^\pm W^\mp \to W^\pm W^\mp$[4]

The scattering amplitude of the four-point interaction is proportional to

$$\mathcal{M} \sim \epsilon_L\epsilon_L\epsilon_L\epsilon_L \sim E^4. \tag{2.61}$$

The scattering amplitude diverges and would violate unitarity for increasing energy. Additional information on unitarity violation for longitudinal polarized W-bosons can be found references [4, 39].

Spontaneous symmetry breaking

A solution for the above mentioned problems is to spontaneously break the electroweak symmetry through the Brout-Englert-Higgs mechanism. To describe this procedure the Higgs Lagrangian is introduced.

$$\mathcal{L}_{\text{Higgs}} = \mathcal{L}_{HG} + \mathcal{L}_{HF} \tag{2.62}$$

where $\mathcal{L}_{HG}$ and $\mathcal{L}_{HF}$ contain couplings of the Higgs boson to resp. the gauge bosons and fermions that will generate their masses and remove the violation of unitarity.

The derivation starts with an introduction of a complex scalar field in the $SU(2)_L$ representation

$$\Phi = \begin{pmatrix} \phi^+ \\ \phi^0 \end{pmatrix} = \frac{1}{\sqrt{2}} \begin{pmatrix} \phi_1 + i\phi_2 \\ \phi_3 + i\phi_3 \end{pmatrix}. \tag{2.63}$$

of which ϕ^0 represents a neutral scalar field and ϕ^+ a charged scalar field. The Lagrangian for this doublet of complex scalar fields can be written as,

$$\mathcal{L}_H = (\partial^\mu \Phi)^\dagger (\partial_\mu \Phi) - V(\Phi) \tag{2.64}$$

with the Higgs potential defined as

$$V(\Phi) = \mu^2 \Phi^\dagger \Phi + \lambda (\Phi^\dagger \Phi)^2. \tag{2.65}$$

The λ-term describes the quartic self-interaction of the scalar field and is required to be positive $\lambda > 0$ for vacuum stability. By minimising the potential the Higgs ground state i. e. the vacuum expectation value(VEV) can be found. For $\mu^2 > 0$ the trivial VEV of $\langle \Phi \rangle_0 = 0$ is obtained and the symmetry will remain unbroken. However, for $\mu^2 < 0$ a non-zero VEV is obtained.

$$\langle \Phi \rangle_0 = \sqrt{\frac{-\mu^2}{2\lambda}} = \frac{v}{\sqrt{2}}. \tag{2.66}$$

The minimum at the origin is no longer stable but is accompanied by an infinite set of degenerate vacuum states. These states all satisfy

$$\Phi^\dagger \Phi = \frac{1}{2}(\phi_1^2 + \phi_2^2 + \phi_3^2 + \phi_4^2) = \frac{v^2}{2}. \tag{2.67}$$

By choosing an arbitrary minimum, eg. $\phi_1 = \phi_2 = \phi_4 = 0$ and $\phi_3 = v$, it is possible to expand the field Φ around this minimum for small deviations $h(x)$.

$$\Phi(x) = \frac{1}{\sqrt{2}} \begin{pmatrix} \chi_1(x) + i\chi_2(x) \\ v + h(x) + i\chi_3(x) \end{pmatrix}. \tag{2.68}$$

The spontaneously symmetry breaking introduced three massless Goldstone bosons χ_i and one massive scalar boson $h(x)$. By taking the scalar field $\Phi(x)$ in the appropriate basis the Goldstone boson components χ_i can be set to zero. This is also known as the unitary gauge and results in the scalar field

$$\Phi(x) = \frac{1}{\sqrt{2}} \begin{pmatrix} 0 \\ v + h(x) \end{pmatrix}. \tag{2.69}$$

As a result the Higgs to gauge couplings become,

$$\begin{aligned} \mathcal{L}_{HG} = \frac{1}{2}(\partial_\mu h)(\partial^\mu h) + \frac{g^2}{4}(v+h)^2 W_\mu^+ W^{-\mu} + \frac{1}{8}\frac{g^2}{cos^2(\theta_W)}(v+h)^2 Z_\mu Z^\mu \\ + \frac{\mu^2}{2}(v+h)^2 - \frac{\lambda}{4}(v+h)^4. \end{aligned} \tag{2.70}$$

The full procedure of "gauging-away" the Goldstone bosons and constructing the above terms for the gauge bosons can be found in Appendix A.3. The new terms introduce the $W^\pm$- and Z^0-bosons as superpositions of the W_μ^i- and B_μ-fields. The Higgs-Gauge Lagrangian generates the mass terms of the $W^\pm$- and Z^0-bosons with the v^2-factors but leaves the photon field (A_μ) massless. The new masses are defined as

$$m_W = \frac{vg}{2}, m_Z = \frac{m_W}{cos(\theta_W)}, m_h = \sqrt{-\mu^2}. \tag{2.71}$$

Similar to the Higgs to gauge couplings one can use the concepts of spontaneous symmetry breaking to generate mass terms for the fermions. The Higgs to fermion couplings can be written as

$$\mathcal{L}_{HF} = -\sum_{u-\text{type}} g_u \bar{Q}_L \tilde{\Phi} u_R - \sum_{d-\text{type}} g_d \bar{Q}_L \Phi d_R - \sum_{l-\text{type}} (g_\nu \bar{L}_L \tilde{\Phi} \nu_{l,R} + g_l \bar{L}_L \Phi l_R) \tag{2.72}$$

with

$$\tilde{\Phi} = i\tau_2 \Phi^* = \frac{1}{\sqrt{2}}(v + h(x), 0). \tag{2.73}$$

This gives the following fermion mass contributions

$$\mathcal{L}_{HF} = -\frac{v + h(x)}{\sqrt{2}} \Big(\sum_{u-type} g_u \bar{u} u + \sum_{d-type} g_d \bar{d} d + \sum_{l-type} g_l \bar{l} l \Big). \tag{2.74}$$

The introduction of the Higgs boson also solves the unitarity violation. Recall that the scattering amplitude of longitudinally polarized $W^{\pm}$-bosons is dependent on the contribution of the 4-point interaction diagram. However, the Higgs boson introduces a new scattering process with the Higgs as mediator which adds new terms to the scattering amplitude. At large energies beyond the Higgs boson mass the result is,

$$\mathcal{M}_W + \mathcal{M}_H = g^2 \frac{m_H^2}{4m_W^2}. \tag{2.75}$$

The $\mathcal{M}_W$ is the amplitude contribution of the 4-point interaction and $\mathcal{M}_H$ of the Higgs mediated interaction. The energy dependence has been canceled out by the Higgs contribution and the unitarity requirement has been restored.[4, 39]

2.5 Cross section and Luminosity

The concepts of Lagrangian formalism and gauge theories give a detailed description on modelling amplitudes. However, the quantum mechanical processes are not measured in amplitudes but cross sections. Quantum mechanical processes at the LHC are transitions of an initial to a final state that has a specific probability of occurring. As a proxy for the probability, particle physicists measure transition rates for interesting processes in controlled environments, for example using particle colliders. The number of transitions N in a definite time interval T can be defined as,

$$N = \sigma \int_0^T L(t)dt \tag{2.76}$$

with the cross section σ and the instantaneous luminosity $L(t)$ i. e. the instantaneous rate of collisions. The amount of accumulated observed data that is used in an analysis is expressed in integrated luminosity, the integral of the instantaneous luminosity over time. The cross section gives a experiment agnostic measurement of probability and is defined as,

$$\sigma_{i\to j} = \int P_{i\to f} d\Omega \propto \int d\Omega |\mathcal{M}|^2 \tag{2.77}$$

where $\mathcal{M}$ denotes the previously introduced scattering amplitude of the process and $P_{i\to f}$ its probability. One of the most important dependencies of the cross section is the *centre-of-mass energy (CoM)* denoted by $\sqrt{s}$. The CoM energy is the total available energy in the Centre-of-Mass frame and is stated at the beginning of any collider experiment analysis.

2.6 Effective Field Theory

The goal of the modern physicist is to expand the current theories that are known and combine them to one universal theory of everything that works on every scale. Particle physicists try to go higher in energy and therefore smaller in scale to find new physics beyond the status quo that is the Standard Model. However, it is not always necessary or even feasible to take all the regimes into account. For example, in chemistry the laws are governed by the electromagnetic interaction that makes chemical bonds and reaction between atoms possible. The fundamental theory that lies at the basis of these processes is the previously introduced Quantum Electrodynamics. However, an attempt to describe the chemistry processes with QFT would be unnecessarily complex. A more simple and non-relativistic description of a classical atom with a Coulomb potential and electrons orbiting it would fit this regime better and give a more effective analysis. This example illustrates how neglecting effects outside the regime of analysis as an approximation can be a powerful tool. An effective field theory is exactly this. Any additional information on effective field theories can be found in the following references [40–42].

Effective field theories (EFT) give descriptions of physics in an energy regime defined by a cutoff scale Λ. Particles that can not be produced at these low energies, i. e. states with $m \gg \Lambda$, will not result in additional fields in the Lagrangian but will modify the couplings between lighter fields through higher-order loop effects involving the new particles. This process of removing the heavier fields from the Lagrangian is called *integrating out the fields*. There are two approaches to utilize an EFT:

- **Top-down** - The QFT beyond Λ is known. By integrating out the heavy fields theoretical calculations are simplified and the EFT can be used as an educational tool for the low energy regime.
- **Bottom-up** - The QFT beyond Λ is *not* known. We assume that the current accepted theory is the EFT and try to explore beyond this model by looking for deviations in the low energy regime that might infer new physics.

In this thesis the *bottom-up* approach is used to search for new physics beyond the energies of our current experiment. Signs for BSM physics can be found by studying deviations in Higgs couplings with other SM particles that can be produced in the energy regime of the LHC. However, it serves educational ends well to give a well-known example that visualizes the concepts of an effective field theory well.

2.6.1 Fermi theory

The textbook example of an EFT is Fermi theory. This theory illustrates how an effective field theory can be used to simplify the full underlying theory if we look at its respective low-energy regime. Fermi theory describes the charged current weak interactions between fermions and was first formulated by Enrico Fermi in 1934. In the Standard Model this type of interaction is mediated by the exchange of a W-boson and is described by the electroweak theory.

The process under study was the β-decay $n \rightarrow p^+e^-\bar{\nu}_e$ which is an interaction of a down to an up quark, an electron and an anti-electron neutrino. The Feynman diagram of this process is depicted in figure 2.7. The amplitude of this process has the following dependency.

$$\mathcal{M}_{\text{full}} \sim \frac{g_2^2}{q^2 - m_W^2} \tag{2.78}$$

Here m_W is the mass of the W-boson, g_2 is the previously introduced coupling constant of the $SU(2)_L \times U(1)_Y$ gauge symmetry and q^2 is the transferred momentum.

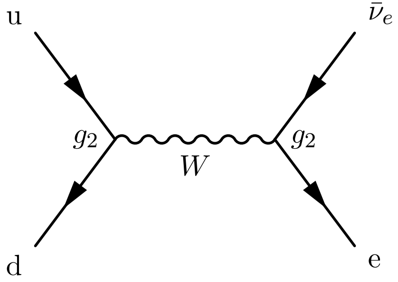

Figure 2.7: β-decay mediated by a W-boson as described by electroweak theory

Even though the W and Z bosons were not discovered until the 1980s Fermi was still able to give a good theoretical prediction by, unknowingly, constructing an EFT. In Fermi theory the energy cut-off scale is defined by the mass of the W-boson $\Lambda = m_W = 80.385\,\text{GeV}$ which is well above the characteristic β-decay energies of a few hundred keV.

This means that the W-boson is deeply virtual, i. e. $m_W^2 \gg q^2$, and the matrix element reduces to

$$\mathcal{M}_{EFT} \sim G_F \propto -\frac{g^2}{m_W^2} \tag{2.79}$$

where $G_F = 1.6637 \cdot 10^{-5}$ GeV^{-2} is the Fermi constant. The W-boson propagator has been contracted to a four-point interaction vertex as depicted in figure 2.8.

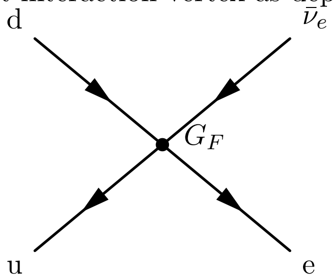

FIGURE 2.8: β-decay contracted to a 4-point interaction as described by Fermi theory

The accuracy of the EFT with respect to the full theory can be quantified by the *EFT error*. With an energy scale of a few hundred keV for the β-decay and with the mass of the W-boson functioning as cut-off scale the following error is obtained[41].

$$\Delta = \frac{\sigma_{\text{EFT}}}{\sigma_{\text{full}}} \sim \frac{E^2}{\Lambda^2} \sim 10^{-5} \tag{2.80}$$

Here it is shown that the error on the calculation in Fermi theory increases with E^2 which means that the validity of this effective field theory will remain as long as the W-boson is deeply virtual. This example shows that the Fermi theory is a good effective *top-down* approach for the electroweak theory as long as the energy regime is several orders below the mass of the mediating boson.

The illustration of Fermi theory with respect to the Standard Model gives a good idea of resp. an effective and underlying model. However, one can argue that the Standard Model is also only valid up to a certain energy level as it does not give explanations for several phenomena such as dark matter or the matter-antimatter asymmetry. So the Standard Model would be an effective field theory in the energy regime of $E \ll \Lambda \leq E_P$ and it is possible to say that all theories can be viewed as a never ending series of EFTs along the ladder of energy. In any case, computational efforts can substantially be reduced and out of reach energy regimes can be studied by dividing the phase space into regions and choosing the right effective approach.

2.6.2 Higgs Characterization Model

The Higgs Characterization model is an effective field theory that is used to model Higgs properties. The Lagrangian is constructed from a Standard Model Lagrangian excluding a Higgs sector and part describing a boson $X(J^P)$ where J and P denote resp. the spin and parity of the boson. The model does not assume any definite CP-properties and therefore allows for CP-mixing between the $X(J^+)$ and $X(J^-)$ states. In this study the spin-0 scalar model is chosen as previous studies have indicated that this is the most compatible with the found Higgs boson[43]. Any additional information on the Higgs Characterization Model can be found in the following reference[21]. The fermionic part of the Lagrangian is defined as

$$\mathcal{L}_0^f = \sum_{f=t,b,\tau} \bar{\psi}_f (c_\alpha \kappa_{Hff} g_{Hff} + i s_\alpha \kappa_{Aff} g_{Aff} \gamma_5) \psi_f X_0 \tag{2.81}$$

with

$$c_\alpha \equiv cos\alpha, s_\alpha \equiv sin\alpha \tag{2.82}$$

that parametrize the CP-mixing with the angle α. The SM coupling strength of the even and uneven parity scalar are denoted resp. by $g_{Hff} = m_f/v$ and $g_{Aff} = m_f/v$. The effective Lagrangian part that covers the interaction of the spin-0 boson with the vector bosons is defined as,

$$\begin{aligned}
\mathcal{L}_0^V = & \\
& \Big\{ c_\alpha \kappa_{SM} [\frac{1}{2} g_{HZZ} Z_\mu Z^\mu + g_{HWW} W_\mu^+ W^{-\mu}] \\
& - \frac{1}{4} [c_\alpha \kappa_{H\gamma\gamma} g_{H\gamma\gamma} A_{\mu\nu} A^{\mu\nu} + s_\alpha \kappa_{A\gamma\gamma} g_{A\gamma\gamma} A_{\mu\nu} \tilde{A}^{\mu\nu}] \\
& - \frac{1}{2} [c_\alpha \kappa_{HZ\gamma} g_{HZ\gamma} Z_{\mu\nu} A^{\mu\nu} + s_\alpha \kappa_{AZ\gamma} g_{AZ\gamma} Z_{\mu\nu} \tilde{A}^{\mu\nu}] \\
& - \frac{1}{4} [c_\alpha \kappa_{Hgg} g_{Hgg} G^a_{\mu\nu} G^{a,\mu\nu} + s_\alpha \kappa_{Agg} g_{Agg} G^a_{\mu\nu} \tilde{A}^{a,\mu\nu}] \\
& - \frac{1}{4} \frac{1}{\Lambda} [c_\alpha \kappa_{HZZ} g_{HZZ} Z_{\mu\nu} Z^{\mu\nu} + s_\alpha \kappa_{AZZ} g_{AZZ} Z_{\mu\nu} \tilde{Z}^{\mu\nu}] \\
& - \frac{1}{2} \frac{1}{\Lambda} [c_\alpha \kappa_{HWW} g_{HWW} W^+_{\mu\nu} W^{-\mu\nu} + s_\alpha \kappa_{AWW} g_{AWW} W^+_{\mu\nu} \tilde{W}^{-\mu\nu}] \\
& - \frac{1}{\Lambda} c_\alpha [\kappa_{H\partial\gamma} Z_\nu \partial_\mu A^{\mu\nu} + \kappa_{H\partial Z} Z_\nu \partial_\mu Z^{\mu\nu} + (\kappa_{H\partial W} W_\nu^+ \partial_\mu W^{-\mu\nu} + h.c.)] \Big\} X_0
\end{aligned} \tag{2.83}$$

with the (reduced) field strength tensors defined as,

$$
\begin{aligned}
V_{\mu\nu} &= \partial_\mu V_\nu - \partial_\nu V_\mu \\
G^a_{\mu\nu} &= \partial_\mu G^a_\nu - \partial_\nu G^a_\mu + g_s f^{abc} G^b_\mu G^c_\nu
\end{aligned}
\tag{2.84}
$$

with $V = A, Z, W^\pm$ and the dual tensor as,

$$\tilde{V}_{\mu\nu} = \frac{1}{2}\epsilon_{\mu\nu\rho\sigma} V^{\rho\sigma}. \tag{2.85}$$

The variable parameters are the CP-mixing terms c_α and s_α and the Wilson coefficients κ_i. All other terms are fixed to their SM value, see Table 2.2, such that the SM is retreived if $c_\alpha = 1$, κ_{SM} and all other coefficients set to $\kappa_i = 0$. Any deviation of these values gives us information on the CP-mixing and indication of new physics.

$g_{Xyy'} \times v$	ff	ZZ/WW	$\gamma\gamma$	$Z\gamma$	gg
H	m_f	$2m^2_{Z/W}$	$47\alpha_{EM}/18\pi$	$C(94cos^2\theta_W - 13)/9\pi$	$-\alpha_s/3\pi$
A	m_f	0	$4\alpha_{EM}/3\pi$	$2C(8cos^2\theta_W - 5)/3\pi$	$\alpha_s/2\pi$

Table 2.2: Values in units of v taken in by the couplings $g_{Xyy'}$ with $C = \sqrt{\frac{\alpha_{EM} G_F m_Z^2}{8\sqrt{2}\pi}}$[21]

2.6.3 Effective Lagrangian Morphing

In the previous sections it is shown what the characteristics of an Effective Field theory are. This section shows a derivation [18] that facilitates a theoretical basis for the morphing technique used in this thesis. In general the effective Lagrangian of such a theory can be assumed to be of the form

$$\mathcal{L} = \sum_i g_i \mathcal{O}_i. \tag{2.86}$$

The process of interest in this thesis has at tree level a scattering amplitude of the form

$$\mathcal{M} = \prod_{\mathcal{V}} \sum_{i \in \mathcal{V}} g_i \mathcal{M}_i \tag{2.87}$$

Here $\mathcal{V}$ denotes the set of vertices that occur in the Feynman diagram of the process, g_i are couplings that characterize the particles and their interactions partaking in the vertex and $\mathcal{M}_i$ the partial matrix elements.

In this analysis the focus is on a Higgs boson that is produced by two gluons and decays into two W-bosons i. e. one production and one decay vertex. So 2.87 becomes

$$\mathcal{M} = \sum_{i \in prod} g_i \mathcal{M}_i \sum_{j \in dec} g_j \mathcal{M}_j. \tag{2.88}$$

By combining equation 2.77 with 2.88 one obtains

$$\sigma_{i \to f} = a \cdot \int d\Omega | \sum_{i \in prod} g_i \mathcal{M}_i \sum_{j \in dec} g_j \mathcal{M}_j |^2 \tag{2.89}$$

By expanding the product of sums in a sum of products the cross section can be defined as a function of a set of coupling parameters $\vec{g} = (g_1, ..., g_n)$.

$$\begin{aligned} \sigma(\vec{g}) &= \int d\Omega \sum_i P_i(\vec{g}) P_i(\vec{\mathcal{M}}) \\ &= \sum_i c_i P_i(\vec{g}) \int d\Omega P_i(\vec{\mathcal{M}}) \end{aligned} \tag{2.90}$$

Here P_i denote polynomials of the form

$$P(\vec{x}) = \Re \Big(\prod_\alpha x_\alpha \Big). \tag{2.91}$$

The integral term forms the basis of a vector space for $\sigma(\vec{g})$. Because it is a linear vector space a change of basis can be used to span the space with respect to a different set of base vectors ξ_i

$$\int d\Omega P_i(\vec{\mathcal{M}}) = \sum_j b_{ij} \xi_j \tag{2.92}$$

for some set of coefficients b_{ij}. This redefines the cross section as

$$\begin{aligned} \sigma(\vec{g}) &= \sum_i c_i P_i(\vec{g}) \sum_j b_{ij} \xi_j \\ &= \sum_{i,j} P_i(\vec{g}) A_{ij} \xi_j \end{aligned} \tag{2.93}$$

If ξ_j is an element of the vector space it spans, i. e. can be expressed as a physical cross section σ_j, then it is possible to create the following set of linear equations.

$$\xi_k = \sigma(\vec{g}_k) = \sum_{i,j} P_i(\vec{g}_k) A_{ij} \xi_j \tag{2.94}$$

This can be rewritten as,

$$\delta_{jk} = \sum_{i} P_i(\vec{g}_k) A_{ij} \tag{2.95}$$

or in matrix notation,

$$A \cdot M = \mathbb{1} \tag{2.96}$$

with $M_{ik} = P_i(\vec{g}_k)$. A solution can be found for these linear equations if the matrix M is invertible. The sample set that satisfies this condition qualifies as a *morphing basis.* The solution is the set of coefficients A_{ij} that together with the base sample set can be used to interpolate to obtain cross section predictions for an arbitrary parameter set.

2.7 Beyond the Standard Model

The goal of the EFT coupling parameter measurement is to probe new physics beyond the Standard Model that solve the current unanswered questions. Theories that propose extensions on the Standard Model Higgs sector infer certain coupling strength modifiers, the same adjusting factors that are used in the Higgs Characterization model. Any non-zero value for coupling strength modifiers other then κ_{SM} implies deviation from SM and can be compared with the predictions proposed by Higgs BSM theories.

2.7.1 Issues of the Standard Model

In this section a few issues of the Standard Model are given as an example for the shortcomings and to illustrate the necessity of extensions. One of the most prominent and obscure problems in particle physics is *dark matter.* Dark matter is matter that does not interact via the electromagnetic interaction, barely interacts with other baryonic matter and has only been observed via its gravitational effects. It accounts for 85% of the matter content in the universe and was first proposed as a solution for the imbalance in rotational speed of galaxies and the gravitational force needed for such speeds. Current searches for an undiscovered new particle as a dark matter candidate, eg. a weakly interacting massive particle (WIMP), are still ongoing. A WIMP would be a good dark matter candidate as it would only interact with other particles through the weak or gravitation force. More information on dark matter can be found in references [27, 28]. Another issue is the *naturalness problem*. Because many questions are left unanswered by the Standard Model, it is believed that there lies a more fundamental theory at higher energies and that the Standard Model is an effective field theory. This means that natural coefficients in the Lagrangian terms must have the form

$$c_d = \alpha_d \Lambda^{4-d}. \tag{2.97}$$

where d denotes the dimension of the field operator, Λ is the cut-off scale and α_d is a parameter that should be of the order one. The natural coefficients c_d can be measurable quantities such as masses of gauge coupling constants. To reconcile the measured coefficient c_d and the cut-off scale Λ^{4-d} the parameter α_d sometimes needs to be adjusted to very large or small values. As an example, lets see what this means for the Higgs mass if one assumes the cut-off energy of the Standard Model to be at the Planck scale $M_P \sim 10^{19}$ GeV. The Higgs mass is roughly,

$$m_H \sim \alpha_2 M_P^2. \tag{2.98}$$

However, experiments revealed a Higgs mass of $m_H \approx 125.7$ GeV. The parameter α_2 needs to be *fine-tuned* to a very low value which seems *unnatural*. Other coefficients in the Standard Model need to be fine-tuned in a similar and unnatural way. Additional information on naturalness can be found in references [44, 45].

Lastly, one of the most pursued problems of all is the *unification of interactions*. In section 2.3 the unification of the weak and electromagnetic interaction was introduced. A Grand Unified Theory (GUT) in general refers to the additional unification of the strong interaction and a Theory of Everything (TOE) also includes a gauge theory of gravity. However, the masses of particles that would support a GUT are a few orders below the Planck scale $E_P \approx 1.2209 \times 10^{19}$ GeV i. e. well beyond the power of our current particle accelerators. Quantum gravity theories such as string theory are also expected to show direct effects only when approaching the Planck scale. Any inferences made on both matters need to be done with indirect measurements eg. in the framework of an EFT.

2.7.2 Higgs Sector Extensions

In this section a summary of the most popular Higgs sector extensions is presented. These are just a few of many and the description is very superficial. For a more detailed discussion on the matter can be found in references [46, 47].

Two-Higgs Doublet Model

The Two-Higgs Doublet Model (2HDM) states that the Standard Model should be extended with an additional electroweak doublet. The 2HDM results in two CP-even neutral h and H, a CP-odd neutral psuedoscalar A and two charged $H^{\pm}$ Higgs bosons. The 2HDM can be categorized in several versions depending on which fermions couple to which electroweak doublet and would provide a solution for the naturalness and strong CP problem i. e. the missing of CP-violation in strong interactions.[48]

Higgs-Portal Model

The Higgs-Portal Model states that the Higgs boson mediates the interaction between the dark matter sector. A Weakly Interacting Massive Particle (WIMP) strongly couples to the Higgs boson but weakly with the Standard Model. This makes dark matter detection possible in either a direct (decay to WIMP's) and indirect (Higgs produced by WIMP's but with SM decay products) way.[49, 50]

Minimal Composite Higgs Model

The Minimal Composite Higgs Model (MCHM) states that the Higgs boson is not a point-like particle but is a bound state of smaller constituents. The Higgs boson emerges as a composite psuedo-Goldstone boson (PGB), a bound state of a new strong interaction. The comparison with the original strong interaction denotes the similarity between the bound state of a composite Higgs and a pion, also a scalar particle.[51] Certain states of the psuedo-Goldstone boson can be a dark matter candidate and proposes a solution for the hierarchy problem i. e. the prediction that new physics will occur only near the Planck scale.

Minimal Supersymmetric Standard Model

The theory of supersymmetry proposes an additional supersymmetric particle for each particle of the Standard Model. This additional partner has the exact same mass and quantum numbers except for a spin difference of 1/2. The Minimal Supersymmetric Standard Model (MSSM) results in four additional Higgs bosons, provides dark matter candidates and would propose a solution for the naturalness and hierarchy problem. However, current observed data largely excludes MSSM and hints to other extensions that include more supersymmetric fields than the minimal amount of the MSSM. Additional information can be found in references [52, 53]

Chapter 3

Large Hadron Collider and ATLAS detector

In the past years enormous progression has been made in particle physics. The community of theoretical particle physics showed great creativity and effort in the construction of new theories that allowed us to calculate and compare with experiment. But these theories will remain nothing more then an idea if they are not supported by experimental evidence. However, the evidence of many theories, eg. a hypothesized particle, is only observable in higher energy scales that often require a rigorous experimental strategy and a lot of technical innovation.

With the awareness of this thought the *Conseil Européen pour la Recherche Nucléaire* (CERN) was founded in 1954 as an international organization that combines the intellectual power and resources to increase our scientific achievements in particle physics. Since then CERN has shown that collider experiments are very effective in the search for new physics and have made incredible discoveries thus far. The Large Hadron Collider is largest and most advanced collider experiment ever built.
The LHC is operated by a worldwide collaboration of physicists and is located in Geneva, Switzerland. The LHC hosts many different experiments that all have their own specific goals in high-energy physics. The ATLAS detector is the biggest detector and operates at one of the interaction points of the LHC to investigate a varying number of subjects such as new exotic particles or high accuracy measurements of known objects. The Higgs boson discovery was one of the major subjects of the ATLAS and CMS experiment. In this chapter an overview of the design and functionality of the ATLAS detector is given. Additional information can be found in references [6–9, 54, 55].

3.1 Large Hadron Collider

The Large Hadron Collider is a circular hadron collider build in a 27km long tunnel located 100 meters underground and has been operational since 2008. The accelerator is able to reach centre-of-mass energies of $\sqrt{s} = 14$ TeV for proton-proton collisions, $\sqrt{s} = 2.76$ TeV for heavy ion collisions and instantaneous luminosities of $L = 10^{34}$ cm^{-2}s^{-1} in proton-proton collisions.

The protons that are supplied for injection are created by stripping the electrons of hydrogen atoms with an electric field. The protons are first injected in the linear accelerator 2 (LINAC2) and then subsequently in the Booster, Proton Synchrotron (PS) and the Super Proton Synchrotron (SPS) to gradually ramp up to an energy of 450 GeV. With this energy the protons are injected into the LHC in bunches of 1.15×10^{11} protons per bunch and ramped up to energies of up to $\sqrt{s} = 13$ TeV. A beam is created by injecting the bunches 25 ns apart and can hold up to 2808 bunches per beam. To bend, focus and collide the beam the LHC is equiped with superconducting Niobium-Titanium magnets which create magnetic fields of up to 8.33 T when cooled down to a temperature of 1.9 K with the use of liquid Helium. The beams collide at one of the four interaction points where the following experiments will perform the data taking:

- **ATLAS** is a general purpose detector that focuses on the discovery of new particles, interactions beyond the Standard Model and precision measurements in electroweak physics.
- **CMS** is also a general purpose detector that focuses on the same scientific goals as ATLAS. However, it has a very different magnet system and uses other technical solutions.
- **ALICE** is a detector designed for heavy-ion collisions to study the physics of strongly interacting matter.
- **LHCb** is a detector designed to investigate the difference between matter and antimatter by studying the beauty quark.

In addition to these there is a whole collection of smaller experiments located in the interaction point caverns or on the above ground sites of CERN. When terminating and refilling with a new beam needs less effort and energy the beam is safely dumped at one of the dumping caverns. The beam dump absorber consists of a 7 m long segmented carbon cylinder, water cooled and surrounded by tonnes of iron and concrete shielding to safely stop the beam. A overview of the Large Hadron Collider and CERN complex is given in figure 3.1.

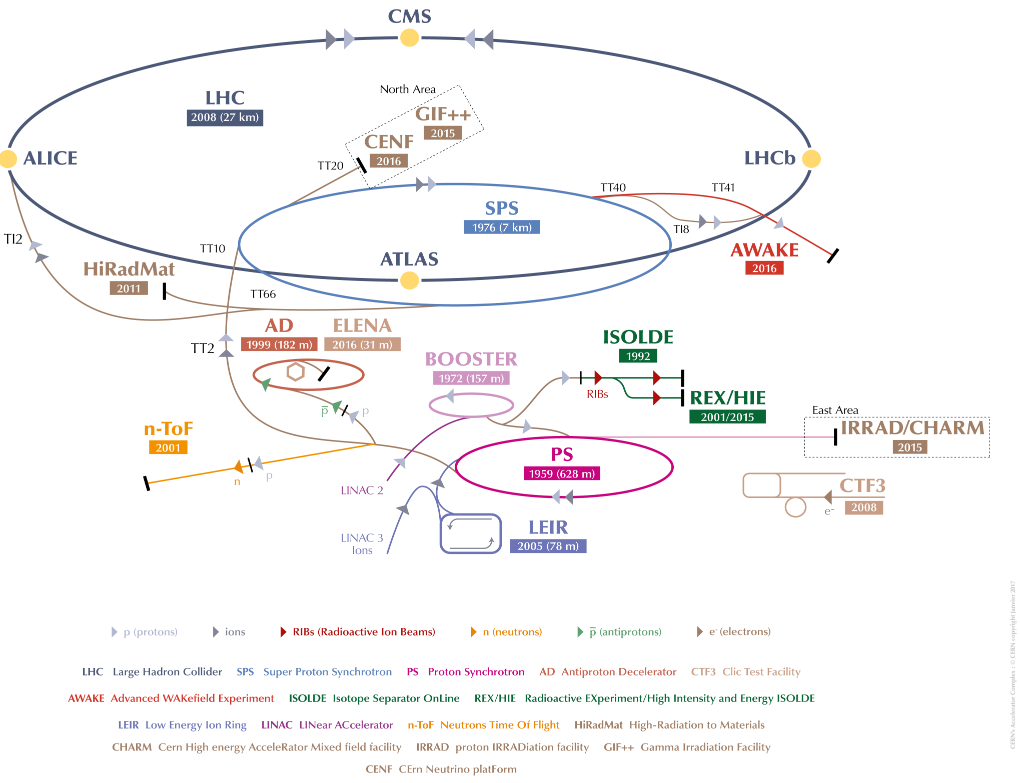

FIGURE 3.1: The CERN accelerator complex[5]

3.2 The ATLAS detector

The ATLAS (A Toroidal LHC Apparatus) detector is a general purpose detector of 44 m long, 25 m in diameter and a weight of about 7.000.000 kg. It is the largest detector at the LHC and is mainly focused on physics at the TeV scale. The detector has a cylindrical layer structure of subdetectors that each have their own specific task in particle detection and identification. A schematic representation of the detector is given on the previous page. Because of the geometry of the detector a cylindrical coordinate system is more practical than the more general cartesian coordinate system. The interaction point of the particle beams is located in the centre of the detector and is used as the origin of the cylindrical coordinate system:

- Parameter z - The z-coordinate is defined along the beam axis.
- Parameter θ - The polar angle, $\theta \in [0, \pi]$, is the angle from the beam axis.
- Parameter ϕ - The azimuthal angle, $\phi \in [-\pi, \pi]$, is the angle around the beam axis.

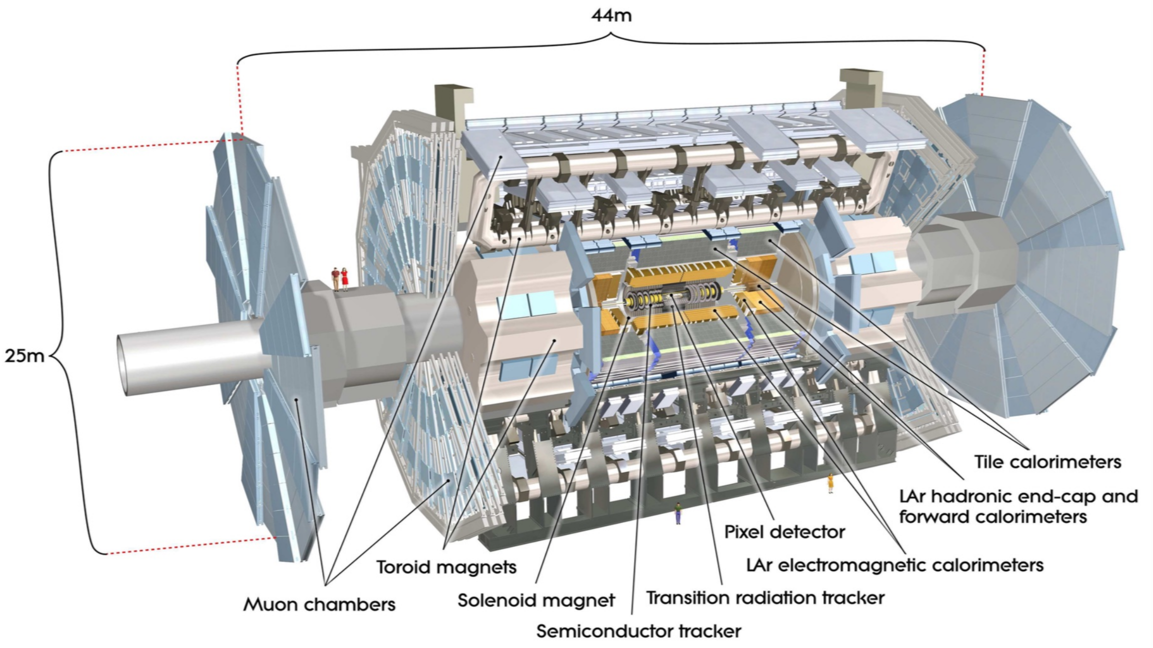

FIGURE 3.2: Schematic of the ATLAS detector[6]

As an addition it is common to use the psuedorapidity $\eta = -\ln\left[\tan(\frac{\theta}{2})\right]$ instead of the polar angle θ and the resulting distance coordinate $\Delta R = \sqrt{\Delta\eta^2 + \Delta\phi^2}$. It is also possible to define a Cartesian coordinate system where z is still along the beam axis, x points to the center of the ring and y points upwards.

3.2.1 Inner Detector

The purpose of the Inner Detector (ID) is to reconstruct the tracks and vertices of the particles that occur in the event and is located closest to the interaction point of all the subdetectors. Because of the strong magnetic field created by the magnet system the traversing charged particles experience a Lorentz force. By studying the curve of the trajectories a measurement can be made of the tranverse momentum p_T of the traversing particle. The Inner Detector has an outer radius of 115 cm, a total length of 7 m and is divided into four systems of which each uses a different but complementary technology. Schematics of the Inner Detector and its cross section are given in figure 3.3 and **??**.

Insertable B-layer (IBL)

This is the silicon tracker layer that is the closest to the interaction point with a radial extension of 31.0 < r <40.0 mm and a length of 332 mm. When charged particles traverse the active silicon material, electron-hole pairs will be created and will create a current under an applied bias voltage.

It was added to the Inner Detector during Long Shutdown 1 (2013-2015) to improve the vertex reconstruction and thus increase b tagging efficiency (See sections 4.1.2 and 4.4 for definitions). The IBL consists of 14 staves parallel to the beam line, each with up to 32 modules and a pixel size($\phi \times z$) of 50×250 μm$\times\mu$m.[7]

Pixel Detector (PD)

The Pixel Detector consists out of three concentric cylindrical layers and three end-cap disks of silicon pixel detectors at each side. The PD uses the same particle detection technology as the IBL but has a smaller pixel size of $50 \times 400(\phi \times z)$ μm$\times\mu$m.[56]

Semiconductor Tracker (SCT)

The SCT consists out of four concentric cylindrical layers and two end-caps with silicon strip modules. Instead of independent pixels the active silicon material has rectangular strips with a 80 μm pitch mounted on them to read-out the charge signal.[57]

Transition Radiation Tracker (TRT)

The TRT consists out of 370,000 straws that have a conductive outer coating, a golden plated tungsten sense wire in the centre and is filled with a gas mixture of xenon, carbondioxide and oxygen. It is the outer most part of the ID and additional to the tracking capabilities it also has a particle identification function based on transition radiation. A charged particle emits electromagnetic radiation proportional to its Lorentz factor γ when it crosses from one material to another. When the momentum of the particle is known one can calculate its mass and make a distinction between electrons and charged pions. This differentiation is one of the primary functions of the TRT.[58]

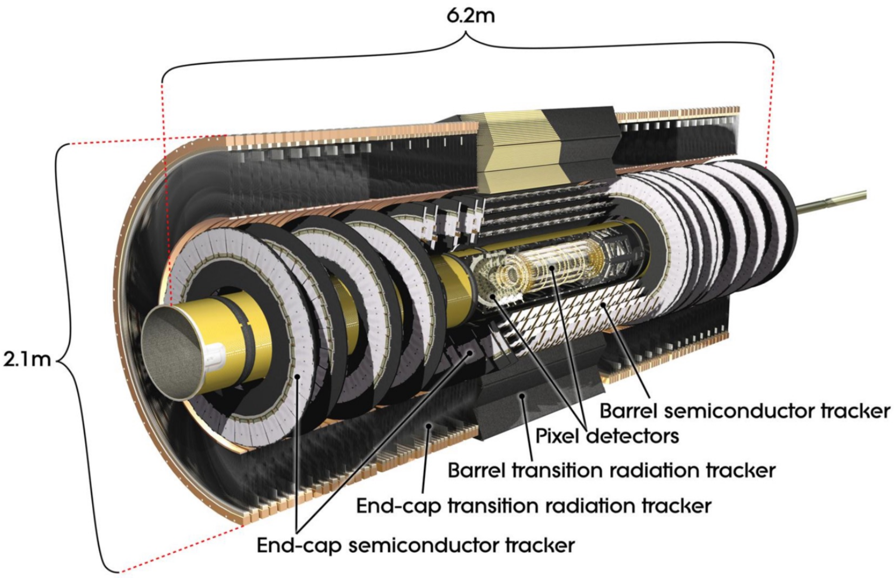

Figure 3.3: Schematic of the Inner Detector[6]

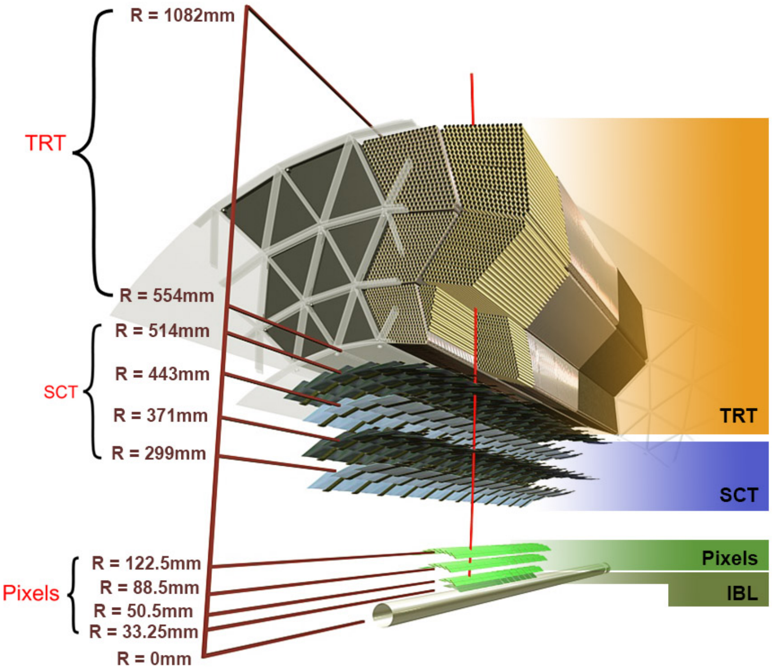

FIGURE 3.4: Schematic of the Inner Detector cross section[7]

3.2.2 Calorimeters

The goal of the calorimeter system of ATLAS is to measure the energy an incoming particle loses by triggering and absorbing particle showers. The calorimeter system consists out of an electromagnetic and hadronic calorimeter, where the former focuses on electromagnetic particles and the latter on hadronic particles. Both are a sampling calorimeter which means that they consist out of alternating layers of a *passive* and *active* medium. The passive medium is a high density material to trigger the showers and completely absorb the incoming particles while the active medium actually creates a detectable signal proportional to the input energy. A schematic of the calorimeter system is depicted in figure 3.5.

Electromagnetic Calorimeter (ECAL)

The main functionality of the ECAL is to measure the energies of electrons and photons. The ECAL consists of a barrel with an end-cap on either side. Both components have a accordion-like structure with layers of electrodes to read-out the electric signal, layers of lead as passive material and with the gaps in between filled with liquid argon to act as active material. With this geometry any cracks in the plates will have no influence on the measurements and will decrease the signal rise time i. e. the time for a signal to rise past a set threshold[59]. The ECAL is further segmented into cells with varying size $\Delta\eta \times \Delta\phi$ depending on its location in the calorimeter.

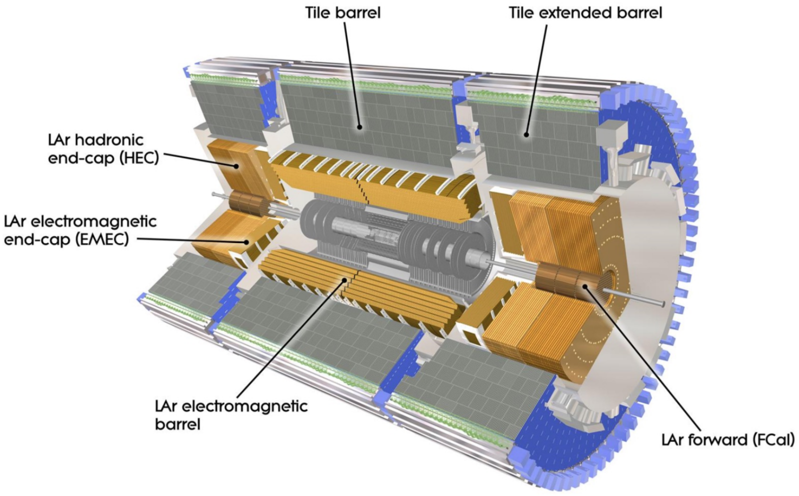

FIGURE 3.5: Schematic of the calorimeter system[8]

Hadronic Calorimeter (HCAL)

The main functionality of the HCAL is to measure the energies of hadrons and consists of a tile calorimeter, end-cap and forward calorimeter. The end-cap and forward calorimeter also use liquid argon as active material but have either copper or tungsten as passive material. The outer barrel however uses tiles of iron as passive and scintillating plastic as active material which are placed in the direction $\eta = 0$. This structure allows for good hermiticity and for the fibers to easily deliver the light signals to the photo-multiplier tubes (PMT) at the outside of the calorimeter.

3.2.3 Muon Spectrometer

The goal of the Muon Spectrometer (MS) is to detect muons and determine their tracks. Because most muons are not yet decayed, detected or stopped in the rest of the detector, the MS was added to perform stand-alone muon measurement capability. It is the outermost and largest part of the ATLAS detector and consists of three cylindrical layers and four vertical placed layers on each side that function as end-cap. The layers can be constructed from one of four chamber technologies, two for triggering and two for tracking (See section 3.3 and 4.1.2 for triggerering and tracking explanations). A schematic of the Muon Spectrometer is given in figure 3.6.

Monitored Drift Tube chambers

The MDT chambers are used for the precision measurement of muon tracks in all the layers except for the most inner end-cap layer. The detection element MDT is an aluminium tube with a tungsten-rhenium (W-Re) wire in the center and is filled with a argon-methane ($Ar\text{-}CH_4$) gas mixture. At the ends of the tubes there are oppositely charged electrodes that measure the drifting charges created by a gas ionizing muon.

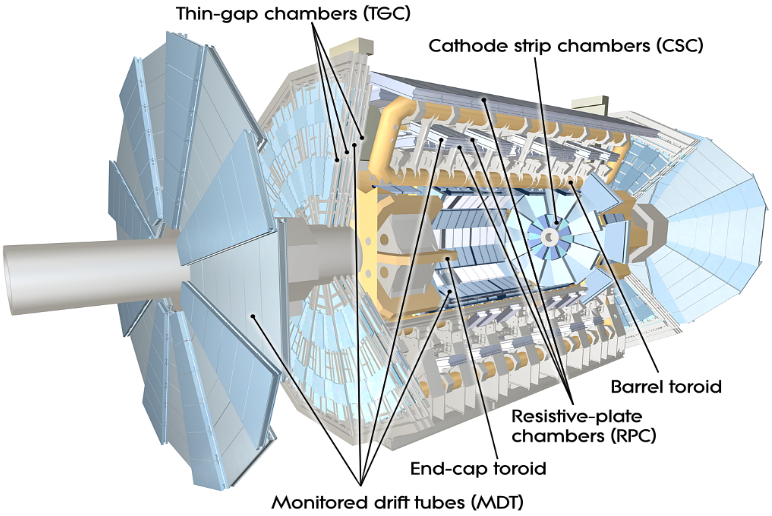

FIGURE 3.6: Schematic of the Muon spectrometer[9]

Cathode Strip chambers

The Cathode Strip (CS) chambers are also used for muon tracking but are only present in the end-cap layer closest to interaction point and pseudorapidities $\eta > 2$. The CS chambers are multiwire proportional chambers with a cathode strip and anode wire read-out of charges created by ionizing muons. The same wire material and gas is used but the resolution is higher compared to the MDT chambers.

Resistive Plate chambers

The Resistive Plate (RP) chambers are wireless gas-chambers filled with a mixture of tetrafluoroethane ($C_2H_2F_4$) and isobutane (C_4H_{10}) and with metal plates on either side for read-out. The RP chambers are only placed in the barrel with two on either side of the middle MDT chamber layer and one on the outside of the outer MDT chamber layer.

Thin Gap chambers

The Thin Gap (TG) chambers are only used in the end-cap and are all located near the first and second end-cap layer. The TG chambers have a similar structure as the Cathode Strip chambers but have a anode-wire pitch and anode-cathode distance that are not the same and use a gas mixture of CO_2 and n-pentane ($n\text{-}C_5H_{12}$).

3.2.4 Magnet System

The goal of the magnet system is to create a magnetic field can bend the trajectory of the created charged particles to make the measurement of transverse momenta possible. The magnet system consists out of the Barrel Toroid, Central Solenoid Magnet and the End-cap Toroids. A schematic of the magnet system is given in figure 3.7.

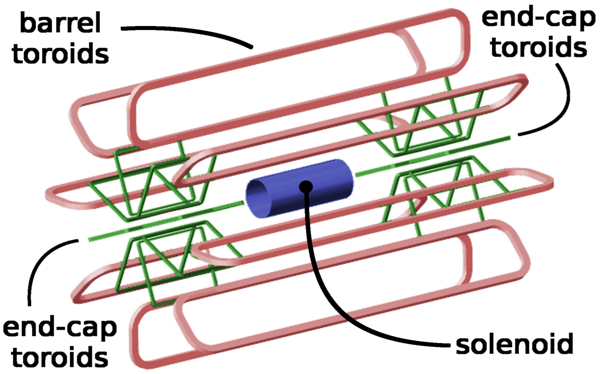

FIGURE 3.7: Schematic of the magnet system of the ATLAS detector[10]

Barrel and End-cap Toroids

The Barrel Toroid and End-cap Toroids consist each out of 8 superconducting coil magnets that provide a magnetic field for the Muon spectrometer. The superconducting wires are made from a NbTi/Cu alloid that is cooled to a temperature of 4.5 K by a cryostat system with liquid helium. The magnetic system can deliver a magnetic field of up to 4 T.

Central Solenoid Magnet

The Central Solenoid Magnet is a 2.4 diameter coil that provides a magnetic field for the Inner Detector. The superconducting wires are made from NbTi/Cu with a aluminium stabilizer to minimize the thickness of the solenoid for the calorimeter system but keep electrical stability. Because of its vicinity to the ECAL it is integrated with the LAr cryostat system to keep the solenoid at a temperature of 4.5 K. The solenoid can deliver a magnetic field of up to 2 T.

3.3 Trigger system of ATLAS

The goal of the trigger system is to select the events of interest, acquire the data of these events and discard the rest of the signals created in the sub detector. The rate of events during *pp* collisions is roughly 30 million per second and one event amounts up to about 1 Mb of data. However, only a fraction of the events are interesting for our physics analysis. To make a selection the ATLAS detector has a trigger system that contains two levels.

Level 1 Trigger
L1 is hardware-based trigger of custom made electronics which reduces the event rate from approximately 30 MHz to 100 kHz. Cones of space originating from the interaction point into the detector are selected as Regions of Interest (RoIs) by using information from the calorimeter and muon spectrometer. This level acts on an event in a decision time of 2.5 μs

High-Level Trigger
The HLT is a software-based trigger which uses the information gathered in L1 and sophisticated selection algorithms to reduces the event rate from 100 kHz to approximately 1 kHz. These selections are made in a processing time of 200 ms.

The criteria that are imposed on the events in these trigger levels can vary from kinematic thresholds to geometry or track selection. After the HLT has selected the final events of interests the data is saved on disk at the computer facilities of CERN for later retrieval, reconstruction and analysis.

3.4 Monte Carlo Generators & Simulation

Monte Carlo data has become an indispensable part of almost every analysis in high energy physics. Both experimentalists and theorists use them to make predictions and develop strategies for the collider experiments to search for new physics and make precision measurements. This section gives an general description of Monte Carlo event generation and ATLAS detector simulation.

3.4.1 Monte Carlo Event Generation

The Monte Carlo Event Generators are used to simulate the proton-proton collisions at the LHC before any interaction with the detector. There are many different types of event generators but in general their process can be divided in the following steps:

1. Hard process
2. Parton shower
3. Underlying event

4. Hadronization

5. Unstable particle decays

Hard process

The first step in the generation of Monte Carlo data is simulating the hard scattering on parton-level and computing the matrix elements up to a chosen perturbation order of accuracy. In case of proton-proton collisions it is assumed that only one of the incoming partons, i. e. gluons or quarks, take part in the hard scattering with the remaining partons as *spectators*. *Parton Distribution Functions(PDFs)*[60] are used to describe the incoming partons and lowest order perturbation theory is then used to calculate the probability distribution of outgoing partons. Next-to-leading order corrections are often needed for e. g. multi-jet final states and can be applied with additional dedicated algorithms which are implemented in various matrix-element generators. The most widely used generators nowadays are `ALPGEN`, `AMEGIC`[61], `Comix`[62], `CompHEP`[63], `HELAC`[64], `MadGraph`[65] and `O'Mega`[66].

Parton shower

The final state particles generated in the hard scattering process may proceed into additional hard scattering processes. Similar to electrons radiating photons in case of Bremsstrahlung can the partons emerging from the collision both radiate gluons. The highly energetic particles cascade in a shower of partons and evolve to lower momentum scales until perturbation theory breaks down. The simulation of these processes and their cross sections are performed by programs such as `HERWIG`[67], `Pythia`[68] and `Sherpa`[69].

Hadronization

Quarks and gluons cannot move freely because of color confinement, the concept that color charged particles cannot be isolated. After perturbation theory breaks down the partons hadronize into final state hadrons. The processes fall into what is called the *soft regime* of QCD and cannot be derived from first principles. Instead, it is modeled by fragmentation functions that are obtained from observed data.

Underlying event

The event generation process starts with a single parton extraction from each of the hadrons. However, the remaining spectator partons also evolve, hadronize and end up among the final state hadrons. These processes are referred to as *underlying events(UE)* and must be modelled to accurately measure the high momentum-transfer processes. Perturbative QCD no longer holds here as well and brings the need for alternative modelling techniques. Generators such as `HERWIG 7`[70], `Pythia 8`[71] and `Sherpa` contain models for the UE.

Unstable particle decays

Many of the final state particles that are created during and after the hadronization are stable enough to reach the detector. However, some have insufficient long life-time so that they decay before they can be detected. Additional dedicated programs are used to model particles such as b-hadrons and τ-leptons.

3.4.2 ATLAS Detector Simulation

Just like with any other measurement apparatus does the ATLAS detector also have its characteristics and limitations. An accurate simulation of the detector response is therefore important to give a realistic benchmark for the observed data. The ATLAS simulation software is based on a `Geant 4` simulation toolkit[72] and is integrated in the ATLAS common analysis framework Athena. To reduce computational requirements for detector simulation, several fast simulation approaches have been developed under shared name `ATLFAST`[73] and `FAST-G4`[74]. However, as one can see in figure 3.8, the majority of computational resources is still reserved for the generation and simulation of Monte Carlo data samples. This limitation motivates the usage of alternative methods that require less computation and storage such as used in this thesis, *Effective Lagrangian Morphing*.

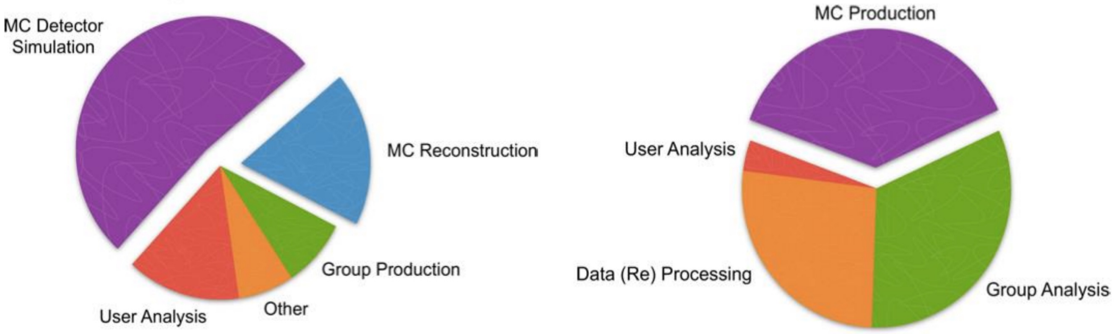

FIGURE 3.8: Overview of ATLAS LHC Computing Grid CPU[left] and disk[right] usage.[11]

Chapter 4

Object Reconstruction and Particle Identification

In the previous chapter it is shown that the ATLAS detector is a vast and complex machine. By segmenting the functionality over different parts it tries to capture all the information that is generated during the particle collisions with the highest accuracy possible. The next step is to take all these observations and use it to make a physical and coherent picture. Each particle leaves a different trace in the detector and can therefore be reconstructed based on characteristic detector signals. This is done with the ATLAS reconstruction software framework that is used for both the observed data that passed the online trigger levels and Monte Carlo data that has been processed by the Geant4 ATLAS simulation framework.

4.1 Tracks and Vertices

A proton-proton collision creates many different particles and accompanying interactions. It is therefore important to distinguish all the charged-particle trajectories (tracks) and their origins (vertices) to avoid ambiguity in the physical processes. Any additional information on track and vertex reconstruction can be found in the following references [12, 13, 75].

4.1.1 Track Reconstruction

The tracks are reconstructed by the *New Tracking* software framework (NEWT) which is made up from two main sequences, an *inside-out* and an *outside-in* tracking algorithm. The inside-out sequence uses the hits in the inner silicon pixel layers as seed for the track searching algorithm while the outside-in sequence starts at the TRT. Additionally to NEWT, a *second stage pattern* recognition is deployed to find decay points and tracks of long-lived neutral strange particles i. e. V0 vertices and kink objects due to brehmsstrahlung. Any additional information on track reconstruction can be found in reference [76].

The inside-out sequence starts in the Pixel detector and SCT with a *connected component analysis* (CCA) that groups the pixels and strips in the same sensor with a deposited energy above a certain threshold and with a common edge or corner. Each of these clusters gets a three-dimensional coordinate referred to as a *space-point* that represents the traversing of a charged particle.

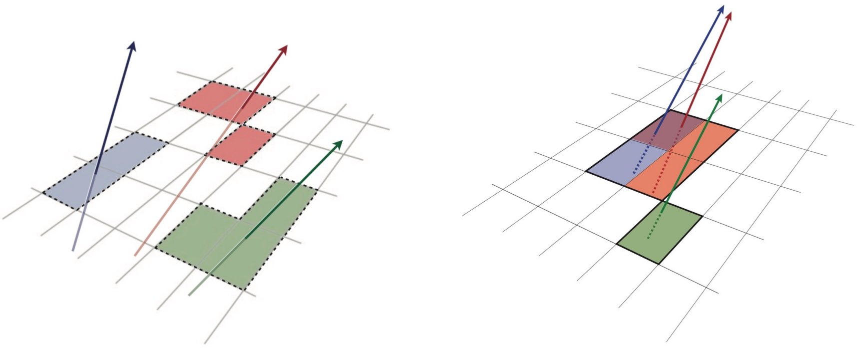

FIGURE 4.1: Illustration of (left) single-particle pixel clusters and (right) a merged pixel cluster due to very collimated charged particles. The colours indicate energy deposits of different charged particles.[12]

Combinations of three space-points are made called *track seeds* using a helicoidal fit. A *combinatorial Kalman filter* is then used to extend the space-point combinations with additional space points in the remaining layers of the Pixel detector and SCT.

The created track candidates get a track score assigned based on the amount of holes, an expected but missing space-point w.r.t. the track, the χ^2 of a preliminary fit and the logarithm of the momentum. The latter is to suppress tracks with low momentum that correlates to wrongly assigned clusters. The *ambiguity solver algorithm* then cuts away tracks based on that score and several other quality criteria. The remaining track candidates are subject to a high-resolution fit which is used one more time in the ambiguity solver algorithm to apply another cut in tracks. A dedicated tool then extends the remaining tracks to the TRT.

The outside-in sequence is an complementary reverse procedure for tracks that the inside-out sequence might have missed. New tracks are identified by a dedicated tool that recognizes and rejects tracks from the inside-out sequence. By backtracking track segments of the TRT that were not used in the inside-out sequence additional tracks are reconstructed.

4.1.2 Primary Vertex Reconstruction

The collection of final tracks are used as input for the reconstruction of the interaction points also known as vertices. Here we make a distinction between primary and secondary vertices, the former being the point of a hard inelastic collision between two protons and the latter being any interaction subsequent to the first collision eg. in a jet, decay chain, photon conversion or V0-decay. But the hard collisions are superimposed with several minimum bias events, events that pass the minimum bias trigger. It is expected that in the current high luminosity regime soft inelastic scattering interactions the same and surrounding bunch-crossings will overlap with the hard scattering processes of interest, forming so called *pile-up*. To model these pile-up events triggers need to be used that introduce minimum bias in the event selection with respect to the bias that the normal trigger system introduces.[77] The process of primary vertex reconstruction starts with the selection of trajectories according to the following requirements:

- $p_T > 400$ MeV and $|\eta| < 2.5$
- Number of hits ≥ 9 for $|\eta| < 1.65$ and ≥ 11 for $|\eta| > 1.65$
- Hits in the first two layers ≥ 1
- A maximum of 1 shared pixel and 2 shared SCT hits
- Holes in pixel detector $= 0$
- Holes in SCT ≤ 1

After the tracks have been chosen an initial vertex position set as seed to a fitting procedure. Each iteration assigns a weight to each tracks according to how compatible they are with the chosen vertex. The vertex is then refitted to the tracks with the new weights. These iterations continue until the vertex converges to a position at which moment the tracks that are incompatible with the vertex are removed from the vertex. The algorithm is repeated until either no unassociated tracks are left or no new vertices can be found. The vertex with the highest sum of squared transverse momenta is chosen as the *primary vertex* and the rest are labelled as *pile-up vertex*. Secondary vertex reconstruction is performed in a similar way but with a constrained vertex fit.

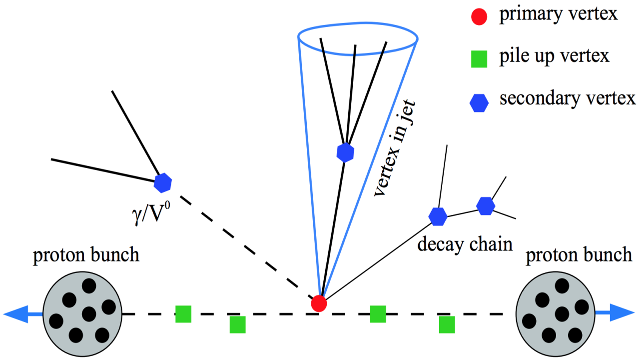

FIGURE 4.2: Schematic of vertex topologies during a proton-proton bunch crossing.[13]

4.2 Electrons and Photons

The next step after determining the tracks and vertices is to identify the particle assigned to each track and to make the first implications about the physical processes occuring at the vertices. The first types of physical objects that are identified and are crucial for many analyses are the electrons and photons. Electrons and photons play a vital role for both precision measurements, BSM searches and many Higgs analyses. Any additional information on electron and photon reconstruction and identification can be found in the following references [78, 79].

The first encounter of the reconstructed tracks the calorimeter system of which the electromagnetic calorimeter is specifically build to measure the energy of electrons and photons. Electron and photon reconstruction starts with building seed clusters out of the energy deposits in the EM calorimeter. Calorimeter signals created by photons and electrons are indistinguishable except for the fact that photons won't show any associated track. The EM-calorimeter system is divided into a grid of $\Delta\eta \times \Delta\phi = 0.025 \times 0.025$ towers in which the energy of all layers is summed. A sliding-window algorithm then scans for seed clusters of 3×5 towers with a total transverse energy higher than 2.5 GeV. An additional duplicate-removal algorithm is applied to nearby seed clusters to avoid multiple cluster assignment per photon or electron.

A Region of Interest (RoI) in the form of a cone is defined for seed clusters that pass loose requirements on lateral shower shape $R_\eta > 0.65$ and hadronic leakage $R_{Had} < 0.1$. Standard track pattern reconstruction is performed using a pion hypothesis. If no track seed can be found for the RoI, an electron hypothesis is assumed that allows for up to 30% energy loss at each material surface. A global χ^2 fitter is then used to fit the tracks, initially with the pion hypothesis and the electron hypothesis in case of failure of the fit. The extrapolated tracks are then compared in (η,ϕ)-coordinates with the barycenter of the cluster, which is the energy equivalent of a center of mass. Passed tracks are then refitted with a Gaussian Sum Filter (GSF). In case of multiple track assignment to one cluster, tracks with more silicon pixel hits and closer to the cluster will get preference.

To accommodate different analyses needs the reconstructed electrons are identified by different likelihood-based identification criteria. The electrons are divided in three different classes based on the resulting identification efficiency:

- LooseLH - 95%
- MediumLH - 90%
- TightLH - 80%

The efficiencies are measured with data from $\sqrt{s} = 13$ TeV pp-collisions in 2015.[80].

A EM cluster without an associated track indicates an unconverted photon. A converted photon can be classified as a single- or double-track conversion and will give a indirect signal in the calorimeter system through the electrons and positrons originating from the conversion point. A single-track conversion occurs when either of the tracks has a very low p_T and therefore does not reach the calorimeter or the photon energy is sufficiently high that we can not distinguish the two tracks.

4.3 Muons

Muons are key to some of the most important results of the ATLAS experiment such as the discovery of the Higgs boson, measurement of its properties, other precision measurements and BSM searches. The muon reconstruction is performed based on signals in the Inner Detector, Muon Spectrometer and the calorimeters. They are not stopped but do leave small energy deposits in the calorimeter system. Additional information on the reconstruction and identification of muons can be found in the following reference [81].

The muon reconstruction starts by searching for hit patterns in the Monitored Drift Tube (MDT) chambers of the Muon Spectrometer. The hits are fitted with a straight line fit to create segments which are combined to create track candidates. This combinatorial search is seeded with segments from the middle layer of the MS and is then extended to the inner and outer layer. Tracks are formed by applying a global χ^2 fit on the added hits in the inner and outer layer and pass if a χ^2 threshold is exceeded. Fits are improved by removing hits with a large χ^2-contribution and adding new hits. The tracks reconstructed in the MS are extended with one of four algorithms depending on which subdetectors are used:

- Combined (CB) muons: Tracks are reconstructed independently in the ID and MS and a global fit combines the hits from both. An outside-in approach extrapolates the tracks form the MS to match a track in the ID. A complementary inside-out approach starts with a ID-track and extrapolated outwards. The global fit allows addition and removal of hits in the MS to improve the fit quality.
- Segment-tagged (ST) muons: Tracks of the ID are extrapolated to the MS and tagged as muons if it can be combined with at least one track segment in the MS.
- Calorimeter tagged (CT) muons: Tracks of the ID are extrapolated to the calorimeter systems and tagged as muons if an energy deposit can be associated to the muon track. This is mainly to recover for the uncovered spectrometry region of the MS.
- Extrapolated (ME) muons: Tracks of the MS are extrapolated to the beam region and accepted if it is compatible with the interaction point.

In case more than one algorithm assigns a muon to the same ID track the preference is first given to CB muons, then ST and lastly CT muons. In case of overlap with ME muons the track with the better fit quality and larger amount of hits is chosen.

4.4 Jets

Jets are collimated showers of hadrons that are a result of hadronized quarks and gluons created in the collisions. They play an important role in a variety of subjects and the energy measurement has a direct effect on the missing transverse energy measurement. The jets are reconstructed from energy deposits in the calorimeter system and tracks reconstructed in the ID. The reconstruction is mainly done by the anti-k_t algorithm where the input can either be ID tracks(track jets), calorimeter clusters(calorimeter jets) or a combination of both. Additional information on the reconstruction and identification of jets can be found in the reference [82].

The first step in the reconstruction of jets is clustering calorimeter cells based on their energy deposit. The clustering algorithm is seeded with cells with an energy deposit of at least 4σ and expanded with cells of at least 2σ, where σ is the measured electronic and pile-up noise of the cells. Finally, a cluster-splitting algorithm is used to compare local energy maxima to distinguish between overlapping clusters.

The calorimeter cell clusters are used as input for the anti-k_t algorithm. The algorithm groups the clusters together based on the distance between them d_{ij} and their distance to the beamline d_{iB}.

$$d_{ij} = \min((k_T^i)^{2p}, (k_T^j)^{2p})\frac{\Delta R_{ij}^2}{R^2} \tag{4.1}$$

$$d_{iB} = (k_T^i)^{2p} \tag{4.2}$$

k_T^i and k_T^j are the transverse momenta of the clusters i and j, p is a parameter set to -1 and R is a parameter set to 0.4. The ΔR_{ij} is defined as,

$$\Delta R_{ij}^2 = (y_i - y_j)^2 + (\phi_i - \phi_j)^2, \tag{4.3}$$

with y_i and y_j the rapidity and ϕ_i and ϕ_j the azimuthal angle of the clusters i and j. If $d_{ij} < d_{iB}$ the two clusters are combined to an object k and otherwise cluster i is defined as a jet. Special algorithms are applied to distinguish jets that originate from a b-quark based on impact parameters or secondary vertices.

4.5 Taus

The tau lepton is an important particle for both Standard Model processed and BSM searches. With a mass of 1.777 GeV, the tau is the heaviest of all the leptons has therefore a very short lifetime. The tau lepton decays before reaching the Inner Detector and has to be identified by its decay products. Because of its large mass is the tau the only lepton that can decay hadronically and generates most commonly one or three charged pions along with some neutral pions. The signal from these pions is very similar to a parton jet but can be distinguished based on some characteristics. Additional information on the reconstruction and identification of taus can be found in the following reference [83].

The decay products are first tagged as a calorimeter jet because of their similar signal. To distinguish the tau leptons from the parton jets a minimum transverse energy for tau lepton candidates is set to 10 GeV. Secondly, the tau decay modes give a collimated energy deposit in the calorimeter systems so a selection on jet cone width is set to $\Delta R = \sqrt{(\Delta\phi)^2 + (\Delta)^2} < 0.4$. Taus can be classified into single- or multiple-prong decays where the prong label states how many charged particles occur in the decay mode. The single-prong taus are selected based on the number of tracks within a cone $\Delta R < 0.2$. Dedicated identification of taus is done with a Boosted Decision Tree that is trained separately on single- and multiple-prong taus with a set of discriminating variables.

4.6 Missing Transverse Energy

In the laboratory frame the sum of momenta for all the physical objects should equal to zero. However, the ATLAS detector is not able to detect every particle that is created in the proton-proton collisions. This results in an imbalance in the transverse momenta also known as the missing transverse energy (MET) and plays a crucial role in Higgs properties measurement and the search for dark matter or supersymmetric particles. Because many collision products are lost down the beam pipe a restriction is made to the missing transverse components. Additional information on the reconstruction of the missing transverse energy can be found in the following references [82, 84].

The missing transverse energy is primarily reconstructed from the signals in the calorimeter system. Because the calorimeter cells are organized in towers that point to the collision point, it is possible to define transverse components of the incoming energy. The E_T^{miss} of an event is a vectorial energy sum of the reconstructed physical objects. The E_T^{miss} is defined as

$$E_T^{miss} = \sqrt{(E_x^{miss})^2 + (E_y^{miss})^2} \tag{4.4}$$

with

$$E_{x,y}^{miss} = E_{x,y}^{miss,e} + E_{x,y}^{miss,\gamma} + E_{x,y}^{miss,\tau} + E_{x,y}^{miss,jets} + E_{x,y}^{miss,\mu} + E_{x,y}^{miss,soft} \tag{4.5}$$

where the components are calorimeter deposits for electrons(e), photons(γ), hadronically decaying tau-leptons(τ), jets, muons(μ) and soft objects. Soft objects represent calorimeter signals that are not associated to any of the previously defined reconstructed objects. Additional to the *calorimeter MET* reconstruction a complementary *track MET* reconstruction is applied. The missing transverse energy equals the negative vectorial sum of the missing transverse momenta in the relativistic limit $E = \sqrt{m^2c^4 + p^2c^2} \approx pc$. The missing transverse momentum is defined as

$$p_T^{miss} = \sqrt{(p_x^{miss})^2 + (p_y^{miss})^2} \tag{4.6}$$

with the vectorial sum

$$p_{x,y} = -\Big(\sum_{electrons} p_{x,y} + \sum_{muons} p_{x,y} + \sum_{jets} p_{x,y} + \sum_{soft\,objects} p_{x,y}\Big). \tag{4.7}$$

The tracks of the soft objects must satisfy a set of requirements to be added to the MET reconstruction.

- $p_T > 500$ MeV
- $|\eta| < 2.5$
- At least 1 pixel detector hit
- At least 6 pixels SCT hits
- Transverse impact parameter with respect to the primary vertex $|d_0| < 1.5$ mm
- Longitudinal impact parameter with repect to the primary vertex $|z_0 \times sin\theta| < 1.5$ mm

These are imposed to ensure the quality of the p_T measurement. The selection conditions are not a requirement for the tracks of leptons or jets.

Chapter 5

Higgs Physics at the LHC

One of the main motivations for the construction of the LHC was finding the long-sought Higgs boson. More than five years after the first observation of a Higgs-like particle[22, 23, 85] and many verifications later[86] many properties still remain unclear. In this chapter a short overview is given on dominant production and decay modes of the Higgs boson at the LHC and a summary of the latest results on signal strength and effective field theory coupling measurements by the ATLAS and CMS experiment.

5.1 Production Modes

The LHC can produce the Higgs boson in various ways. The dominant production modes are gluon fusion, vector boson fusion, Higgs strahlung, associated production with top or bottom quarks.

Each production mode has a corresponding expected cross section in proton-proton collisions depending on the centre of mass energy. In figure 5.2 the largest Higgs cross section contributions including order of accuracy (see section 2.2.4) are given. with Monte Carlo generators that can calculate matrix elements up to a certain order of accuracy. The calculations are different for each process and therefore computational effort differs resulting in a varying higher-order precision.

The largest contribution in Higgs production is the **gluon fusion(ggF)** process. The **gluon fusion** process contributes to almost 90% of the Higgs production and plays a central role in this thesis. Even though gluons are massless, the interaction is made possible through a virtual top loop as shown in the Feynmann diagram. The cross section has been calculated up to next-to-next-to-next-to-leading order (N3LO) QCD and next-to-leading order (NLO) electroweak corrections. The **vector boson fusion(VBF)**

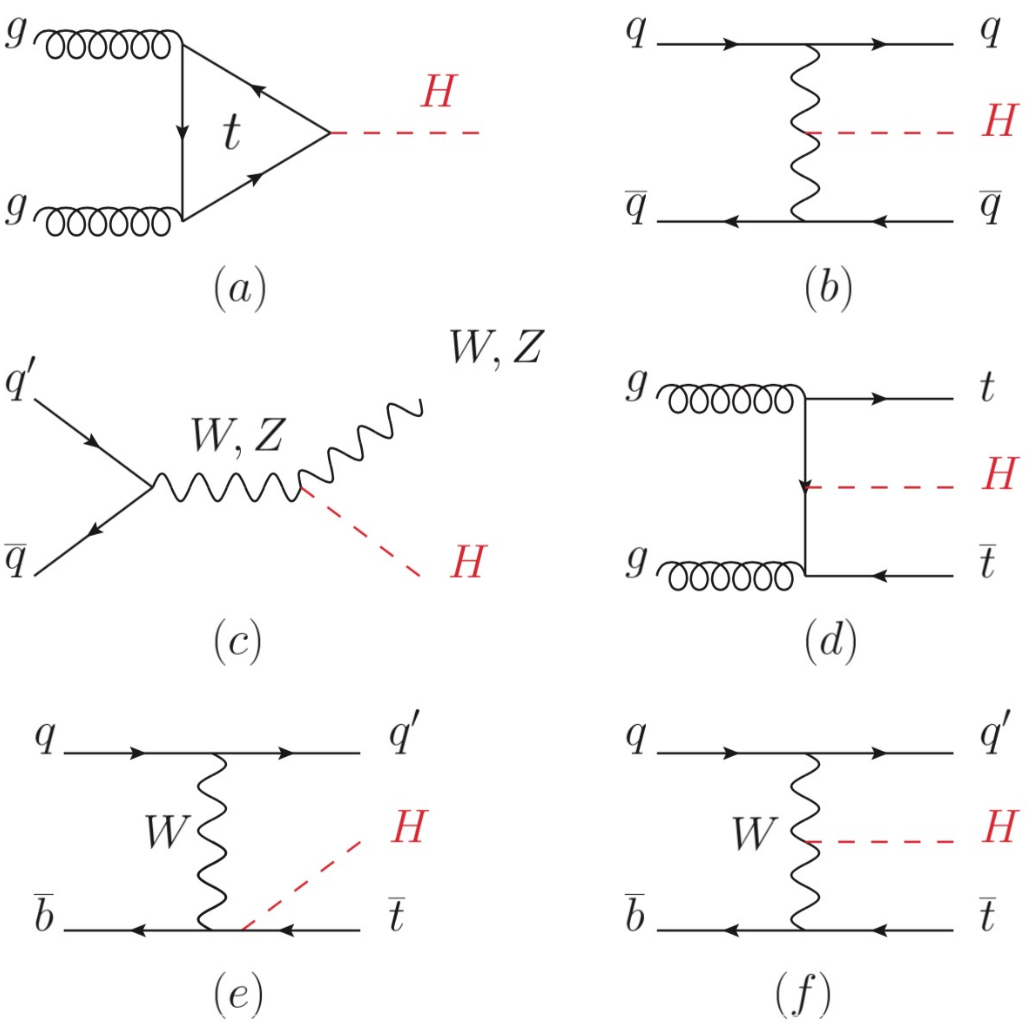

FIGURE 5.1: Leading order Feynmann diagrams for the dominant production modes at the LHC. a) Gluon fusion b) Vector boson fusion c) Higgs-strahlung d-f) Associated production with top or bottom quarks [14].

process is the second largest contribution to the production of Higgs bosons for a proton-proton collisions. A quark and antiquark both radiate off a vector boson of one type(W- or Z-boson). These vector bosons fuse into a Higgs accompanied by two highly energetic jets from the initiating quarks. The **Higgs strahlung(VH)** process is the next major production mode but its contribution is almost a factor 5 lower than the VBF process and is therefore substantially smaller. Two quarks produce a W- or Z-boson which then radiates of a Higgs boson. The last major contributions are from the **quark associated production(ttH/bbH)**. These channels give a direct probe to the Higgs to top/bottom couplings but have substantially lower production rates compared to the previous production modes.

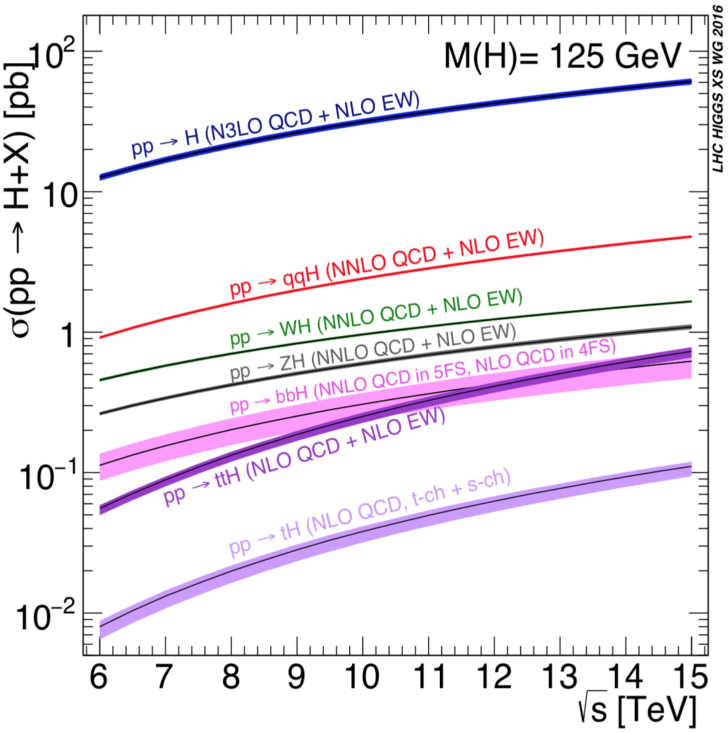

FIGURE 5.2: Theoretical predictions on Standard Model Higgs boson production cross sections including uncertainty [14].

5.2 Decay Modes

The Standard Model Higgs boson has a predicted life time of 1.6×10^{-22} s and therefore decays, just like many other heavy particles, before it exits the beam pipe. The understanding of the decay modes is therefore crucial for studies on the Higgs boson. However, a Higgs mass of 125 GeV makes decays possible to many different particles. The abundance of a specific decay process is quantified in a branching ratio, the fraction of Higgs bosons that decay through that process. A branching ratio for a decay to a final state A is defined as

$$BR(H \to A) = \frac{\Gamma(H \to A)}{\sum_i \Gamma(H \to X_i)} \tag{5.1}$$

where Γ is the partial width of the process and the denominator is a sum over all possible decay modes. The partial width is proportional to the masses of the particles the Higgs boson decays to. The dominant decay modes from largest branching ratio to lowest are $H \to b\bar{b}$, $H \to WW$, $H \to gg$, $H \to \tau\tau$, $H \to c\bar{c}$, $H \to ZZ$, $H \to \gamma\gamma$, $H \to Z\gamma$ and $H \to \mu\mu$.

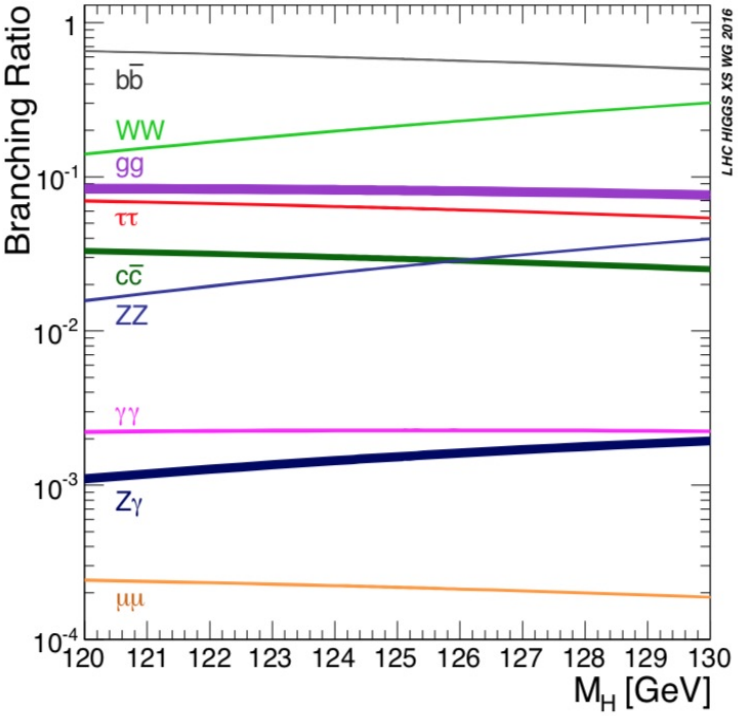

FIGURE 5.3: Theoretical predictions branching ratios for Standard Model Higgs boson decay modes including uncertainty [14].

The decay mode with the largest contribution is to two (anti-)bottom quarks. However, this channel is difficult to study because of the large QCD background caused by other jets. The channel can be made feasible with a Higgs strahlung production and first evidences have recently been found [87]. A Higgs boson produced by vector bosons and decaying leptonically gives a clean signal relative to the other channels. Decay modes to two gluons or two charm quarks are difficult as their occurrence is even rarer and are also associated with a big QCD background. The second most predominant decay mode is to two W-bosons and gives with its leptonic decay products a signature that is easier to distinguish from background. In this thesis the muons and electrons are selected as decay products as they are both sufficiently stable to be measured with respect to the taus which in general decay further into hadrons or other leptons before they reach the detector. The decays to two Z-bosons and photons also give plenty experimental possibilities because of the low background. Some first studies are performed with a decay to two taus and to two muons [88]. The contribution of the Z-boson and a photon decay is very rare and research is still in development.

5.3 Higgs Properties

The goal of the study on Higgs properties is to improve our understanding of the Higgs boson and look for effects beyond the Standard Model. According to the Standard Model, the Higgs boson is a CP-even scalar particle. Previous studies excluded the spin-1 hypotheses up to 99.999% confidence level and spin-2 hypotheses up to 99% [89]. The Higgs boson mass is measured as $m_H \approx 125.7$ GeV and implies a Higgs self-coupling constant of $\lambda \approx 0.13$.[90]. Other parametrizations that are valuable in the search for deviations from the Standard Model are the *signal strength* parameter and EFT couplings.

5.3.1 Signal Strength

In section 2.7 an impression is given on a few theories that could extend the Standard Model. In reality there is a large variety of such theories which can make theory specific tests cumbersome. However, a common method is to search for a new particle predicted by a theory. The observation of such a particle can be quantified with the *signal strength* parameter

$$\mu = \frac{\sigma_{\text{obs.}}}{\sigma_{\text{theo.}}} \tag{5.2}$$

with $\sigma_{\text{obs.}}$ the observed cross section and $\sigma_{\text{theo.}}$ its theoretical prediction. Any deviation from unity would indicate an observed deviation from the Standard Model. Signal strength measurements on the before mentioned production and decay modes have already been performed with Run 1 data taken at the ATLAS and CMS experiment.

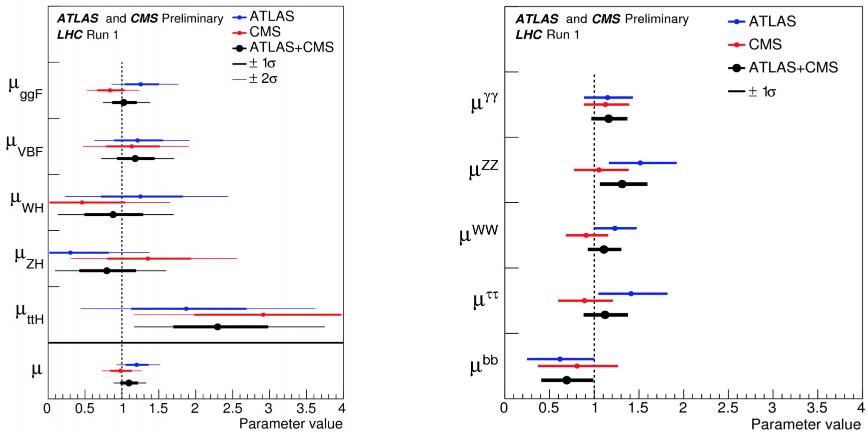

FIGURE 5.4: Results for the production (left) and decay (right) signal strengths from the combination of ATLAS and CMS. The results for each experiment are superimposed. The error bars indicate the 1σ (thick lines) and 2σ (thin lines) intervals. [15].

All the different production and decay modes are be combined in a global signal strength of $\mu = 1.09 \pm 0.07(\text{stat.}) \pm 0.04(\text{exp.syst.}) \pm 0.03(\text{th.bkg.})^{+0.07}_{-0.06}(\text{th.sig.})$ which states no significant deviation from the Standard Model.

The increased total integrated luminosity of Run 2 results in an improved measurement sensitivity. This does not only improve low-background analyses concerning diphoton[91] and double vector boson decay[1, 92] but also makes analyses possible that are more background dominated such as the recently measured $b\bar{b}$[93] or $\tau\bar{\tau}$[94] decay mode. The gluon fusion production to $W^{\pm}W^{\mp *} \rightarrow l^- \bar{\mu}_l l'^+ \mu_{l'}$ decay mode was also recently measured with a signal strength of $\mu = 1.21 \pm^{+0.12}_{-0.11}(\text{stat.})^{+0.18}_{-0.17}(\text{syst.})$.[1] Again no significant deviation from the Standard Model was observed.

5.3.2 EFT Couplings

The signal strength measurement is a good approach to test a single theory that predicts the existence of a particle, the Higgs boson. However, any deviation from the benchmark theory, e. g. the Standard Model including the Higgs boson, comes without any suggestion or hint on which alternative theory could be the right answer. Preferably one would like a model-independent approach that can be coupled to predictions of as many different BSM theories as possible. An effective field theory coupling measurement provides exactly this. Additionally, effective coupling parameters does not only include total signal rate, like the signal strength does, but also the shapes of differential distributions.

There are many different effective field theories that map the character of the Higgs boson. However, the effective Lagrangian approach is relatively new and therefore only few comparable studies have been conducted before this thesis. Previous studies in terms of the Higgs Characterization Model have mostly focused on the Higgs couplings to vector bosons. Expected and observed confidence intervals were set on these couplings with likelihood scans with an effective Lagrangian implementation.[16, 17] All parameters κ_i that are not explicitly mentioned are considered to be 0.

Coupling parameter	Observed	Expected
κ_{Agg}	± 0.43	0
κ_{AVV}	± 2.9	0
κ_{HVV}	2.9	0

Table 5.1: Best fit values for the coupling parameters κ_{Agg}, κ_{AVV} and κ_{HVV} as obtained from the negative log likelihood scans performed with 36.1 fb^{-1} of data at $\sqrt{s} = 13$ TeV collected at the ATLAS experiment.[16]

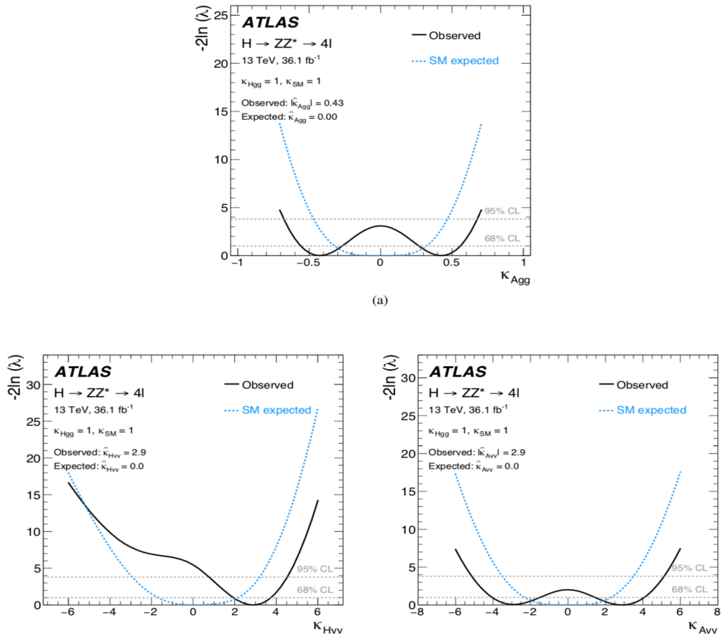

(a)

(b) (c)

FIGURE 5.5: Observed (solid black line) and SM expected (dashed blue line) negative log-likelihood scans for (a) κ_{Agg}, (b) κ_{HVV} and (c) κ_{AVV} coupling parameters using 36.1 fb^1 of data at $\sqrt{s} = 13$ TeV. The horizontal lines indicate the value of the profile likelihood ratio corresponding to the 68% and 95% CL intervals for the parameter of interest[16].

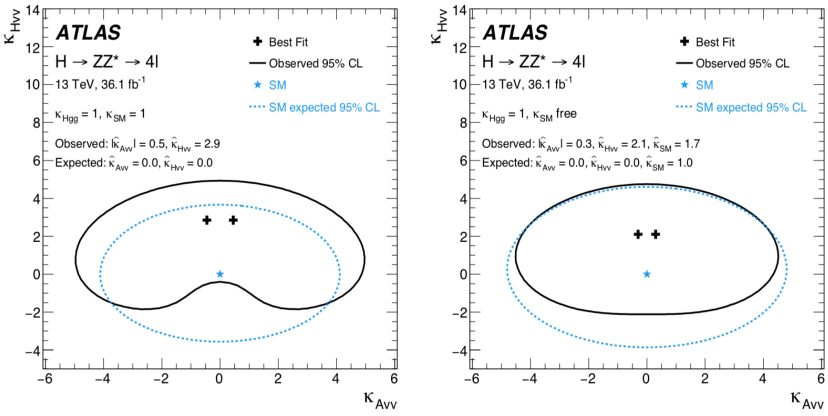

(a) (b)

FIGURE 5.6: Observed (black) and SM expected (blue) contours of the two-dimensional negative log-likelihood at 95% CL for the κ_{HVV} and κ_{AVV} coupling parameters with 36.1 fb^1 of data at $\sqrt{s} = 13$ TeV. The coupling κ_{Hgg} is fixed to the SM value of one in the fit. The coupling κ_{SM} is (a) fixed to the SM value of one or (b) left as a free parameter of the fit (b).[16].

Figure 5.5, 5.7 and table 5.1 show the results of vector boson effective coupling measurements in the $H \to ZZ^* \to 4l$ decay channel with the ATLAS detector. The constraints and best-fit values show no significant deviation from the Standard Model.

A sensitivity study was performed for a likelihood scan of $\cos\alpha$ and the ratio $\frac{\kappa_{Agg}}{\kappa_{Hgg}}\tan\alpha$ on an Asimov dataset. The study targeted the ggF-2j production, $H \to W^{\pm}W^{\mp *} \to l^{-}\bar{\nu}_l l'^{+}\nu_{l'}$ decay mode and also used the likelihood scan approach with an effective lagrangian implementation.

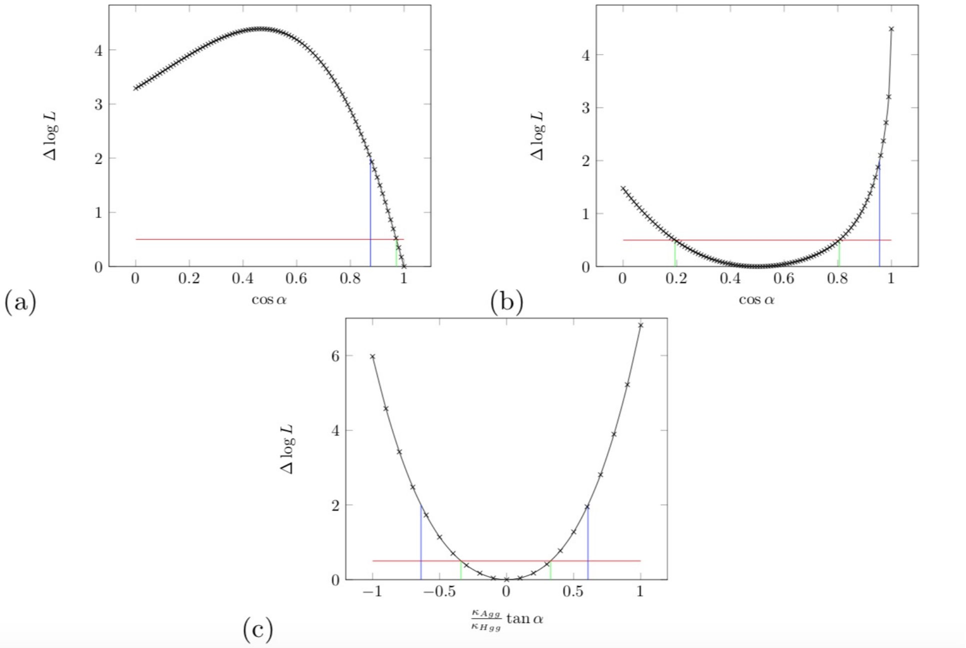

FIGURE 5.7: The sensitivity obtained in this analysis for the parameter scan of (a) $\cos\alpha$ with an Asimov dataset created for the SM CP even Higgs boson, (b) $\cos\alpha$ with an Asimov dataset created for a CP mixed Higgs boson and (c) the ratio $\frac{\kappa_{Agg}}{\kappa_{Hgg}}\tan\alpha$ for an Asimov dataset created for the SM CP even Higgs boson. The green lines indicate the 1σ confidence interval and the blue lines indicate the 2σ confidence interval.[17]

The Asimov data set for a SM CP even Higgs boson corresponds to $\kappa_{Hgg} = 1$, $\kappa_{Agg} = 0$ and $\cos\alpha = 1$ and for a SM CP mixed Higgs boson to $\kappa_{Hgg} = 1$, $\kappa_{Agg} = 1$ and $\cos\alpha = \frac{1}{\sqrt{2}}$. The results indicate that a precision measurement of these effective coupling parameters can be achieved with a comparable precision to previous measurement methods.[17] Another effective field theory framework used to probe the properties of the Higgs boson is the Standard Model Effective Field Theory (SMEFT). The operators and therefore coefficients are defined in two different bases, the strongly-interacting light Higgs (SILH) and the Warsaw basis.[95] Both have an implementation in Madgraph and constraints placed on their effective coupling parameters by previous studies.[96, 97]

Chapter 6

Signal Strength Analysis

As mentioned in the previous chapter, the first line of attack in the search for deviation from the Standard Model is measuring the signal strength. This chapter describes the precision measurement of the signal strength for a Higgs boson in the gluon fusion $H \to W^{\pm}W^{\mp *} \to l^{-}\bar{\nu}_{l}l'^{+}\nu_{l'}$ channel. After selecting the decay topology, cuts are applied to reject as many background events as possible and increase the signal-to-background ratio. A *profile likelihood method* is used to extract the observed *signal strength* μ and its significance expressed in a p-value.

6.1 Data and Monte Carlo Samples

The data that is used for analysis is from the 2015 and 2016 data taking period and corresponds to a total integrated luminosity of 36.07 fb^{-1}. The data is collected by the ATLAS detector during proton-proton collisions at a centre of mass energy of $\sqrt{s} = 13$ TeV. To interpret the data, theoretical predictions of both signal and background events are simulated with Monte Carlo techniques that model hard scattering, parton showering, hadronisation, underlying events and pile-up. After the events are generated on truth level they are passed through a full simulation of the ATLAS detector and are subsequently reconstructed and digitized with the software frameworks discussed in Chapter 4.

6.1.1 Signal Samples

Monte Carlo samples have been generated to simulate the ggF + 0/1 jets signal. The events were generated at next-to-next-to-leading order with POWHEG[98] and subsequently showered with Pythia8[71]. Other signal samples that are included are the vector boson fusion process(VBF) and an additional signal for ggF and VBF processes of which the Higgs decays into two taus(Htt). Higgs production processes such as Higgs strahlung(VH) and quark associated production(ttH, bbH and tHx) are not included as their contributions are quite small.

6.1.2 Background Samples

The background processes that are included consist of other production processes that decay with a similar leptonic decay. The primary backgrounds are productions of V/γ^*, top quarks and electroweak bosons. The background samples are simulated with different Monte Carlo generators and varying precision. Both the signal and background samples are listed in table 6.1.

Process	Generator	σ[pb]	Precision
$ggF\ H \to WW$	POWHEG+Pythia8	1.102	NNLO
$VBF\ H \to WW$	POWHEG+Pythia8	0.0808	NNLO
$gg \to ZZ \to 4l$	Sherpa	0.021	NLO
$q\bar{q}/g \to WZ \to l\nu ll$	Sherpa	13.1	NLO
$q\bar{q} \to ZZ \to 4l$	POWHEG+Pythia8	1.26	NLO
$q\bar{q} \to ZZ \to llqq$	POWHEG+Pythia8	2.27	NLO
$q\bar{q} \to ZZ \to ll\nu\nu$	POWHEG+Pythia8	0.92	NLO
$q\bar{q} \to WW \to l\nu l\nu$	Sherpa	4.58	NNLO
$gg \to WW \to l\nu l\nu$	Sherpa	0.38	NNLO
Wt leptonic	POWHEG+Pythia	3.58	NLO
$t\bar{t}$ leptonic	POWHEG+Pythia	76.9	NNLO + NNLL
$(W \to l\nu)\gamma$	Sherpa	$1.065 \cdot 10^3$	NLO
$(Z \to ll)\gamma$	Sherpa	$0.297 \cdot 10^3$	NLO

Table 6.1: Included signal and background processes, corresponding Monte Carlo generators, cross sections and precisions

6.2 Object Selection

The required physical objects in the final state are two charged leptons, two neutrinos and a maximum of one jet. Events with these objects should have at least one primary vertex and two associated tracks with a transverse momenta of $p_T > 400$ MeV. In case of multiple primary vertices, the one with the largest sum of transverse momenta squared of the tracks will get preference. The technical implementation of sample processing, event selection and plotting is handled with the ROOT-based `Common Analysis Framework (CAFCore)`. Any additional information on the framework can be found in reference [99].

6.2.1 Electrons

The analysis requires exactly one electron and one muon in an event. The electrons must have a minimum transverse energy of $E_T > 15$ GeV and must pass additional identification efficiency criteria based several discriminating variables depending on its transverse energy. Electrons must pass either the *TightLH* or a *MediumLH* identification efficiency criterium depending on if the transverse energy is resp. lower or higher than 25 GeV. The psuedorapidity of the tracks must be in the range $|\eta|< 2.47$ excluding the gap $1.37 < |\eta|< 1.52$ between the barrel and end caps of the liquid argon calorimeter.

6.2.2 Muons

The muons are reconstructed with the *combined muon* algorithm and are required to pass a *Medium* identification criterium that is designed to minimize the systematic uncertainties of muon reconstruction and calibration and avoid muons coming from pions and kaons. Similar to the electrons, a minimum transverse energy of 15 GeV and maximum track psuedorapidity of 2.5 is required. To ensure that the electrons and muons originate from the primary vertex the longitudinal impact parameter z_0 must satisfy $|z_0 \text{sin}\theta|< 0.5$ mm, where θ is the polar angle of the track with respect to the beam line.

6.2.3 Jets

In case the event contains one reconstructed jet it is required to be in the rapidity range $|\eta|< 4.5$ and have a minimum total transverse momentum of 25 GeV. This requirement changes to a minimum of 30 GeV for jets in the range $2.4 < |\eta|< 4.5$. Jets that approach an electron within a cone size of $\Delta R < 0.2$ are removed to avoid double counting as both have a chance to be mistaken for each other in the reconstruction. In case the jet approach is within a cone of $0.2 < \Delta R < 0.4$ the electron is discarded instead. In case of a muon and a cone of $\Delta R < 0.2$ the jet is discarded only if the jet has less then three associated tracks and for a cone of $0.2 < \Delta R < 0.4$ the muon is only discarded if the jet has at least two associated tracks.

6.3 Event Selection

To optimise the seperation between signal and background events and between different Higgs EFT scenarios a set of cuts is applied on the events. Orthogonal signal(SR), control(CR) and validation(VR) regions are defined to resp. apply the fit, estimate background and subsequently validate the background estimation.

6.3.1 Pre-selection

The pre-selection is a set of general cuts that aim to improve the overall quality of the events as well as select the decay channel of choice.

- **Good Run List Selection (GRL)** Select events from a list of runs that satisfy quality constraints. "Bad" runs can be because of unstable beams, faulty magnet system or a switched-off subdetector.
- **Trigger Selection** Select events based on the lepton identification efficiencies as stated in the previous section.
- **Jet Cleaning** Select jets that satisfy quality constraints as stated in the previous previous section.
- **Vγ/Vjets overlap removal** Remove events that are tagged with a photon and a jet.
- ≥ 2 **leptons** Select events with at least two leptons of which the leading leptons must have opposite flavor and sign.
- $p_T^{lead} > 22$ **GeV** Select events where the leading lepton, the lepton with the highest p_T, has a transverse energy of $p_T > 22$ GeV.
- $p_T^{sublead} > 15$ **GeV** Select events where the subleading lepton, the lepton with the second highest p_T, has a transverse energy of $p_T > 15$ GeV.
- $m_{ll} > 10$ **GeV** Select events with a the dilepton invariant mass of $m_{ll} > 10$ GeV.
- $p_T^{miss} > 20$ **GeV** Select events with a missing transverse momentum of $p_T^{miss} > 20$ GeV.
- **Fake factor** A factor is applied to remove jets that faked a lepton. This factor is calculated by a data-driven method that models events with fake leptons. Additional information on the fake factor method can be found in reference [100].

6.3.2 Signal Region

The signal region is selected by applying cuts additional to the pre-selection. This region will be used to apply the likelihood fit to extract the signal strength. Events are selected requiring at most one jet which defines the first two categories signal regions, $N_{jet} = 0$ and $N_{jet} = 1$. The two jet multiplicities result in different background compositions so two categories require two sets of event selections.

$N_{jet} = 0$:	$N_{jet} = 1$:
$\Delta\phi_{ll,E_T^{miss}} > 1.57$	$N_{b-jet} = 0$
$p_T^{ll} > 30$ GeV	$\max_i m_T^{l_i} > 50$ GeV
	$m_{\tau\tau} < m_Z - 25$ GeV
	$m_{ll} < 55$ GeV
	$\Delta\phi_{ll} < 1.8$

Table 6.2: Event selection criteria for the two signal region categories

In the $N_{jet} = 0$ category, the Higgs boson is not boosted[18] i. e. has a low momentum along the beam line but a large momentum perpendicular to the beam line. This motivates the selection of events with a relatively high transverse momentum p_T^{ll}. Additionally does the high transverse momentum results in a large angular difference between the dilepton and missing transverse momentum vector. The discriminating variable is the transverse mass m_T defined as

$$m_T = \sqrt{(E_T^{ll} + E_T^{miss})^2 - |\vec{p}_T^{\,ll} + \vec{E}_T^{miss}|^2}. \tag{6.1}$$

The kinematic distributions of the discriminating variable are eventually used in the likelihood fit to extract the signal strength. The distributions of m_T for both $N_{jet} = 0$ and $N_{jet} = 1$ after applying the full cut selection can be seen in figure 6.1. Each distribution is again split up in 8 distinct signal regions according to the following cuts. The corresponding fit distributions can be found in appendix C.

Signal Region	m_{ll} [GeV]	$p_T^{l_2}$ [GeV]	l_2 [e/μ]
1	$10 < m_{ll} < 30$	$10 < p_T^{l_2} < 20$	e
2	$10 < m_{ll} < 30$	$10 < p_T^{l_2} < 20$	μ
3	$10 < m_{ll} < 30$	$20 < p_T^{l_2}$	e
4	$10 < m_{ll} < 30$	$20 < p_T^{l_2}$	μ
5	$30 < m_{ll} < 55$	$10 < p_T^{l_2} < 20$	e
6	$30 < m_{ll} < 55$	$10 < p_T^{l_2} < 20$	μ
7	$30 < m_{ll} < 55$	$20 < p_T^{l_2}$	e
8	$30 < m_{ll} < 55$	$20 < p_T^{l_2}$	μ

Table 6.3: Signal regions for both jet categories that are used in the likelihood fit.

6.3.3 Control and Validation

The control(CR) regions are defined to normalize simulated background processes. The normalization factor is extracted from kinematic distributions where the observed events are expected to have negligible signal events and an abundance of background events of a specific process. The normalization factor is then applied in the signal region to normalize the background and improve the MC prediction. There are several methods to extract and apply a normalization factor but the most common one is by performing a likelihood fit to the observed data with the normalization factor as a free parameter. Additional validation regions(VR) can be applied to validate the normalization extracted from the control regions. The control regions are separately defined for $N_{jet} = 0$ and $N_{jet} = 1$ as shown in table 6.4. The corresponding distributions used in the likelihood fit are shown in figures 6.2, 6.3 and 6.4. The cut flow for all the signal and background samples for the signal strength measurement can be found in appendix E.1.

Background	$N_{jet} = 0$:	$N_{jet} = 1$:
$q\bar{q}/gg \to WW \to l\nu l\nu$	$55 < m_{ll} < 110$ GeV $\Delta\phi_{ll} < 2.6$	$m_{ll} > 80$ GeV $\lvert m_{\tau\tau} - m_Z\rvert > 25$ GeV b-jet veto
$Z \to \tau\tau$	$m_{ll} < 80$ GeV $\Delta\phi_{ll} > 2.8$	no $p_T^{miss} > 20$ GeV requirement $m_{ll} < 80$ GeV $m_{\tau\tau} > m_Z - 25$ GeV b-jet veto
$t\bar{t}$ leptonic	no N_{jet} requirement $\Delta\phi_{ll} < 2.8$ GeV $p_T^{ll} > 30$ GeV	$N_{b-jet} = 1$ $m_{\tau\tau} < m_Z - 25$ GeV

TABLE 6.4: Event selection criteria used to define the control regions

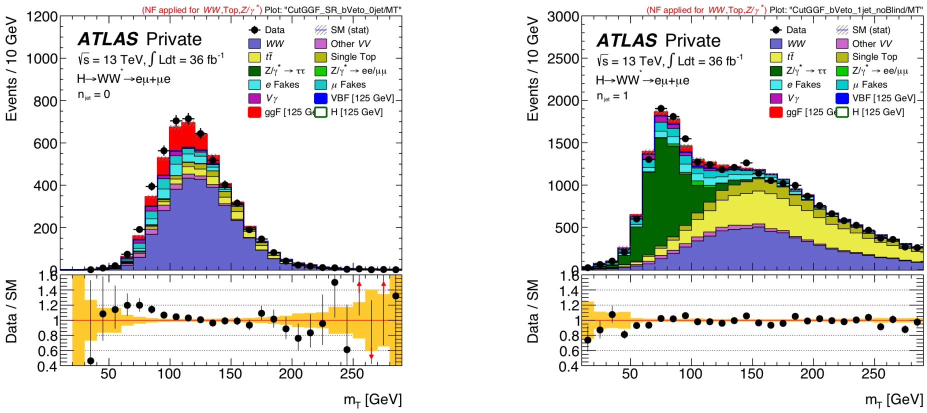

FIGURE 6.1: Distributions of the transverse mass for $N_{jet} = 0$(left) and $N_{jet} = 1$(right) after signal selection criteria are applied (See table 6.2).

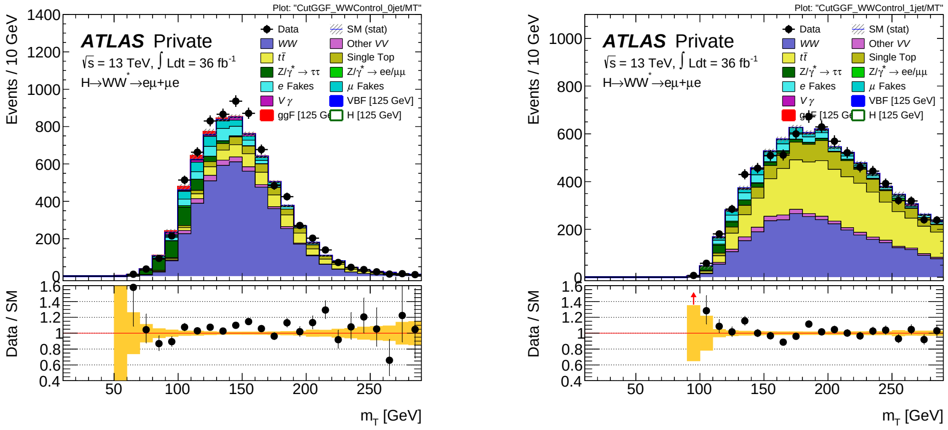

FIGURE 6.2: Distributions of the transverse mass for $N_{jet} = 0$(left) and $N_{jet} = 1$(right) after control selection criteria are applied (See table 6.4) for $q\bar{q}/gg \rightarrow WW \rightarrow l\nu l\nu$ background normalization.

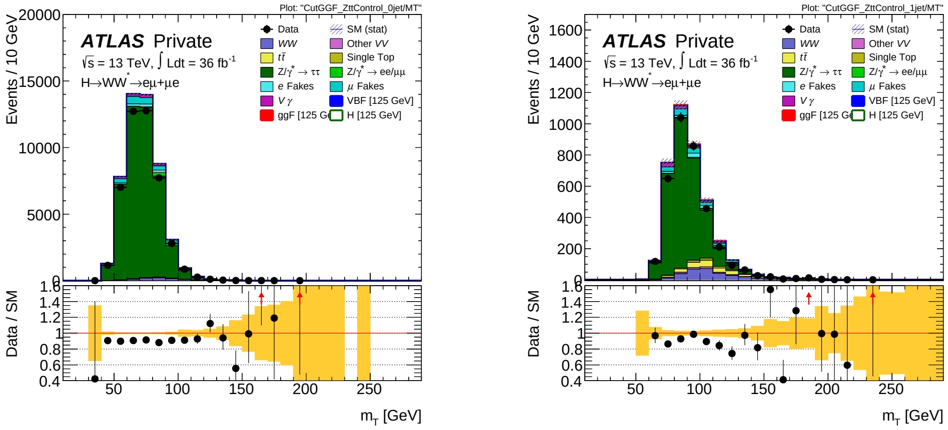

FIGURE 6.3: Distributions of the transverse mass for $N_{jet} = 0$(left) and $N_{jet} = 1$(right) after control selection criteria are applied (See table 6.4) for $Z \rightarrow \tau\tau$ background normalization.

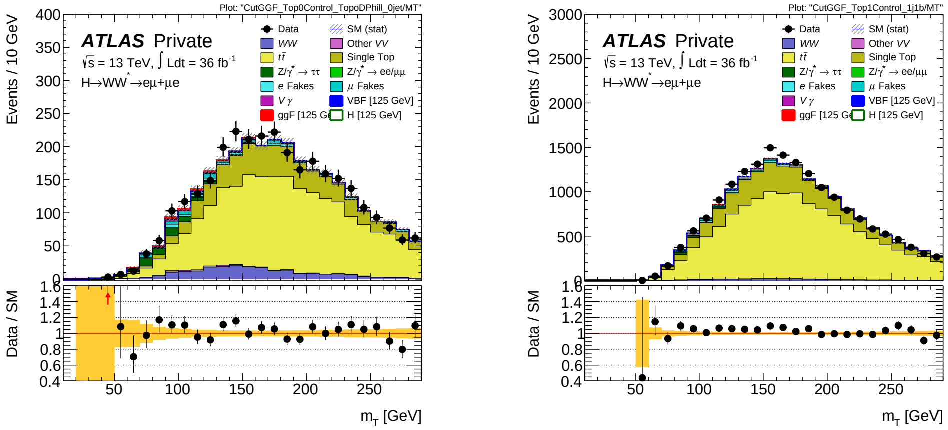

FIGURE 6.4: Distributions of the transverse mass for $N_{jet} = 0$(left) and $N_{jet} = 1$(right) after control selection criteria are applied (See table 6.4) for $t\bar{t}$ leptonic background normalization.

Name	Description	Type
Muon resolution	Track momentum smearing in the Inner Detector and muon spectrometer	P4
Muon scale	Variations in muon momentum scale	P4
Muon identification	Statistical and systematic variation in identification efficiency	SF
Muon isolation	Statistical and systematic variation in isolation efficiency	SF
Muon trigger	Statistical and systematic variation in trigger efficiency	SF
Jet resolution	Track momentum smearing in the Inner Detector	P4
Jet scale	Variations in momentum scale	P4
Jet identification	Statistical and systematic variation in identification efficiency	SF
Jet isolation	Statistical and systematic variation in isolation efficiency	SF
Jet reconstruction	Statistical and systematic variation in reconstruction efficiency	SF
Jet trigger	Statistical and systematic variation in trigger efficiency	SF
Jet resolution nuisance parameter	Single nuisance parameter covering jet energy resolution uncertainties	P4
Jet simulation framework	Uncertainty arising from the use of the ATLFast-II fast simulation framework	P4
Jet scale	Heavy-flavour jet energy scale uncertainty	P4
Jet scale	Linear decomposition of jet energy scale uncertainties	P4
Jet scale	Uncertainties covering η-dependence of the jet energy scale	P4
Jet scale	Uncertainties covering flavour-dependence of the jet energy scale	P4
Jet scale	High p_T jet energy scale uncertainty	P4
Jet scale	Uncertainties covering the effects of pile-up on the jet energy scale	P4
Calorimeter size	Uncertainty covering effects of the calorimeter not covering the whole shower	P4
Jet vertex tagging	Uncertainty on jet vertex tagging	SF
b-tagging	Eigen-vector decomposition of b-tagging uncertainties	SF
c-tagging	Eigen-vector decomposition of c-tagging uncertainties	SF
light flavour-tagging	Eigen-vector decomposition of light-flavour tagging uncertainties	SF
Run extrapolation	Uncertainty covering extrapolation from Run 1 to Run 2	SF
Charm extrapolation	Charm quark specific extrapolation uncertainty	SF
MET resolution	Uncertainty of the missing transverse energy resolution	SF
MET scale	Uncertainty of the missing transverse scale	SF
Lepton fake factor	Uncertainty arising from the subtraction of fake leptons	DD
Lepton fake factor	Uncertainty arising from the sample decomposition variance for the fake leptons	DD
Lepton fake factor	Uncertainty arising from the sample decomposition variance for the fake leptons	DD
Lepton fake factor	Uncertainty arising from the charge dependency of the fake composition for fake leptons	DD
Lepton fake factor	Statistical uncertainty on the fake factor	DD

Table 6.5: Summary of experimental systematic uncertainties used in this analysis

Process	Uncertainty	Description
ggF	Jet veto	Uncertainty associated with the categorization in the number of jets
	Matching	Uncertainty associated with the matching of matrix elements and parton showers
	PS/UE	Uncertainty associated with the modelling of parton showers (PS) and underlying events (UE)
	PDF	Uncertainty associated with the chosen parton distribution function (PDF)
	QCD scale	Uncertainty associated with the choice of renormalization and factorization scales
VBF	PDF	Uncertainty associated with the chosen parton distribution function (PDF)
	QCD scale	Uncertainty associated with the choice of renormalization and factorization scales
WW	Generator	Uncertainty associated with the Monte Carlo generator
	Matching	Uncertainty associated with the matching of matrix elements and parton showers
	PS/UE	Uncertainty associated with the modelling of parton showers (PS) and underlying events (UE)
	PDF	Uncertainty associated with the chosen parton distribution function (PDF)
	QCD scale	Uncertainty associated with the choice of renormalization and factorization scales
	EW correction	Uncertainty associated with the EW corrections used on matrix elements
	CKKW Matching	Uncertainty associated with the CKKW matching of matrix elements and parton showers
WZ/Wγ^*	QCD scales	Uncertainty associated with the choice of renormalization and factorization scales
	Merging scales	Uncertainty associated with the merging scale that is used to cut-off divergencies in matrix element calculations
	CKKW Matching	Uncertainty associated with the CKKW matching of matrix elements and parton showers
	A14 tune	Uncertainty associated with the A14 parameter tune used in the Sherpa generator
Wγ	NLO correction	Uncertainty associated to the next-to-leading order corrections in matrix element calculations
	QCD scale	Uncertainty associated with the choice of renormalization and factorization scales
	Merging scales	Uncertainty associated with the merging scale that is used to cut-off divergencies in matrix element calculations
	PDF	Uncertainty associated with the chosen parton distribution function (PDF)
top	QCD Radiation	Uncertainty associated with parton radiation
	PS/UE	Uncertainty associated with the modelling of parton showers (PS) and underlying events (UE)
	Matching	Uncertainty associated with the matching of matrix elements and parton showers
	Generator	Uncertainty associated with the Monte Carlo generator
	DSDR	Uncertainty associated with the Dislocation Supressing Determinant Ratio gauge actions

Table 6.6: Summary of theoretical systematic uncertainties used in this analysis

6.4 Uncertainty Treatment

Just like with any other measurement, the accuracy of both the signal extraction and coupling modifier measurement is quantified with uncertainty. This uncertainty can originate from several sources but can be globally categorized as either *experimental* or *theoretical*. Lets consider a set of observations x_i, $i = 0, 1, ...N$, a parameter θ to be estimated, also known as a *parameter of interest(POI)*, and a corresponding probability function $p(x_i|\theta)$. These probability distributions can be used to perform a profile likelihood fit to extract the parameter of interest. More information on this process is given in the upcoming section. In general, however, the probability distributions depend on many more additional unknown parameters $\vec{\lambda}$, also known as *nuisance parameters(NPs)*. The value of these parameters can be determined in the same way the parameter of interest θ can be determined. But additionally, one needs to take into account the uncertainties that these NPs bring into the estimation of the POI. These uncertainties are systematic uncertainties.

6.4.1 Experimental Uncertainty

Experimental systematic uncertainties in this analysis are estimated by varying either the four momenta, particle or event weight of an object with $\pm\sigma$ variations and define the variations of the parameter of interest as systematic uncertainty. These types of systematics are known as resp. *four momenta (P4-)* and *scale factor (SF-)systematics*. An additional *Data-driven (DD-)method* is used to take into account the systematic uncertainties related to the fake factor estimation.

6.4.2 Theoretical Uncertainty

The signal and background samples are generated with varying models and Monte Carlo techniques. The theoretical predictions can have both similar as well as process specific systematic uncertainties. A summary of all the theoretical systematic uncertainties is shown in table 6.6.

6.5 Signal Measurement

The measurement of the signal is done with the *profile likelihood method*. Any additional information on this method can be found in references [101, 102].

6.5.1 Maximum-likelihood estimator $\hat{\mu}$

The goal of the signal measurement is to quantify how well the observed data agrees with the observation of a Standard Model Higgs boson. The measurement is made by applying a *profile likelihood fit* on the observed data to extract the signal strength μ for which a value deviating from unity indicates the observation of a Higgs boson with the specified production and decay mode. A likelihood in general states how likely it is to find a certain event in a part of phase space i. e. a bin of a kinematic distributions. Lets assume that a signal sample is used to measure a kinematic variable k for each event. These measurements are used to construct a histogram which after the previously introduced cut analysis has an amount of observed o_i and expected n_i events per bin. The expectation value is defined as

$$n_i = \mu s_i + b_i \tag{6.2}$$

with μ the signal strength that represents a background-only hypothesis for $\mu = 0$ and $\mu = 1$ the signal hypothesis eg. including the Higgs boson. The parameters s_i and b_i are the expected signal and background events and are defined as

$$s_i = s_{tot} \int f(k; \vec{\theta}_s) dk \tag{6.3}$$

$$b_i = b_{tot} \int f(k; \vec{\theta}_b) dk. \tag{6.4}$$

The parameters s_{tot}/b_{tot} are the sums of the expected events over all bins and $f(k; \vec{\theta}_s)/f(k; \vec{\theta}_b)$ the probability distribution functions (PDFs). The PDFs are defined by the underlying theoretical model and are dependant on the kinematic variable k and a set of parameters $\vec{\theta}$ defining this model. The signal strength μ is noted as the parameter of interest and the remaining set $\theta = (\theta_s, \theta_b, b_{tot})$ are noted as *nuisance parameters (NP)*. The parameter s_{tot} remains fixed to the value of the signal model. Because the chance for an event to be found in bin i is Poisson distributed the likelihood function can be defined as a product of these Poisson distributions.

$$L(\mu, \vec{\theta}) = \prod_{i=1}^{N} \frac{(\mu s_i + b_i)^{o_i}}{o_i!} e^{-(\mu s_i + b_i)} \tag{6.5}$$

By maximizing the likelihood function with respect to $\vec{\theta}$ and μ the unconditional maximum-likelihood(ML) estimator $\hat{\mu}$ can be obtained as measurement of the signal strength on the observed data.

6.5.2 Significance

Because the processes studied are quantum mechanical the measurements are probabilistic of nature. An observation might be more likely in one model but can still occur in a different one. To determine the significance of an observed signal strength one needs to quantify what is the probability to observe a signal strength $\hat{\mu}$ under the assumption of no observed signal($\mu = 0$). To quantify this the *profile likelihood ratio* is defined as

$$\lambda(\mu) = \frac{L(\mu, \hat{\hat{\vec{\theta}}})}{L(\hat{\mu}, \hat{\vec{\theta}})}. \tag{6.6}$$

The denominator is the unconditional likelihood function that was maximized to obtain the observed signal strength $\hat{\mu}$. The numerator is the conditional likelihood function maximized with respect to $\vec{\theta}$ for a conditional value of μ. With the profile likelihood ratio a test statistic can be defined as

$$t(\mu) = -2\ln\lambda(\mu). \tag{6.7}$$

The test statistic can be used to quantify the agreement of the observed $\hat{\mu}$ with a hypothesized μ. This can be related to a significance Z that states the exclusion confidence levels in terms of σ.

$$Z(\mu) = \sqrt{-2\ln\lambda(\mu)} \tag{6.8}$$

$$p(\mu) = \int_{t(\hat{\mu})}^{\infty} f(t(\mu))dt \tag{6.9}$$

Here is $f(t(\mu))$ the PDF of the test statistic $t(\mu)$ under the assumption of a signal strength μ which. Under the assumption that the signal strength ML estimator $\hat{\mu}$ follows a Gaussian distribution and given a large data set the PDF of $t(\mu)$ will be a *non-central chi-square* distribution[101]. When assuming $\mu = 0$ one obtains what is called the p_0-value which quantifies the probability to obtain a higher value for the test statistic $\lambda(\mu)$ than the observed $\lambda(\hat{\mu})$. In particle physics a common conventional value for p_0 that justifies a discovery is one that is smaller then $2.87 \cdot 10^{-7}$.

6.5.3 Results

The results are based on data collected from $\sqrt{s} = 13$ TeV pp collisions by the ATLAS experiment and present the measurement of gluon fusion Higgs boson production in the $H \to W^{\pm}W^{\mp *} \to l^{-}\bar{\nu}_l l'^{+}\nu_{l'}$ decay mode. Additionally, a measurement on an Asimov data set was made that represents the expected SM case.

The signal strengths and corresponding significances were measured as

$$\mu_{\text{obs.}} = 1.258^{+0.208}_{-0.200}(tot.) \qquad Z_{\text{obs.}} = 6.6\sigma \tag{6.10}$$

$$\mu_{\text{exp.}} = 1.000^{+0.206}_{-0.197}(tot.) \qquad Z_{\text{exp.}} = 5.3\sigma \tag{6.11}$$

where the total uncertainty given consists of experimental systematic uncertainties, theoretical systematic uncertainties and statistical uncertainties. The measurement agrees with the signal strength measured in reference [1]. The significances state the exclusion confidence level of the background-only hypothesis. The significances correspond to an observed and expected p-value of resp. $p_{0,\text{obs.}} = 1.483 \cdot 10^{-11}$ and $p_{0,\text{exp.}} = 6.586 \cdot 10^{-8}$ which are well below the standard $2.87 \cdot 10^{-7}$ threshold. Additionally a *profile likelihood scan* of the signal strength μ was made with the test statistic defined in equation 6.7 and with corresponding significance exclusion levels.

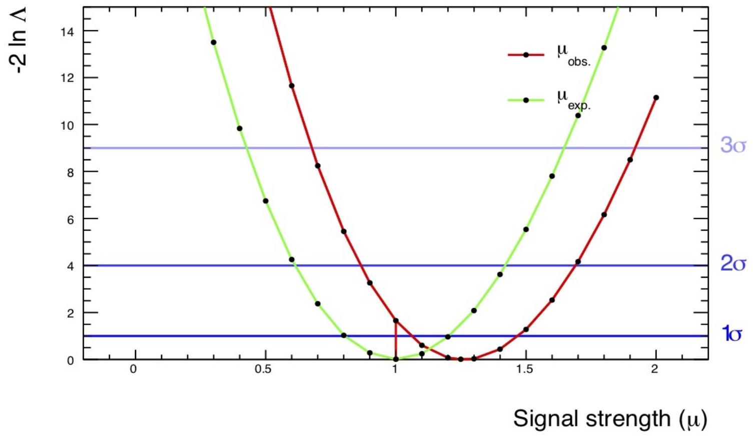

FIGURE 6.5: Scan of the logarithmic difference between a fixed signal strength value(x-axis) and the unconditional likelihood fit value. Shown are the curves corresponding to fits on the observed data (red) and the expected asimov data(green) representing the Standard Model prediction of $\mu = 1$.

Chapter 7

EFT Coupling Analysis

As mentioned in chapter 5, do the measurements of effective coupling parameters not only give a model-independent approach but can also be coupled to BSM predictions and model shape differences in addition to the total signal rate. The goal of this chapter is to present a precise measurement on the coupling parameters κ_{HWW} and κ_{AWW} as introduced in section 2.6.2 in the gluon fusion $H \to W^{\pm}W^{\mp *} \to l^{-}\bar{\nu}_{l}l'^{+}\nu_{l'}$ channel. The selected decay topology and applied cuts are the same as introduced in sections 6.2 and 6.3. The coupling parameters are measured with a *profile likelihood fit* with an Effective Lagrangian Morphing implementation.

7.1 Modeling at the LHC

In the Chapter 3 and 4 it is shown that the creation of fully reconstructed Monte Carlo samples is a long and precise process that takes up a major part of the LHC computing grid resources. The development of new techniques are therefore always needed. For example, the measurement of the signal strength as presented in the previous chapter requires the generation, simulation and reconstruction of dedicated Monte Carlo samples with specific parameter settings. By evaluating the likelihood for different values for the signal strength the likelihood can be minimized and the most likely value with respect to the data can be measured. However, in case of physics parameters that function as input at the beginning of the sample creation process, eg. coupling parameters such as κ_{HWW} and κ_{AWW}, a likelihood fit would quickly become unfeasible as a new sample production chain must be initiated for each parameter space point at which the likelihood is evaluated. In this section some of the most common techniques are introduced that try to circumvent these computational efforts but still accurately model the underlying physics.

7.1.1 Matrix Element Reweighting

When Monte Carlo samples are generated the size is determined by requesting a certain number of events while the cross section is kept fixed relative to the calculated matrix element. However, in section 2.5 it is shown that the number of events depends on the cross section and total integrated luminosity. Because observed data is taken at a known luminosity the Monte Carlo events are weighted to correspond this luminosity.

If any parameters that determine the matrix element are changed the change in matrix element would correspond to a change in the event weights. If the matrix elements of the initial and target samples are calculated the weights can be defined as

$$w_t = w_i \cdot \frac{|\mathcal{M}_t|^2}{|\mathcal{M}_i|^2}, \tag{7.1}$$

with the initial matrix element $\mathcal{M}_i$, the matrix element with the target parameter set $\mathcal{M}_t$ and the initial event weights w_i. This can be applied at any stage of the Monte Carlo sample creation and can therefore *reweight* the events of the initial fully simulated and reconstructed sample to avoid some computational heavy modeling steps. However, these event weights can become very large for new parameter sets that differ a lot from the initial one. If these events are located in kinematic distribution areas with a low number of events the statistical power can be reduced significantly. Additionally, it can be difficult to take into account the statistical dependency of samples created from the same initial sample and the method is not fast enough to be used in between minimization steps in case of a profile likelihood fit.

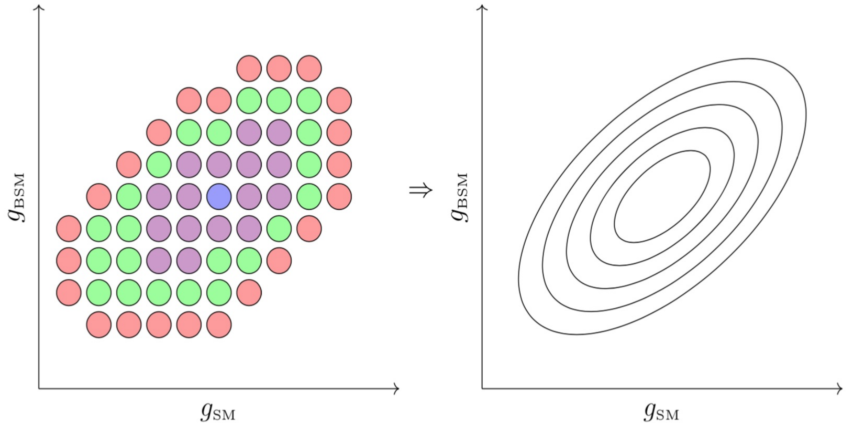

FIGURE 7.1: A likelihood function for two parameters of interest g_{SM} and g_{BSM}. The likelihood can be minimized by evaluating it for a discrete set of samples (left) or with a continuous likelihood function based on a discrete set of samples (right). [18].

7.1.2 Vertical Morphing

Another alternative would be to interpolate between an initial set of generated Monte Carlo samples to a new point in parameter space in between likelihood minimization steps. This procedure is called *morphing* and one variety is vertical morphing [19]. Lets assume a set of n samples that depend on a parameter m and result in a corresponding PDF $f(x|m_i)$ for some observable x. The Taylor expansion around a certain reference value m_0 for this function reads,

$$f(x|m_i) \approx \sum_{j=0}^{n-1} (m_i - m_0)^j \frac{1}{j!} \frac{d^{(j)}}{dm^{(j)}} f(m_0) \tag{7.2}$$

By redefining in matrix notation

$$M_{ij} = (m_i - m_0)^j \tag{7.3}$$

and

$$f'_j(x|m_0) = \frac{1}{j!} \frac{d^{(j)}}{dm^{(j)}} f(m_0) \tag{7.4}$$

gives the new definition

$$f'_j(x|m_0) \approx M_{ij}^{-1} f(x|m_i). \tag{7.5}$$

The new PDF to an arbitrary parameter m' is then given as

$$p(x|m') = \sum_{i,j=0}^{n-1} (m' - m_0)^j m_{ij}^{-1} f(x|m_i). \tag{7.6}$$

However, when the mean of the initial PDFs differ to much the vertical morphing can give an inaccurate result. An example is given in figure 7.2. Vertical morphing is still suitable for eg. the interpolating between probability distribution functions for different nuisance parameters. The vertical morphing can accurately model the shape and rate variations to measure the impact of systematic uncertainties.

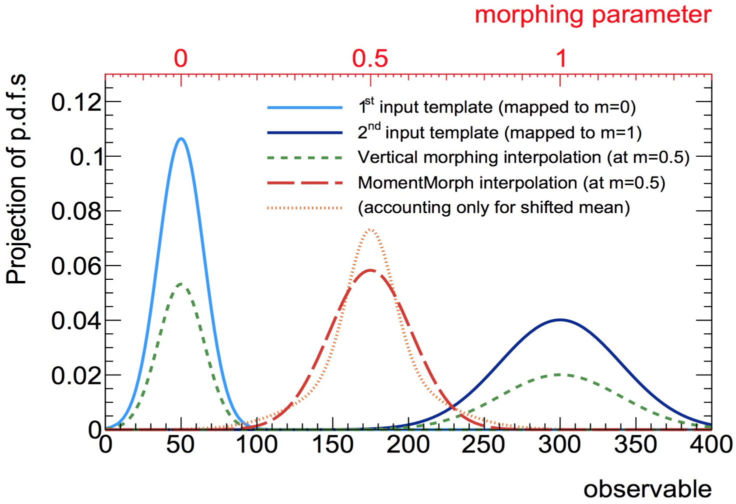

FIGURE 7.2: An example of morphing between two samples of which the PDF is a normal distribution. The statistical moments change for different values for some parameter m. The morphing result is given for both the vertical and the moment morphing [19].

7.1.3 Moment Morphing

To take the differences of the mean and standard deviation into account, also known as *statistical moments*, an additional coordinate transformation can be made[19]. The mean and standard deviation for a target PDF are resp. defined as

$$\nu(m') = \sum_{i,j=0}^{n-1} (m' - m_0)^j M_{ij}^{-1} \mu(m_i) \tag{7.7}$$

$$\eta(m') = \sum_{i,j=0}^{n-1} (m' - m_0)^j M_{ij}^{-1} \sigma(m_i) \tag{7.8}$$

where $\mu(m_i$ and $\sigma(m_i)$ are resp. the mean and and standard deviation of the PDFs of the initial samples. With these a coordinate transformation can be made defined as,

$$\xi_i(x|m') = \frac{x - \nu(m')}{\eta(m')} \cdot \sigma(m_i) + \mu(m_i) \tag{7.9}$$

Using this coordinate transformation the new morphing result for a PDF at an arbitrary parameter m' is redefined as,

$$h(x|m') = \sum_{i,j=0}^{n-1} (m' - m_0)^j M_{ij} f(\xi_i(x|m')|m_i). \tag{7.10}$$

In figure 7.2 it is shown that the moment morphing results in a more satisfactory output than the vertical morphing. The additional advantages are that moment morphing can be used for both binned and continuous templates, is not restricted to the number of model parameter, input observables or input templates and can also morph horizontally. Moment morphing is also widely used in analyses to take systematic uncertainties into account.

However, both morphing techniques are empirical and agnostic of the underlying physics. This means that both techniques can not model any effects of the QFT that lies at the hart of a PDF such as interference or cancellation effects. A technique that does take into account these effects and is much faster than matrix element reweighting is *Effective Lagrangian Morphing*.

7.2 Effective Lagrangian Morphing

In the previous section some of the most well-known interpolation techniques are presented. Effective Lagrangian Morphing is a technique that can interpolate between a discrete set of fully simulated signal samples that are described by an Effective Field Theory as introduced in section 2.6. In section 2.6.3 a theoretical description is given how such an interpolation can be used to calculate the cross section at an arbitrary point in coupling parameter space. Here a more practical description is given for the interpolation between histograms. The interpolation technique only requires kinematic distributions and parameters of the initial samples as input and results in kinematic distributions that represent the arbitrary point in coupling parameter space. The morphing is fast enough such that the output distributions can be used to form a new likelihood function in between minimization steps of a profile likelihood fit.

Lets assume some kinematic distribution T that depends on an arbitrary set of non-SM Higgs boson couplings to which one wants morph to. Effective Lagrangian Morphing defines a morphing function as

$$T_{out}(\vec{g}_t) = \sum_i w_i(\vec{g}_t; \vec{g}_i) T_i(\vec{g}_i) \tag{7.11}$$

with the target couplings $\vec{g}_t$, parameters of the input samples $\vec{g}_i$, the distributions of the input samples $T_i(\vec{g}_i)$ and weights $w_i(\vec{g}_t; \vec{g}_i)$. The calculation of the weights can be illustrated with a simple example.

7.2.1 A Simple Showcase

Let us consider a 2 → 2 s-channel Higgs process with a single non-SM Higgs boson coupling g_{BSM} in the vertex in addition to one SM Higgs boson coupling g_{SM}. As introduced in section 2.6.3 can the matrix element of such a EFT scenario be described by the sum

$$\mathcal{M}(g_{SM}, g_{BSM}) = g_{SM} \cdot \mathcal{O}_{SM} + g_{BSM} \cdot \mathcal{O}_{BSM}. \tag{7.12}$$

Under the assumption that an observable T is proportional to $|\mathcal{M}|^2$ one can state

$$T(g_{SM}, g_{BSM}) \propto g_{SM}^2 \cdot \mathcal{O}_{SM}^2 + g_{BSM}^2 \cdot \mathcal{O}_{BSM}^2 + 2 g_{SM} \cdot g_{BSM} \cdot \Re(\mathcal{O}_{SM}^* \mathcal{O}_{BSM}) \tag{7.13}$$

Now in general the couplings g_{SM} and g_{BSM} can have any value. For educational purposes a pure SM $\vec{g}_{in,1} = (1,0)$, a pure BSM $\vec{g}_{in,2} = (0,1)$ and a mixed $\vec{g}_{in,3} = (1,1)$ sample with resp. input distributions $T_{in}(1,0)$, $T_{in}(0,1)$ and $T_{in}(1,1)$ are chosen. This gives the following proportionalities.

$$T_{in}(1,0) \propto |\mathcal{O}_{SM}|^2 \tag{7.14}$$

$$T_{in}(0,1) \propto |\mathcal{O}_{BSM}|^2 \tag{7.15}$$

$$T_{in}(1,0) \propto |\mathcal{O}_{SM}|^2 + |\mathcal{O}_{BSM}|^2 + 2\Re(\mathcal{O}_{SM}^* \mathcal{O}_{BSM}) \tag{7.16}$$

This results in the morphing function

$$\begin{aligned} T_{out}(g_{SM}, g_{BSM}) = & \underbrace{(g_{SM}^2 - g_{SM} g_{BSM})}_{w_1} T_{in}(1,0) \\ & + \underbrace{(g_{BSM}^2 - g_{SM} g_{BSM})}_{w_2} T_{in}(0,1) \\ & + \underbrace{g_{SM} g_{BSM}}_{w_3} T_{in}(1,1). \end{aligned} \tag{7.17}$$

Here it is shown how the earlier introduced weights w_i are only dependant on the target coupling parameters. A graphic depiction is given in figure 7.3 that illustrates the derivation and how it takes interference effects into account. To generalize this to initial samples with arbitrary values for their coupling parameters one can make the following ansatz

$$\begin{aligned}T_{out}(g_{SM}, g_{BSM}) =&(a_{11}g_{SM}^2 + a_{12}g_{BSM}^2 + a_{13}g_{SM}g_{BSM})T_{in}(g_{SM,1}, g_{BSM,1})\\ &(a_{21}g_{SM}^2 + a_{22}g_{BSM}^2 + a_{23}g_{SM}g_{BSM})T_{in}(g_{SM,2}, g_{BSM,2})\\ &(a_{13}g_{SM}^2 + a_{32}g_{BSM}^2 + a_{33}g_{SM}g_{BSM})T_{in}(g_{SM,3}, g_{BSM,3})\end{aligned} \tag{7.18}$$

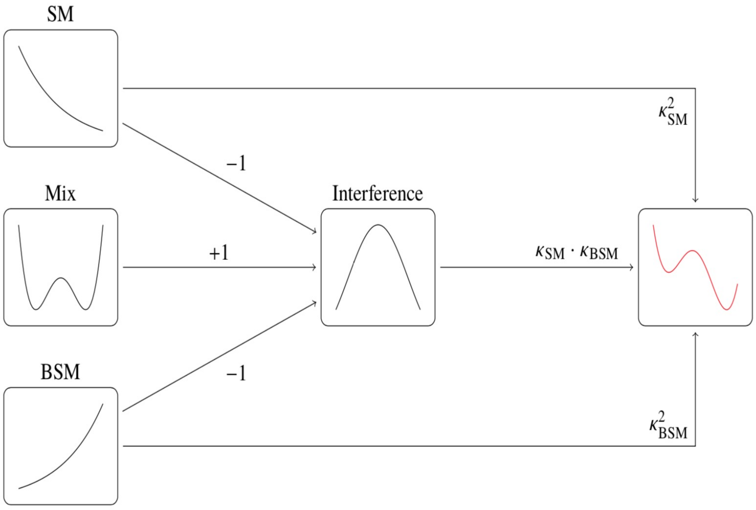

FIGURE 7.3: A graphical depiction of Effective Lagrangian Morphing in a simple showcase [20].

The morphing function requires that when morphing to an input parameter set the output distribution should be equal to the input distribution. This results in the constraints

$$T_{out} = T_{in} \tag{7.19}$$

$$\vec{g}_t = \vec{g}_i \tag{7.20}$$

and thus a set of linear equations in matrix form.

$$\begin{pmatrix} a_{11} & a_{12} & a_{13} \\ a_{21} & a_{22} & a_{23} \\ a_{31} & a_{32} & a_{33} \end{pmatrix} \cdot \begin{pmatrix} g_{SM,1}^2 & g_{SM,2}^2 & g_{SM_3}^2 \\ g_{BSM,1}^2 & g_{BSM,2}^2 & g_{BSM,3}^2 \\ g_{SM,1}g_{BSM,1} & g_{SM,2}g_{BSM,2} & g_{SM,3}g_{BSM_3} \end{pmatrix} = A \cdot G = \mathbb{1} \tag{7.21}$$

This gives an unique solution if the input parameters fulfill the condition $det(G) \neq 0$. A generalization to more coupling parameters is straightforward and can be found in reference [20].

7.3 Experimental Strategy

The Effective Lagrangian Morphing technique is implemented within the `RooFit` package[103]. To use the morphing implementation to measure the coupling parameters κ_{HWW} and κ_{AWW} the following experimental strategy is set.

1. Choose the number of input samples, also known as *base samples*, and their coupling parameter configuration.
2. Choose addition validation samples that will be used to morph to and validate the morphing technique.
3. Fully simulate and reconstruct the base and validation samples.
4. Choose the kinematic distribution that will be used in the morphing.
5. Apply kinematic cuts to increase the signal to background ratio in this kinematic distribution.
6. Optimize the coupling parameter configuration of the base samples with a dedicated algorithm.
7. Use the optimized base samples to morph to the validation samples and compare the kinematic distributions to determine any discrepancies.
8. Build a `RooFit` workspace with the morphing implementation and use the workspace to measure the coupling modifier parameters κ_{HWW} and κ_{AWW} with a profile likelihood fit.

7.4 Base and Validation Samples

As illustrated in section 7.2 is the number of base samples determined by the couplings that play part in the process under study. In case of a $2 \rightarrow 2$ s-channel process at leading order with n_p couplings exclusively in the production vertex, n_d couplings exclusively in the decay vertex and n_s shared couplings, the number of samples needed to form a basis for Effective Lagrangian Morphing is

$$\begin{aligned} N =& \frac{n_p(n_p+1)}{2} \cdot \frac{n_d(n_d+1)}{2} + \binom{4+n_s-1}{4} \\ &+ \left(n_p \cdot n_s + \frac{n_s(n_s+1)}{2}\right) \cdot \left(\frac{n_d(n_d+1)}{2}\right) \\ &+ \left(n_d \cdot n_s + \frac{n_s(n_s+1)}{2}\right) \cdot \left(\frac{n_p(n_p+1)}{2}\right) \\ &\frac{n_s(n_s+1)}{2} \cdot n_p \cdot n_d + (n_p+n_d)\left(\binom{3+n_s-1}{3}\right). \end{aligned} \tag{7.22}$$

In the section 2.6.2 the coupling parameters are introduced as scale factors to the SM Higgs couplings. The SM couplings are constant so that the role of BSM couplings in Effective Lagrangian Morphing is replaced with the coupling parameters. The morphing concepts remain the same. The gluon fusion production vertex can contribute the coupling parameters κ_{Hgg} and κ_{Agg} through the top quark loop. However, in this analysis we assume a CP-even SM Higgs to gluon coupling i. e. we only include the κ_{Hgg} coefficient in the production vertex ($n_p = 1$). The decay vertex $H \to WW$ contributes the two BSM coefficients κ_{HWW} and κ_{AWW} and the SM coefficient κ_{SM} ($n_d = 3$). There are no share coefficient that contribute to the process. The rest of the coefficients in the Higgs Characterization Model (see section 2.6.2) do not contribute and are set to zero throughout the analysis. With equation 7.4 it can be shown that this results in $N = 6$ base samples. The number of validation samples is trivial for the morphing process itself and only plays a role in the optimization and validation of the base samples.

Samples	κ_{HWW}	κ_{AWW}
Input Sample 1 ”EFT_1”	-4.07	-4.13
Input Sample 2 ”EFT_2”	-4.03	4.11
Input Sample 3 ”EFT_3”	1.53	-7.24
Input Sample 4 ”EFT_4”	5.41	-0.07
Input Sample 5 ”EFT_5”	-0.12	0.13
Input Sample 6 ”EFT_6”	1.66	7.37
Validation Sample 1	-2.47	-0.13
Validation Sample 2	-0.03	-3.89
Validation Sample 3	3.15	-2.42
Validation Sample 4	3.19	2.37
Validation Sample 5	2.42	-0.24
Validation Sample 6	-4.11	0.09
Validation Sample 7	4.32	-3.92
Validation Sample 8	4.22	4.64

TABLE 7.1: Values of the coupling parameters for the base and validation samples

In the parameter configurations of both the base and validation samples the values $\kappa_{SM} = \sqrt{2}$, $\kappa_{Hgg} = \sqrt{2}$ and $\cos\alpha = 1/\sqrt{2}$ are kept constant. The values for coefficients κ_{HWW} and κ_{AWW} are given in 7.1 and chosen to evenly span the range $[-8, 8]$. Based on earlier investigations [18, 20, 89] this is the expected region of interest, i. e. the region in which the coefficient measurement will lie. Additionally, a simple algorithm is used before sample generation to check if the coefficients satisfy the constraint $\det(G) \neq 0$ and can be used to construct a morphing function. The validation points are chosen randomly in between the base samples.

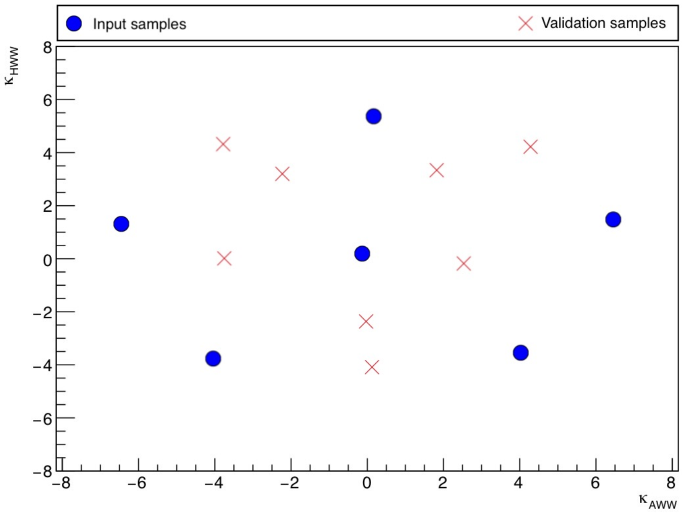

FIGURE 7.4: Parameter configuration overview of the initial base and validation samples.

Just like with the signal strength extraction is the discriminating variable the transverse mass m_T because of the expected peak in the kinematic distribution. Also the same kinematic cuts are applied to both the base and validation sample as the signal samples in the signal strength analysis. The cut flow for all the signal and background samples for the EFT coupling measurement can be found in appendix E.2.

7.5 Base Sample Optimization

To optimize the base sample parameter configuration is to find one that gives the best morphing result, i. e. generates kinematic distributions that have minimal uncertainties. Because we do not know a priori which steps the likelihood minimization will take through parameter space we can optimize the base samples with respect validation samples chosen in the expected region of measurement.

To optimize the base sample a *figure of merit* needs to choosen that quantifies the morphing performance of a set of base samples. In general this figure of merit for N base samples can be chosen to be

$$f(\vec{g}_1, ..., \vec{g}_N) = \sum_{v \in \mathcal{V}} \sqrt{\Delta\sigma^2(\vec{g}_v | \vec{g}_1, ..., \vec{g}_N)} \tag{7.23}$$

where the sum runs over the uncertainty of the morphing result at the validation parameter points $\vec{g}_v$ from N base samples with parameters $\vec{g}_i$. The uncertainty is defined as

$$\Delta\sigma(\vec{g}_v | \vec{g}_1, ..., \vec{g}_N) = \sqrt{\sum_{i=1}^{N} w_i^2 \sigma_i^2(\vec{g}_i \cdot (\Delta\sigma_i)^2} \tag{7.24}$$

with w_i the weights introduced in section 7.2, $\sigma_i(\vec{g}_i)$ the cross section of the base sample and $\Delta\sigma_i^2$ the relative uncertainty of the base samples [17]. However, one needs to take into account that the validation parameter points are difficult to model for the used Monte Carlo generator or implemented model which results in large uncertainties not associated with the morphing. By normalizing to the validation uncertainties the figure of merit becomes

$$f(\vec{g}_1, ..., \vec{g}_N) = \sum_{v \in \mathcal{V}} \sqrt{\frac{\Delta\sigma^2(\vec{g}_v | \vec{g}_1, ..., \vec{g}_N)}{\Delta\sigma_v^2} \cdot (\sigma(\vec{g}_v | \vec{g}_1, ..., \vec{g}_N) - \sigma_v)^2}. \tag{7.25}$$

A dedicated algorithm is applied that morphs to a test basis and consecutively uses this test basis to morph to the validation samples and calculate the uncertainty. The algorithm repeats this process until uncertainty converges. Repeating the minimization with the optimized samples can improve the base samples even further.

The optimization algorithm has been repeated for three iterations i. e. after each convergence the new base parameter configuration is used to create new fully simulated and reconstructed signal samples to repeat the optimization. To map the impact of the optimization algorithm the resulting base sample is used after each optimization to morph to a range of parameter points to compare the result and uncertainty. The optimized samples are used to morph over a range of $[-8, 8]$ with steps of 0.1 for the coefficients κ_{AWW} and κ_{HWW}. For each resulting histogram the cross section and rel. uncertainty is calculated and plotted in figures 7.5,7.6,7.7 and 7.8. An overview of the optimization impact is given in table 7.2.

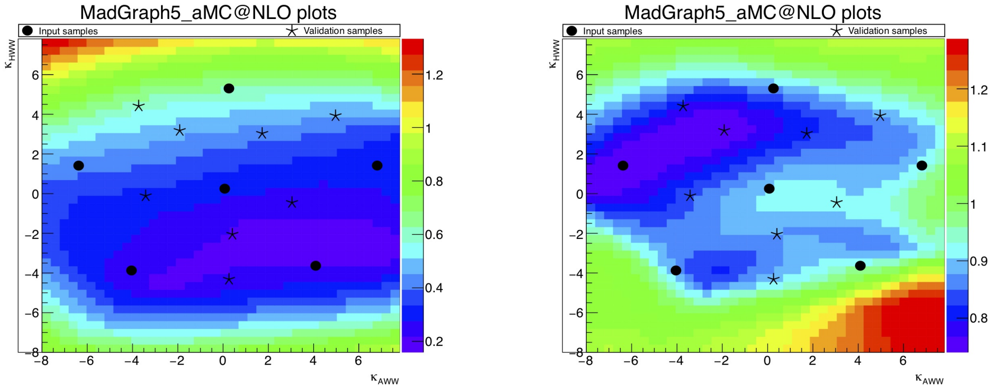

FIGURE 7.5: Morphing result and relative uncertainty before optimization

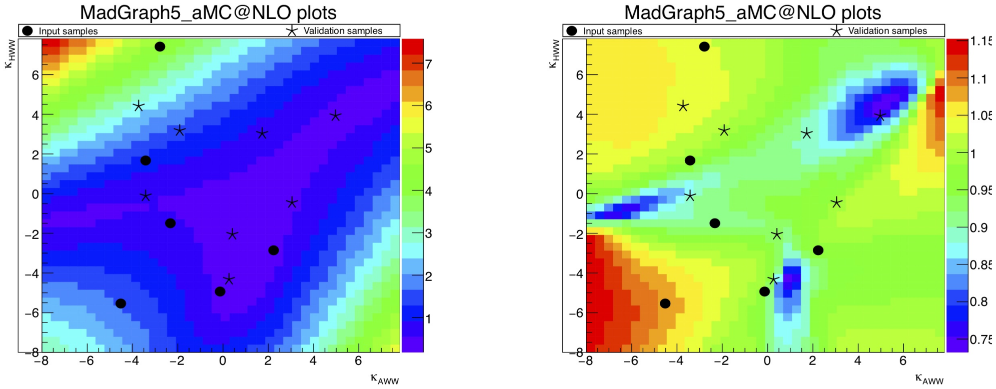

FIGURE 7.6: Morphing result and relative uncertainty after one optimization

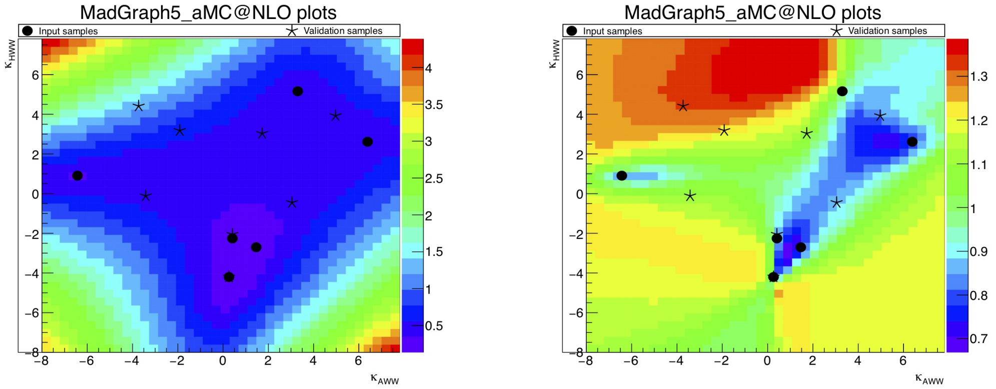

FIGURE 7.7: Morphing result and relative uncertainty after two optimizations

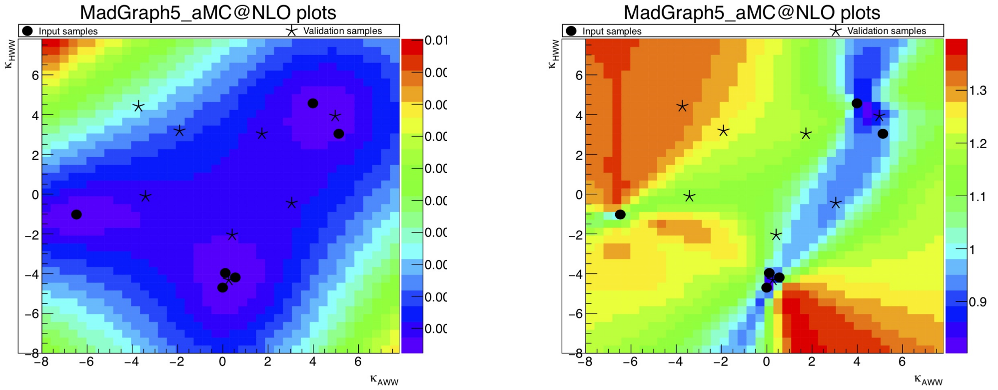

FIGURE 7.8: Morphing result and relative uncertainty after three optimizations

Optimization	min. rel. uncert.	av. rel. uncert.
0	0.740194	0.948051
1	0.727934	0.982931
2	0.658247	1.124754
3	0.731085	1.185848

TABLE 7.2: The impact of the optimization on the relative uncertainty in terms of the average and the lowest of the whole parameter range.

The optimization shows no clear overall improvement in terms of minimal and average relative uncertainty. This can be explained by the low Monte Carlo signal statistics in the signal region histograms that are used as input for the Effective Lagrangian Morphing. The chosen signal region for optimization was signal region 1 as defined in table 6.3. However, each of the signal regions has a total raw event count in the order of a few tens of events that are distributed over 50 bins. This results in a low to sometimes even empty bin count which might result in an unrepresentative distribution shape i. e. a shape that does not model the underlying physics well. This also means that the signal samples are optimized to validation histograms that might have the same issue. In the appendix D some signal region histograms are shown that contain the morphing result and the validation histogram.

7.6 Results

The results are based on data collected from $\sqrt{s} = 13$ TeV pp collisions by the ATLAS experiment and present the measurement of the coupling modifiers κ_{HWW} and κ_{AWW} as introduced in section 2.6.2 in the gluon fusion $H \to W^{\pm}W^{\mp *} \to l^{-}\bar{\nu}_{l}l'^{+}\nu_{l'}$ channel. Additionally, a measurement on an Asimov data set was made that represents the expected SM case of $\kappa_{HWW} = 0$ and $\kappa_{AWW} = 0$.

A *profile likelihood fit* is performed to obtain the maximum likelihood estimator for both coupling parameters of which the results are shown in table **??**. The two-dimensional likelihood scan probes both coupling parameters in the range $[-6, 6]$ with a step size of 0.48. The results are plotted in both a surface plot as well as a contour plot in figures 7.9, 7.10, 7.11 and 7.12. Additionally, a one-dimensional likelihood scan is performed for each coupling parameter in the range $[-6, 6]$ with a step size of 0.24. The results are plotted in figures 7.13 and 7.14.

Coupling parameter	Observed	Expected
κ_{AWW}	2.80481	-0.0627708
κ_{HWW}	-4.46414	0.144603

Table 7.3: Maximum likelihood estimators of the two-dimensional likelihood scans for the coupling parameters κ_{AWW} and κ_{HWW} for both observed and Asimov data.

For some coupling parameter values in the likelihood scans an abnormally large value for the logarithmic likelihood ratio was obtained due to a non-convergent minimization. These artifacts were removed and replaced with a value obtained from a nearest-neighbour linear interpolation.

When the results are compared to the coupling parameter measurement results in figure 5.5 and 5.7 some similarities can be identified. The one-dimensional likelihood scan of κ_{HWW} in figure 7.14 and κ_{HVV} in figure 5.5 both show an asymmetry in the observed data while keeping a symmetry in the Asimov data. However, the symmetry in the one-dimensional likelihood scan of κ_{AWW} in figure 7.13 does not show in figure 5.5. The expected two-dimensional fit in figure 5.7 with the κ_{SM} as fixed parameter and figure **??** show a similar sensitivity. The observed two-dimensional fit in figure 5.7 with the κ_{SM} as fixed parameter and figure 7.10 both have a double minimum structure though the minima of the latter are located at different parameter values and have differing values for the negative log-likelihood.

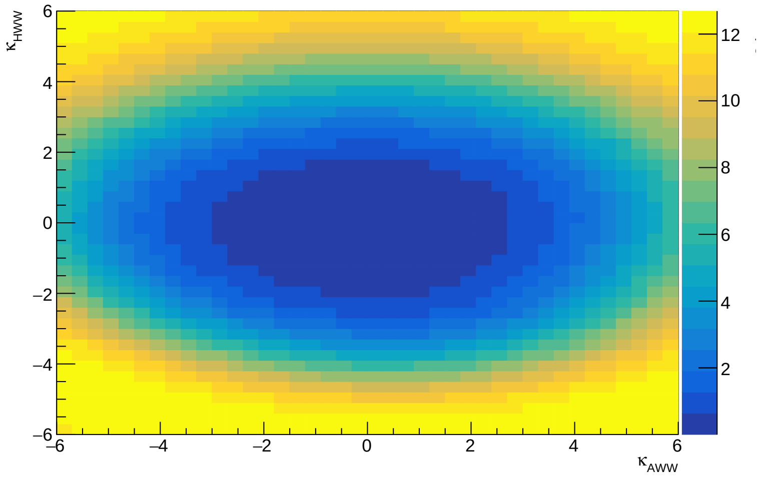

FIGURE 7.9: Contour plot of the expected SM two-dimensional negative log-likelihood scan for the κ_{HWW} and κ_{AWW} coupling parameters.

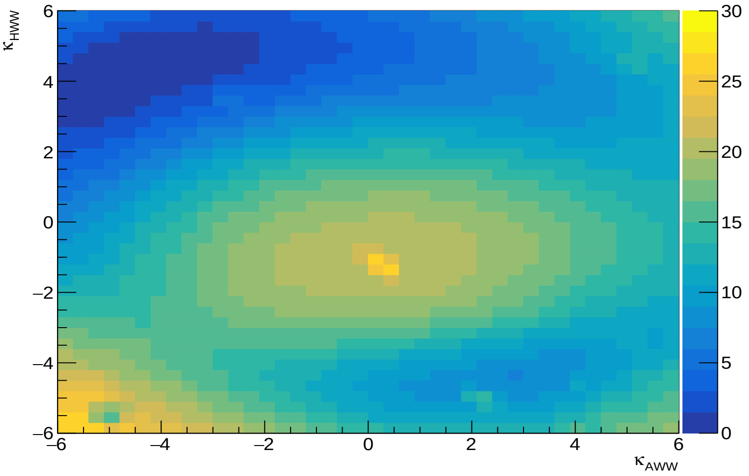

FIGURE 7.10: Contour plot of the observed two-dimensional negative log-likelihood scan for the κ_{HWW} and κ_{AWW} coupling parameters.

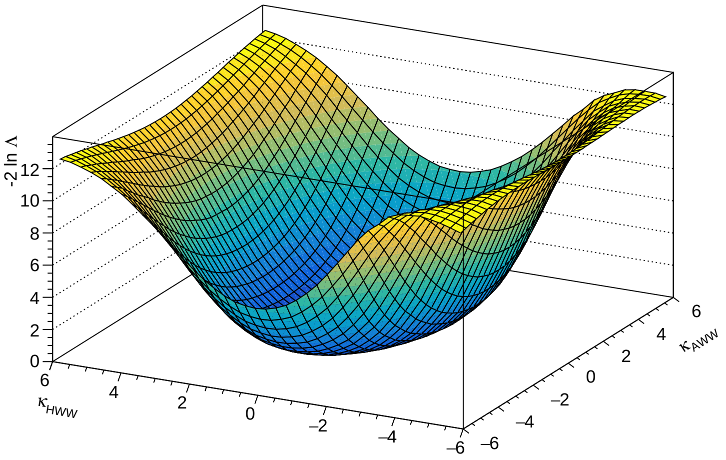

FIGURE 7.11: Surface plot of the expected SM two-dimensional negative log-likelihood scan for the κ_{HWW} and κ_{AWW} coupling parameters.

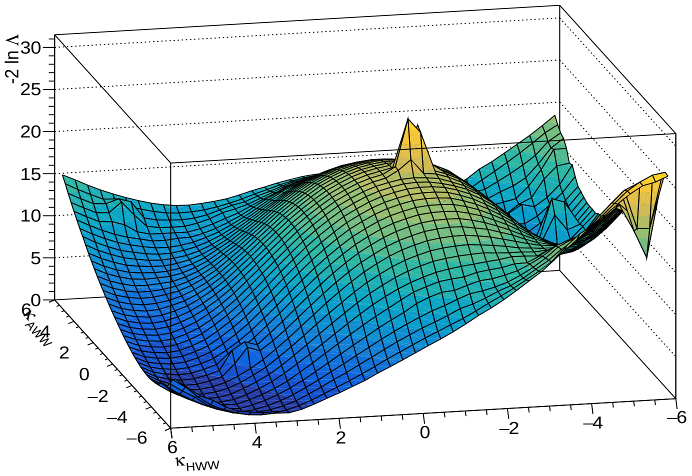

FIGURE 7.12: Surface plot of the observed two-dimensional negative log-likelihood scan for the κ_{HWW} and κ_{AWW} coupling parameters.

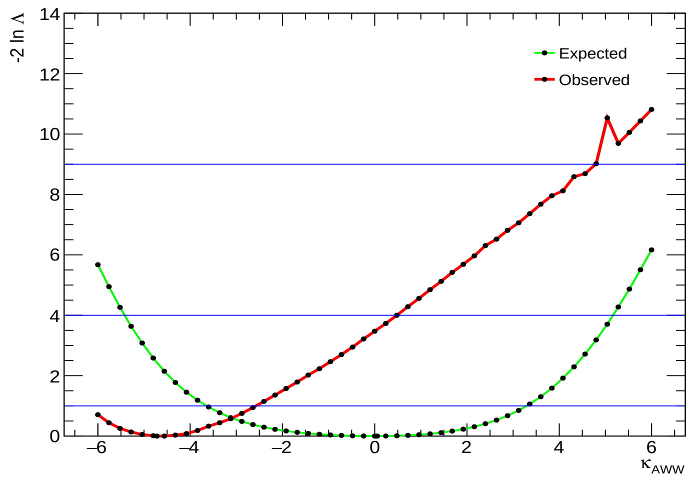

FIGURE 7.13: Observed (red) and expected SM (green) one-dimensional negative log-likelihood scan for the κ_{AWW} coupling parameter.

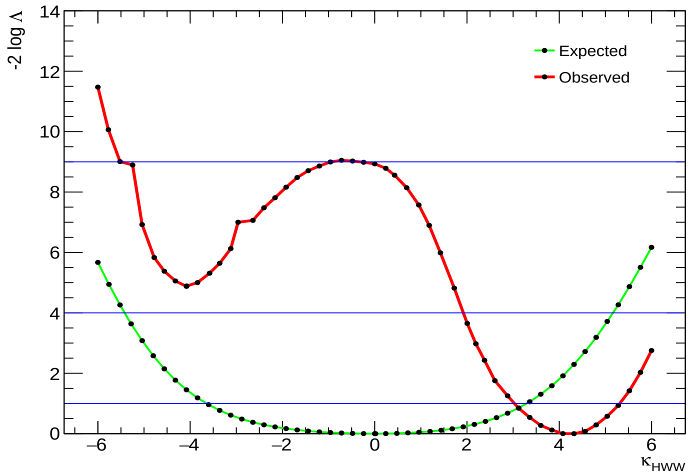

FIGURE 7.14: Observed (red) and expected SM (green) one-dimensional negative log-likelihood scan for the κ_{HWW} coupling parameter.

Chapter 8

Conclusions and Outlook

This thesis presents the measurement of the Higgs boson and the effective field theory coupling parameters κ_{HWW} and κ_{AWW}. The measurements are performed on data from pp collisions at $\sqrt{s} = 13$ TeV taken during 2015 and 2016 runs by the ATLAS detector corresponding to a total integrated luminosity of 36.07 fb^{-1}.

8.1 Signal Strength Analysis

Chapter 6 presents the analysis of data with the goal to identify Higgs bosons via gluon fusion production and $H \to W^{\pm}W^{\mp *} \to l^{-}\bar{\nu}_{l}l'^{+}\nu_{l'}$ decay mode. The signal strength extracted with a profile likelihood method and was measured as

$$\mu = 1.253^{+0.219}_{-0.197}(tot.) \tag{8.1}$$

with an observed significance of $p_0 = 1.446 \cdot 10^{-11}$ corresponding to 6.7 standard deviations. The observed signal strength is in good agreement with the Standard Model prediction of $\mu = 1$.

8.2 EFT Coupling Analysis

Chapter 7 presents the analysis of data with the goal to measure the CP-even κ_{HWW} and CP-odd κ_{AWW} coupling parameters via gluon fusion production and $H \to W^{\pm}W^{\mp *} \to l^{-}\bar{\nu}_{l}l'^{+}\nu_{l'}$ decay mode. The coupling parameters are extracted with a profile likelihood method with an Effective Lagrangian Morphing technique implementation. The measurement is still in agreement with previous studies and the Standard Model prediction.

The analysis shows that a precision measurement is possible with the use of an Effective Lagrangian Morphing technique and gives an indication of the precision of such a measurement. However, the main take-away message is the proof of concept as the analysis still shows a lot of room for improvement. The first and most straightforward improvement would be the increase of simulated signal sample events. The signal samples could provide additional improvement if the generation accuracy of the samples would be upgraded to NLO level. Furthermore, the applied kinematic cuts are optimized for the isolation of signal from background events. The measurement would however benefit from an altered cut analysis that also takes the separation power of the EFT configuration into account. Lastly, the measurement of the effective coupling parameters show a large deviation from the Standard Model prediction which is acceptable with the current sensitivity. However, future studies would profit greatly from a breakdown study of the statistical and systematic uncertainties that impact the measurement.

Appendix A

Theoretical Derivations

A.1 Free Scalar Field Generating Functional

The starting expression is the generating functional with the free scalar field Lagrangian plugged in.

$$Z[J] = \frac{1}{Z_0}\int \mathcal{D}\phi e^{i/\hbar \int d^4x(\frac{1}{2}\partial_\mu\phi\partial^\mu\phi - \frac{1}{2}m^2\phi^2 + J(x)\phi)} \tag{A.1}$$

It is possible to integrate the term $\partial_\mu\phi\partial^\mu\phi$ by parts and using Gauss' theorem the functional gives

$$Z[J] = \frac{1}{Z_0}\int \mathcal{D}\phi e^{-i/\hbar \int d^4x(\frac{1}{2}\phi(\Box + m^2)\phi - J(x)\phi)}. \tag{A.2}$$

It is possible to make the following change in variables.

$$\phi(x) \to \phi(x) + \phi_0(x) \tag{A.3}$$

Including

$$\int d^4x\phi\Box\phi_0 = \int d^4x\phi_0\Box\phi \tag{A.4}$$

and demanding that $\phi_0 \to 0$ at infinity this change in variables gives the functional

$$Z[J] = \frac{1}{Z_0}\int \mathcal{D}\phi e^{-i/\hbar \int d^4x(\frac{1}{2}\phi(\Box + m^2)\phi + \phi(\Box + m^2)\phi_0 + \frac{1}{2}\phi_0(\Box + m^2)\phi_0 - J(x)\phi)}. \tag{A.5}$$

The heterogeneous Klein-Gordon equation demands that

$$(\Box + m^2)\phi = J(x). \tag{A.6}$$

This equation can be solved by introducing the Feynman propagator $G(x, y)$ that satisfies,

$$(\Box + m^2)G(x, y) = \delta^4(x - y). \tag{A.7}$$

and hence,

$$\phi_0 = -\int G(x, y)J(y)d^4y. \tag{A.8}$$

If this expression is plugged into the generating functional the new Z[J] reads

$$Z[J] = \frac{1}{Z_0} e^{-\frac{i}{2\hbar}\int J(x)G(x,y)J(y)d^4xd^4y} \int \mathcal{D}\phi e^{-i/\hbar \int d^4x \frac{1}{2}\phi(\Box + m^2)\phi}. \tag{A.9}$$

Recall that,

$$Z_0 = \int \mathcal{D}\phi e^{-i/\hbar \int d^4x \frac{1}{2}\phi(\Box + m^2)\phi} \tag{A.10}$$

so the final expression reads

$$Z[J] = \exp\left[-\frac{i}{2}\int J(x)G(x, y)J(y)d^4xd^4y\right] \tag{A.11}$$

A.2 Wick's Theorem

The starting expression is the result of Appendix A.1.

$$Z[J] = \exp\left[-\frac{i}{2}\int J(x)G(x, y)J(y)d^4xd^4y\right] \tag{A.12}$$

This expression can be expanded in powers of J.

$$Z[J]=\sum_{n=0}^{\infty}\frac{1}{n!}\Big(-\frac{i}{2}\Big)^{n}\int d^4x_1...d^4x_{2n}J(x_1)...J(x_{2n})G(x_1,x_2)...G(x_{2n-1},x_{2n}) \quad \text{(A.13)}$$

Note that the $2n$ denotes that only even powers of J appear. If we use equation

$$\langle 0|T[\phi(x_1)...\phi(x_n)]|0\rangle=\frac{1}{i^n}\frac{\delta^n Z[J]}{\delta J(x_1)...J(x_n)}\bigg|_{J=0}. \quad \text{(A.14)}$$

we get the expression

$$\langle 0|T[\phi(x_1)...\phi(x_n)]|0\rangle=\frac{1}{n!}\Big(\frac{i}{2\hbar}\Big)^{n}\sum_{\sigma}G(\sigma_1,\sigma_2)...G(x_{2\sigma-1},x_{2\sigma}) \quad \text{(A.15)}$$

where the sum σ runs over (2n)! permutations of 1,...,2n. The final expression of Wick's theorem is obtained by taking into account the symmetry $G(x,y)=G(y,x)$.

$$\langle 0|T[\phi(x_1)...\phi(x_{2n})]|0\rangle=\sum_{\sigma}iG(x_{\sigma_1},x_{\sigma_2})...G(x_{\sigma_{2n-1}},x_{\sigma_{2n}}) \quad \text{(A.16)}$$

A.3 Vector Boson Masses

The starting expression is the Higgs Lagrangian 2.64 with the potential 2.65.

$$\mathcal{L}_H=(\partial^\mu\Phi)^\dagger(\partial_\mu\Phi)-V(\Phi)=\mu^2\Phi^\dagger\Phi+\lambda(\Phi^\dagger\Phi)^2 \quad \text{(A.17)}$$

Lets impose the left-handed doublet covariant derivative of the $SU(2)_L\otimes U(1)_Y$ gauge symmetry stated in equation 2.44 and include the complex scalar field in unitary gauge stated in equation 2.69. The kinetic terms become

$$\begin{aligned} D^\mu\begin{pmatrix}0\\ v+h(x)\end{pmatrix} &= (\vec{I}(\partial_\mu+\frac{g_1}{2}B_\mu)+ig_2\frac{\vec{\tau}}{2}\vec{W}_\mu \\ =\begin{pmatrix}0\\ \partial_\mu h(x)\end{pmatrix}+i\frac{g_2}{2}(g_1B_\mu-g_2W^3_\mu)&\begin{pmatrix}v+h(x)\\ 0\end{pmatrix}+i\frac{g_2}{2}(g_1B_\mu-g_2W^3_\mu)\end{aligned} \quad \text{(A.18)}$$

and

$$\left(D^{\mu}\begin{pmatrix}0\\ v+h(x)\end{pmatrix}\right)^{\dagger}=(0,\partial_{\mu}h(x))-i\frac{g_2}{2}(W_{\mu}^{1}+iW_{\mu}^{2})(0,v+h(x))$$
$$-i\frac{g_2}{2\sqrt{2}}(W_{\mu}^{1}-iW_{\mu}^{2})(0,v+h(x)). \tag{A.19}$$

Note that the following definition

$$\tau\cdot\vec{W}_{\mu}=\begin{pmatrix}W_{\mu}^{3} & W_{\mu}^{1}-iW_{\mu}^{2}\\ W_{\mu}^{1}+iW_{\mu}^{2} & W_{\mu}^{3}\end{pmatrix}=\begin{pmatrix}W_{\mu}^{3} & W_{\mu}^{+}\\ W_{\mu}^{-} & W_{\mu}^{3}\end{pmatrix} \tag{A.20}$$

and

If equations A.18, A.19 and A.20 are plugged into equation A.17 the Higgs-Gauge section is redefined as

$$\mathcal{L}_{HG}=\frac{1}{2}\partial_{\mu}h(x)\partial^{\mu}h(x)-\frac{\mu^{2}}{2}(v+h(x))^{2}-\frac{\lambda}{4}(v+h(x))^{4}$$
$$+\frac{g_2^{2}}{2}(v+h(x))^{2}W_{\mu}^{+}W^{\mu-}+\frac{1}{8}(g_1B^{\mu}-g_2W^{3\mu})(g_1B_{\mu}-g_2W_{\mu}^{3})(v+h(x))^{2}. \tag{A.21}$$

Additionally it is possible to redefine the fields as

$$\begin{pmatrix}W_{\mu}^{3}\\ B_{\mu}\end{pmatrix}=\begin{pmatrix}\cos\theta_W & \sin\theta_W\\ -\sin\theta_W & \cos\theta_W\end{pmatrix}\begin{pmatrix}Z_{\mu}\\ A_{\mu}\end{pmatrix} \tag{A.22}$$

with

$$\sin\theta_W=\frac{g_1}{(g_2^{2}+g_1^{2})^{1/2}}. \tag{A.23}$$

This gives the final expression with the mass terms for the W and Z bosons but leaving the photon massless.

$$\mathcal{L}_{HG}=\frac{1}{2}(\partial_{\mu}h)(\partial^{\mu}h)+\frac{g_2^{2}}{4}(v+h)^{2}W_{\mu}^{+}W^{-\mu}+\frac{1}{8}\frac{g_2^{2}}{cos^{2}(\theta_W)}(v+h)^{2}Z_{\mu}Z^{\mu}$$
$$+\frac{\mu^{2}}{2}(v+h)^{2}-\frac{\lambda}{4}(v+h)^{4}. \tag{A.24}$$

Appendix B

Optimization Plots

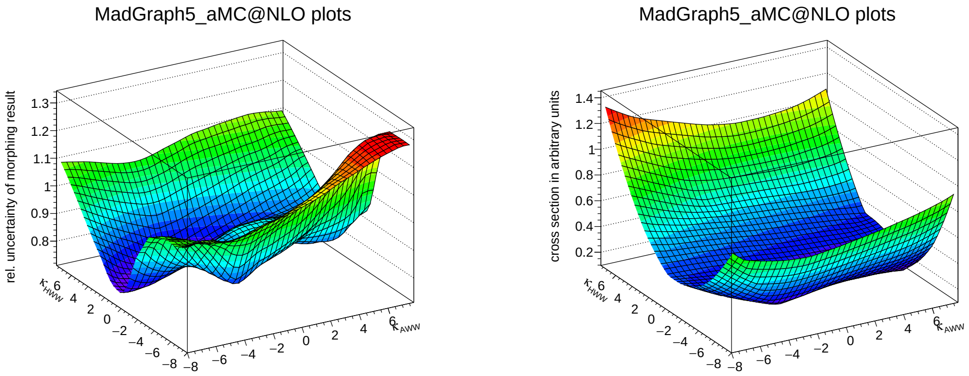

FIGURE B.1: Morphing result and relative uncertainty after three optimizations

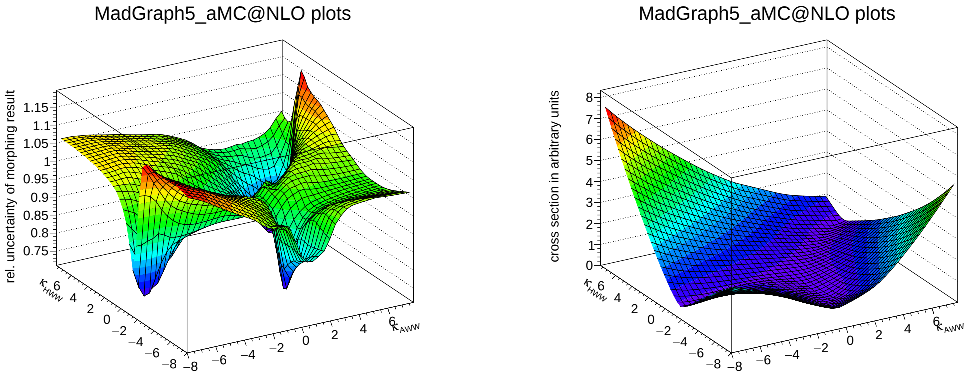

FIGURE B.2: Morphing result and relative uncertainty after three optimizations

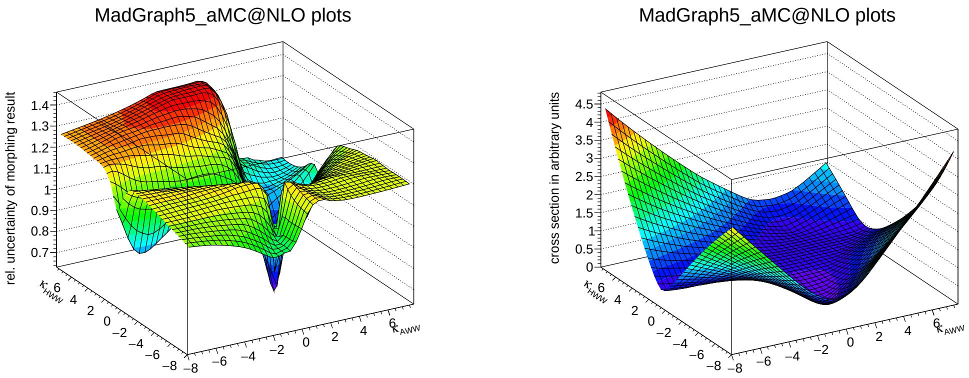

FIGURE B.3: Morphing result and relative uncertainty after three optimizations

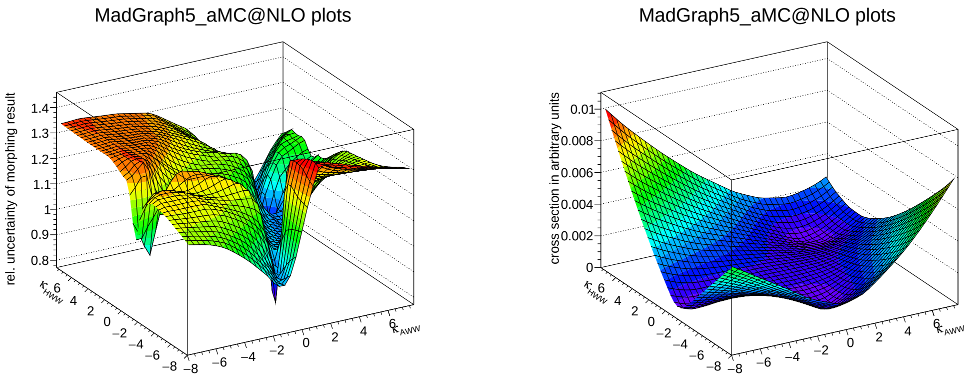

FIGURE B.4: Morphing result and relative uncertainty after three optimizations

Appendix C

Signal Region Fit Distributions

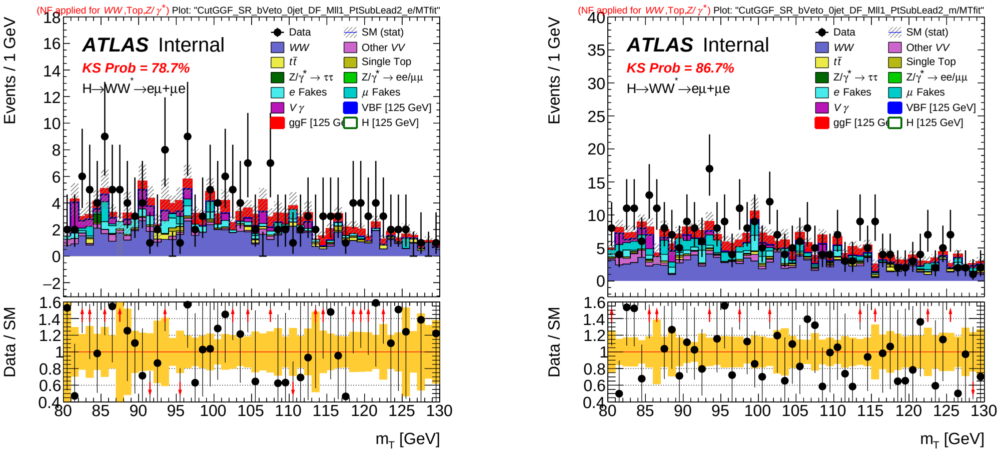

FIGURE C.1: Fit distributions of signal region 1(left) and 2(right) as defined in table 6.3 for $N_{jet} = 0$

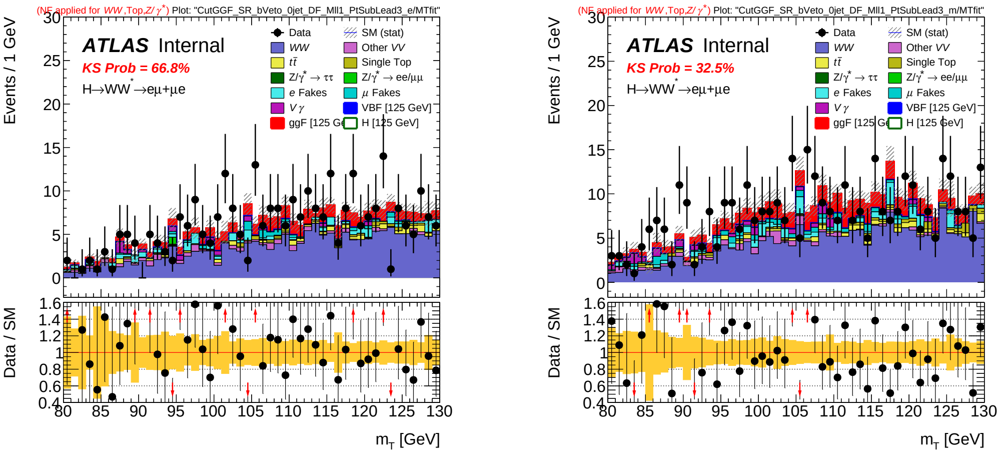

FIGURE C.2: Fit distributions of signal region 3(left) and 4(right) as defined in table 6.3 for $N_{jet} = 0$

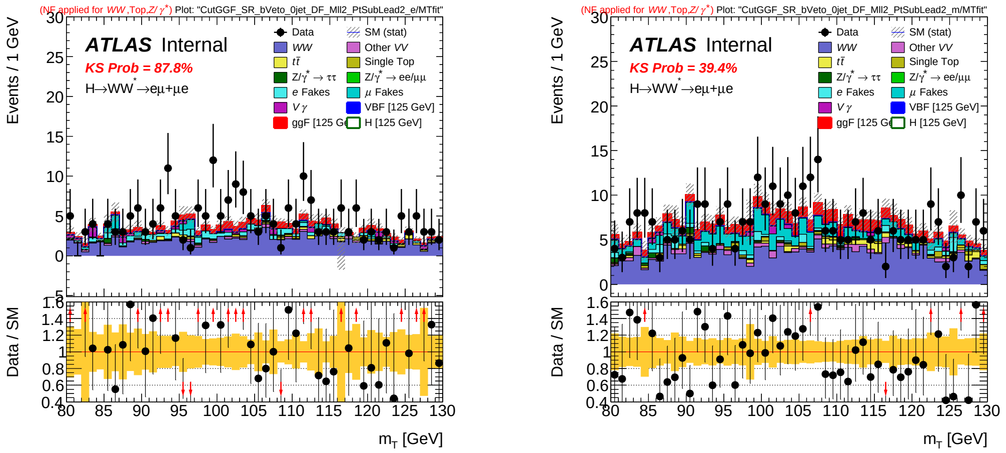

FIGURE C.3: Fit distributions of signal region 5(left) and 6(right) as defined in table 6.3 for $N_{jet} = 0$

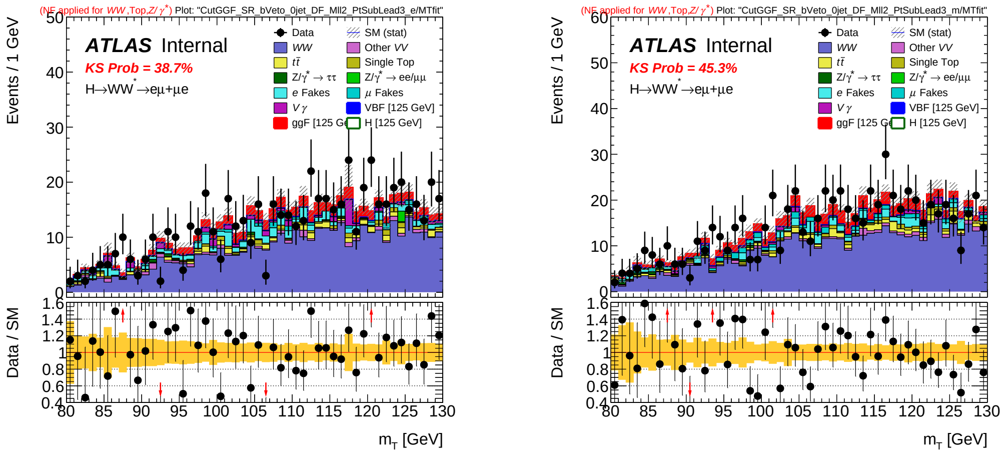

FIGURE C.4: Fit distributions of signal region 7(left) and 8(right) as defined in table 6.3 for $N_{jet} = 0$

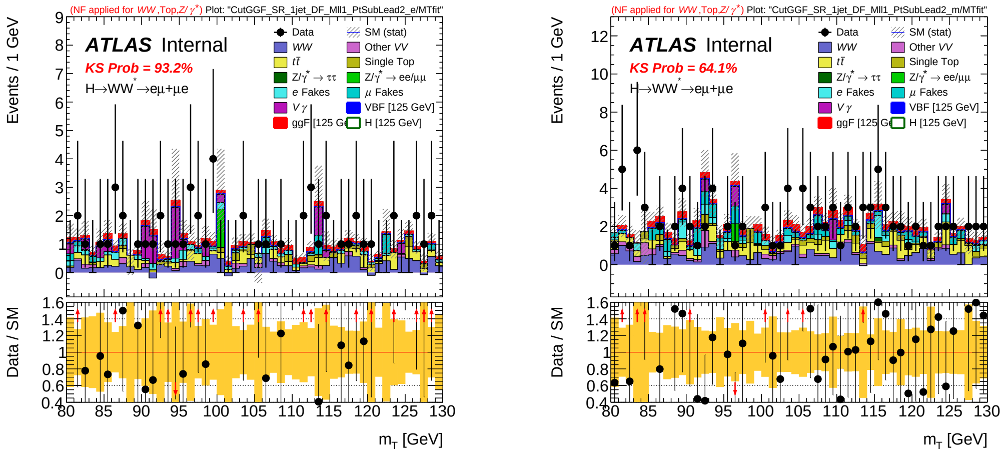

FIGURE C.5: Fit distributions of signal region 1(left) and 2(right) as defined in table 6.3 for $N_{jet} = 1$

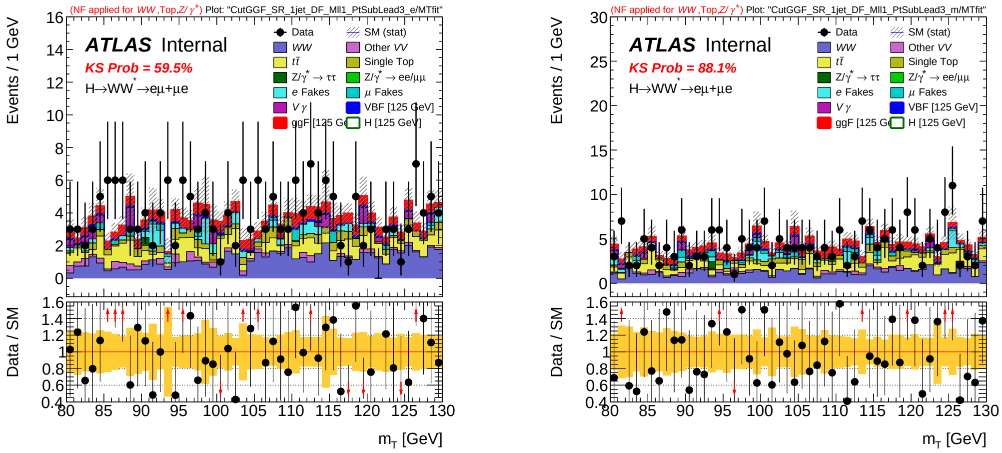

FIGURE C.6: Fit distributions of signal region 3(left) and 4(right) as defined in table 6.3 for $N_{jet} = 1$

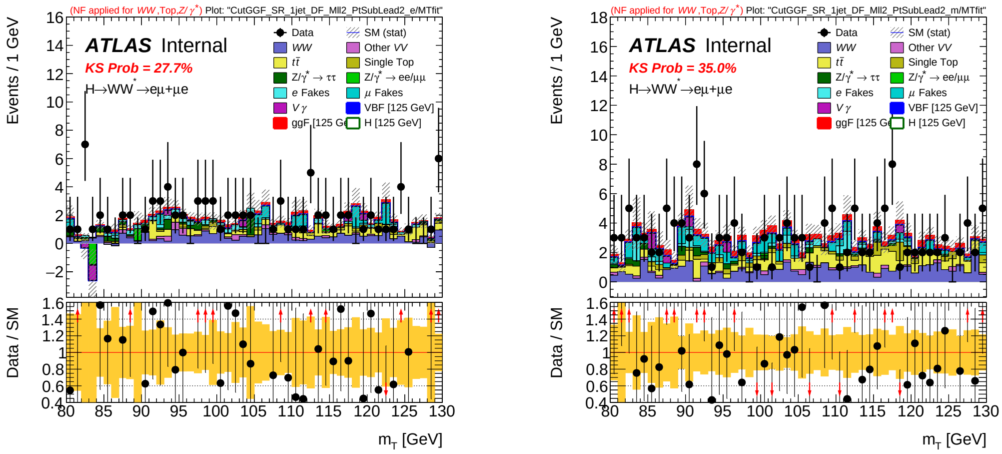

FIGURE C.7: Fit distributions of signal region 5(left) and 6(right) as defined in table 6.3 for $N_{jet} = 1$

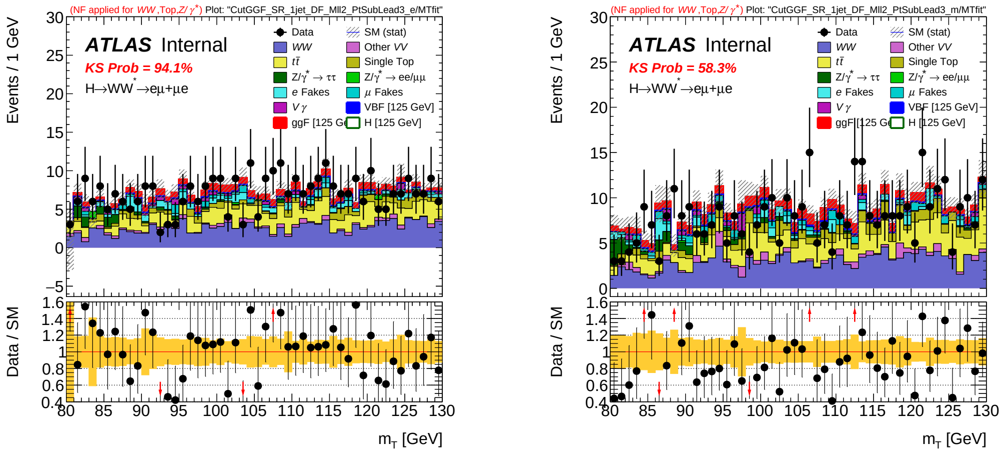

FIGURE C.8: Fit distributions of signal region 7(left) and 8(right) as defined in table 6.3 for $N_{jet} = 1$

Appendix D

Validation Plots

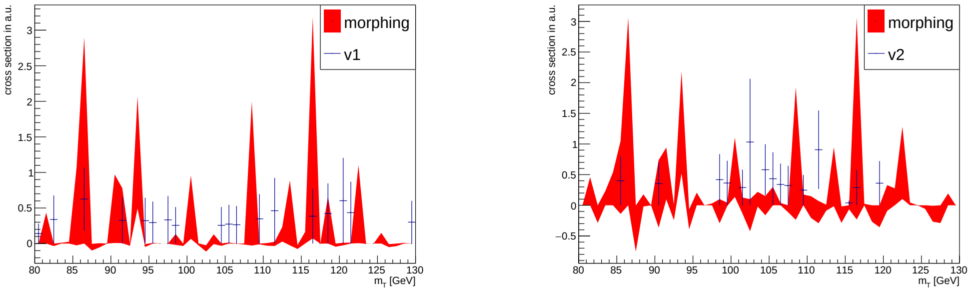

FIGURE D.1: Validation plots for the base samples in signal region 3 as defined in table 6.3 for $N_{jet} = 1$

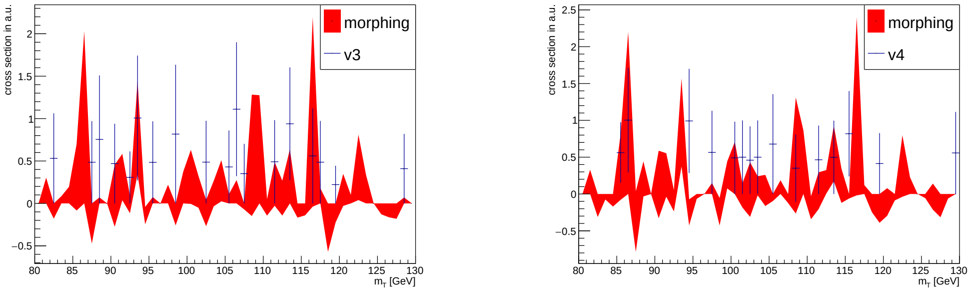

FIGURE D.2: Validation plots for the base samples in signal region 3 as defined in table 6.3 for $N_{jet} = 1$

Appendix E

Cut Flow

E.1 Signal Strength Signal Cut Flow

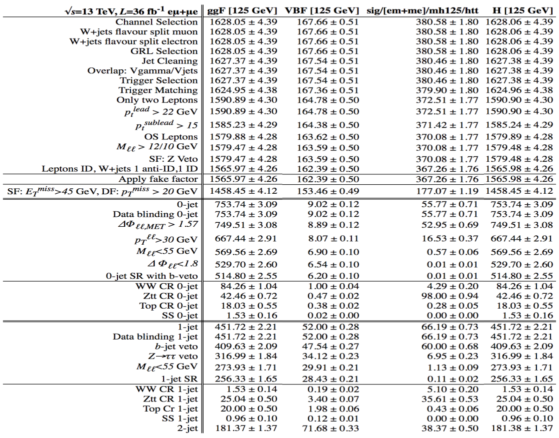

$\sqrt{s}$=13 TeV, L=36 fb^{-1} eμ+μe	ggF [125 GeV]	VBF [125 GeV]	sig/[em+me]/mh125/htt	H [125 GeV]
Channel Selection	1628.05 ± 4.39	167.66 ± 0.51	380.58 ± 1.80	1628.06 ± 4.39
W+jets flavour split muon	1628.05 ± 4.39	167.66 ± 0.51	380.58 ± 1.80	1628.06 ± 4.39
W+jets flavour split electron	1628.05 ± 4.39	167.66 ± 0.51	380.58 ± 1.80	1628.06 ± 4.39
GRL Selection	1628.05 ± 4.39	167.66 ± 0.51	380.58 ± 1.80	1628.06 ± 4.39
Jet Cleaning	1627.37 ± 4.39	167.54 ± 0.51	380.46 ± 1.80	1627.38 ± 4.39
Overlap: Vgamma/Vjets	1627.37 ± 4.39	167.54 ± 0.51	380.46 ± 1.80	1627.38 ± 4.39
Trigger Selection	1627.37 ± 4.39	167.54 ± 0.51	380.46 ± 1.80	1627.38 ± 4.39
Trigger Matching	1624.95 ± 4.38	167.36 ± 0.51	379.90 ± 1.80	1624.96 ± 4.38
Only two Leptons	1590.89 ± 4.30	164.78 ± 0.50	372.51 ± 1.77	1590.90 ± 4.30
$p_t^{lead} > 22$ GeV	1590.89 ± 4.30	164.78 ± 0.50	372.51 ± 1.77	1590.90 ± 4.30
$p_t^{sublead} > 15$	1585.23 ± 4.29	164.38 ± 0.50	371.42 ± 1.77	1585.24 ± 4.29
OS Leptons	1579.88 ± 4.28	163.62 ± 0.50	370.08 ± 1.77	1579.89 ± 4.28
$M_{\ell\ell} > 12/10$ GeV	1579.47 ± 4.28	163.59 ± 0.50	370.08 ± 1.77	1579.48 ± 4.28
SF: Z Veto	1579.47 ± 4.28	163.59 ± 0.50	370.08 ± 1.77	1579.48 ± 4.28
Leptons ID, W+jets 1 anti-ID,1 ID	1565.97 ± 4.26	162.39 ± 0.50	367.26 ± 1.76	1565.98 ± 4.26
Apply fake factor	1565.97 ± 4.26	162.39 ± 0.50	367.26 ± 1.76	1565.98 ± 4.26
SF: E_T^{miss}>45 GeV, DF: $p_T^{miss} > 20$ GeV	1458.45 ± 4.12	153.46 ± 0.49	177.07 ± 1.19	1458.45 ± 4.12
0-jet	753.74 ± 3.09	9.02 ± 0.12	55.77 ± 0.71	753.74 ± 3.09
Data blinding 0-jet	753.74 ± 3.09	9.02 ± 0.12	55.77 ± 0.71	753.74 ± 3.09
$\Delta\Phi_{\ell\ell,MET} > 1.57$	749.51 ± 3.08	8.89 ± 0.12	52.95 ± 0.69	749.51 ± 3.08
$p_T^{\ell\ell}$>30 GeV	667.44 ± 2.91	8.07 ± 0.11	16.53 ± 0.37	667.44 ± 2.91
$M_{\ell\ell}$<55 GeV	569.56 ± 2.69	6.90 ± 0.10	0.57 ± 0.06	569.56 ± 2.69
$\Delta\,\Phi_{\ell\ell}<1.8$	529.70 ± 2.60	6.54 ± 0.10	0.01 ± 0.01	529.70 ± 2.60
0-jet SR with b-veto	514.80 ± 2.55	6.20 ± 0.10	0.01 ± 0.01	514.80 ± 2.55
WW CR 0-jet	84.26 ± 1.04	1.00 ± 0.04	4.29 ± 0.20	84.26 ± 1.04
Ztt CR 0-jet	42.46 ± 0.72	0.47 ± 0.02	98.00 ± 0.94	42.46 ± 0.72
Top CR 0-jet	18.03 ± 0.55	0.38 ± 0.02	0.28 ± 0.05	18.03 ± 0.55
SS 0-jet	1.53 ± 0.16	0.02 ± 0.00	0.00 ± 0.00	1.53 ± 0.16
1-jet	451.72 ± 2.21	52.00 ± 0.28	66.19 ± 0.73	451.72 ± 2.21
Data blinding 1-jet	451.72 ± 2.21	52.00 ± 0.28	66.19 ± 0.73	451.72 ± 2.21
b-jet veto	409.63 ± 2.09	47.54 ± 0.27	60.00 ± 0.68	409.63 ± 2.09
$Z\rightarrow\tau\tau$ veto	316.99 ± 1.84	34.12 ± 0.23	6.95 ± 0.23	316.99 ± 1.84
$M_{\ell\ell}$<55 GeV	273.93 ± 1.71	29.91 ± 0.21	1.13 ± 0.09	273.93 ± 1.71
1-jet SR	256.33 ± 1.65	28.43 ± 0.21	0.11 ± 0.02	256.33 ± 1.65
WW CR 1-jet	1.53 ± 0.14	0.19 ± 0.02	5.10 ± 0.20	1.53 ± 0.14
Ztt CR 1-jet	25.04 ± 0.50	3.40 ± 0.07	35.61 ± 0.53	25.04 ± 0.50
Top Cr 1-jet	20.00 ± 0.50	1.98 ± 0.06	0.43 ± 0.06	20.00 ± 0.50
SS 1-jet	0.96 ± 0.10	0.12 ± 0.01	0.00 ± 0.00	0.96 ± 0.10
2-jet	181.37 ± 1.37	71.68 ± 0.33	38.37 ± 0.50	181.38 ± 1.37

Figure E.1: Cut flow of the signal samples of the signal strength analysis

E.2 EFT Coupling Signal Cut Flow

E.3 Shared Background Cut Flow

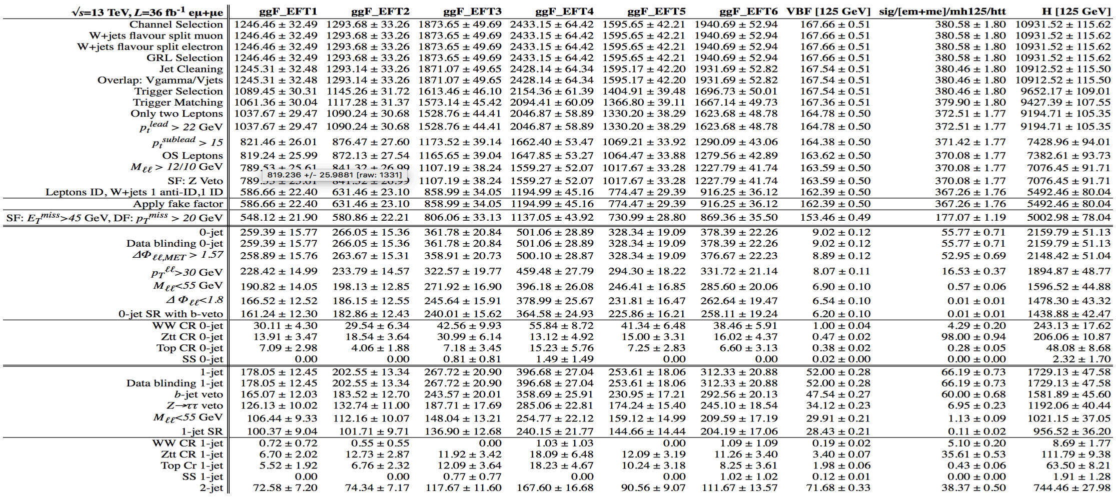

$\sqrt{s}$=13 TeV, L=36 fb^{-1} eμ+μe	ggF_EFT1	ggF_EFT2	ggF_EFT3	ggF_EFT4	ggF_EFT5	ggF_EFT6	VBF [125 GeV]	sig/[em+me]/mh125/htt	H [125 GeV]
Channel Selection	1246.46 ± 32.49	1293.68 ± 33.26	1873.65 ± 49.69	2433.15 ± 64.42	1595.65 ± 42.21	1940.69 ± 52.94	167.66 ± 0.51	380.58 ± 1.80	10931.52 ± 115.62
W+jets flavour split muon	1246.46 ± 32.49	1293.68 ± 33.26	1873.65 ± 49.69	2433.15 ± 64.42	1595.65 ± 42.21	1940.69 ± 52.94	167.66 ± 0.51	380.58 ± 1.80	10931.52 ± 115.62
W+jets flavour split electron	1246.46 ± 32.49	1293.68 ± 33.26	1873.65 ± 49.69	2433.15 ± 64.42	1595.65 ± 42.21	1940.69 ± 52.94	167.66 ± 0.51	380.58 ± 1.80	10931.52 ± 115.62
GRL Selection	1246.46 ± 32.49	1293.68 ± 33.26	1873.65 ± 49.69	2433.15 ± 64.42	1595.65 ± 42.21	1940.69 ± 52.94	167.66 ± 0.51	380.58 ± 1.80	10931.52 ± 115.62
Jet Cleaning	1245.31 ± 32.48	1293.14 ± 33.26	1871.07 ± 49.65	2428.14 ± 64.34	1595.17 ± 42.20	1931.69 ± 52.82	167.54 ± 0.51	380.46 ± 1.80	10912.52 ± 115.50
Overlap: Vgamma/Vjets	1245.31 ± 32.48	1293.14 ± 33.26	1871.07 ± 49.65	2428.14 ± 64.34	1595.17 ± 42.20	1931.69 ± 52.82	167.54 ± 0.51	380.46 ± 1.80	10912.52 ± 115.50
Trigger Selection	1089.45 ± 30.31	1145.26 ± 31.72	1613.46 ± 46.10	2154.36 ± 61.39	1404.91 ± 39.48	1696.73 ± 50.01	167.54 ± 0.51	380.46 ± 1.80	9652.17 ± 109.01
Trigger Matching	1061.36 ± 30.04	1117.28 ± 31.37	1573.14 ± 45.42	2094.41 ± 60.09	1366.80 ± 39.11	1667.14 ± 49.73	167.36 ± 0.51	379.90 ± 1.80	9427.39 ± 107.55
Only two Leptons	1037.67 ± 29.47	1090.24 ± 30.68	1528.76 ± 44.41	2046.87 ± 58.89	1330.20 ± 38.29	1623.68 ± 48.78	164.78 ± 0.50	372.51 ± 1.77	9194.71 ± 105.35
$p_t^{lead} > 22$ GeV	1037.67 ± 29.47	1090.24 ± 30.68	1528.76 ± 44.41	2046.87 ± 58.89	1330.20 ± 38.29	1623.68 ± 48.78	164.78 ± 0.50	372.51 ± 1.77	9194.71 ± 105.35
$p_t^{sublead} > 15$	821.46 ± 26.01	876.47 ± 27.60	1173.52 ± 39.14	1662.40 ± 53.47	1069.21 ± 33.92	1290.09 ± 43.06	164.38 ± 0.50	371.42 ± 1.77	7428.96 ± 94.01
OS Leptons	819.24 ± 25.99	872.13 ± 27.54	1165.65 ± 39.04	1647.85 ± 53.27	1064.47 ± 33.88	1279.56 ± 42.89	163.62 ± 0.50	370.08 ± 1.77	7382.61 ± 93.73
$M_{\ell\ell} > 12/10$ GeV	789.53 ± 25.61	841.32 ± 26.99	1107.19 ± 38.24	1559.27 ± 52.07	1017.67 ± 33.28	1227.79 ± 41.74	163.59 ± 0.50	370.08 ± 1.77	7076.45 ± 91.71
SF: Z Veto	789.53 ± 25.61	841.32 ± 26.99	1107.19 ± 38.24	1559.27 ± 52.07	1017.67 ± 33.28	1227.79 ± 41.74	163.59 ± 0.50	370.08 ± 1.77	7076.45 ± 91.71
Leptons ID, W+jets 1 anti-ID,1 ID	586.66 ± 22.40	631.46 ± 23.10	858.99 ± 34.05	1194.99 ± 45.16	774.47 ± 29.39	916.25 ± 36.12	162.39 ± 0.50	367.26 ± 1.76	5492.46 ± 80.04
Apply fake factor	586.66 ± 22.40	631.46 ± 23.10	858.99 ± 34.05	1194.99 ± 45.16	774.47 ± 29.39	916.25 ± 36.12	162.39 ± 0.50	367.26 ± 1.76	5492.46 ± 80.04
SF: $E_T{}^{miss}$>45 GeV, DF: $p_T{}^{miss} > 20$ GeV	548.12 ± 21.90	580.86 ± 22.21	806.06 ± 33.13	1137.05 ± 43.92	730.99 ± 28.80	869.36 ± 35.50	153.46 ± 0.49	177.07 ± 1.19	5002.98 ± 78.04
0-jet	259.39 ± 15.77	266.05 ± 15.36	361.78 ± 20.84	501.06 ± 28.89	328.34 ± 19.09	378.39 ± 22.26	9.02 ± 0.12	55.77 ± 0.71	2159.79 ± 51.13
Data blinding 0-jet	259.39 ± 15.77	266.05 ± 15.36	361.78 ± 20.84	501.06 ± 28.89	328.34 ± 19.09	378.39 ± 22.26	9.02 ± 0.12	55.77 ± 0.71	2159.79 ± 51.13
$\Delta\Phi_{\ell\ell,MET} > 1.57$	258.89 ± 15.76	263.67 ± 15.31	358.91 ± 20.73	500.10 ± 28.87	328.34 ± 19.09	376.67 ± 22.23	8.89 ± 0.12	52.95 ± 0.69	2148.42 ± 51.04
$p_T{}^{\ell\ell}$>30 GeV	228.42 ± 14.99	233.79 ± 14.57	322.57 ± 19.77	459.48 ± 27.79	294.30 ± 18.22	331.72 ± 21.14	8.07 ± 0.11	16.53 ± 0.37	1894.87 ± 48.77
$M_{\ell\ell}$<55 GeV	190.82 ± 14.05	198.13 ± 12.85	271.92 ± 16.90	396.18 ± 26.08	246.41 ± 16.85	285.60 ± 20.06	6.90 ± 0.10	0.57 ± 0.06	1596.52 ± 44.88
$\Delta\,\Phi_{\ell\ell}$<1.8	166.52 ± 12.52	186.15 ± 12.55	245.64 ± 15.91	378.99 ± 25.67	231.81 ± 16.47	262.64 ± 19.47	6.54 ± 0.10	0.01 ± 0.01	1478.30 ± 43.32
0-jet SR with b-veto	161.24 ± 12.30	182.86 ± 12.43	240.01 ± 15.62	364.58 ± 24.93	225.86 ± 16.21	258.11 ± 19.24	6.20 ± 0.10	0.01 ± 0.01	1438.88 ± 42.47
WW CR 0-jet	30.11 ± 4.30	29.54 ± 6.34	42.56 ± 9.93	55.84 ± 8.72	41.34 ± 6.48	38.46 ± 5.91	1.00 ± 0.04	4.29 ± 0.20	243.13 ± 17.62
Ztt CR 0-jet	13.91 ± 3.47	18.54 ± 3.64	30.99 ± 6.14	13.12 ± 4.92	15.00 ± 3.31	16.02 ± 4.37	0.47 ± 0.02	98.00 ± 0.94	206.06 ± 10.87
Top CR 0-jet	7.09 ± 2.98	4.06 ± 1.88	7.18 ± 3.45	15.23 ± 5.76	7.25 ± 2.83	6.60 ± 3.13	0.38 ± 0.02	0.28 ± 0.05	48.08 ± 8.68
SS 0-jet	0.00	0.00	0.81 ± 0.81	1.49 ± 1.49	0.00	0.00	0.02 ± 0.00	0.00 ± 0.00	2.32 ± 1.70
1-jet	178.05 ± 12.45	202.55 ± 13.34	267.72 ± 20.90	396.68 ± 27.04	253.61 ± 18.06	312.33 ± 20.88	52.00 ± 0.28	66.19 ± 0.73	1729.13 ± 47.58
Data blinding 1-jet	178.05 ± 12.45	202.55 ± 13.34	267.72 ± 20.90	396.68 ± 27.04	253.61 ± 18.06	312.33 ± 20.88	52.00 ± 0.28	66.19 ± 0.73	1729.13 ± 47.58
b-jet veto	165.07 ± 12.03	183.52 ± 12.70	243.57 ± 20.01	358.69 ± 25.91	230.95 ± 17.21	292.56 ± 20.13	47.54 ± 0.27	60.00 ± 0.68	1581.89 ± 45.60
$Z\rightarrow\tau\tau$ veto	126.13 ± 10.02	132.74 ± 11.00	187.71 ± 17.69	285.06 ± 22.81	174.24 ± 15.40	245.10 ± 18.54	34.12 ± 0.23	6.95 ± 0.23	1192.06 ± 40.44
$M_{\ell\ell}$<55 GeV	106.44 ± 9.33	112.16 ± 10.07	148.04 ± 13.21	254.77 ± 22.12	159.12 ± 14.99	209.59 ± 17.19	29.91 ± 0.21	1.13 ± 0.09	1021.15 ± 37.05
1-jet SR	100.37 ± 9.04	101.71 ± 9.71	136.90 ± 12.68	240.15 ± 21.77	144.66 ± 14.44	204.19 ± 17.06	28.43 ± 0.21	0.11 ± 0.02	956.52 ± 36.20
WW CR 1-jet	0.72 ± 0.72	0.55 ± 0.55	0.00	1.03 ± 1.03	0.00	1.09 ± 1.09	0.19 ± 0.02	5.10 ± 0.20	8.69 ± 1.77
Ztt CR 1-jet	6.70 ± 2.02	12.73 ± 2.87	11.92 ± 3.42	18.09 ± 6.48	12.09 ± 3.19	11.26 ± 3.40	3.40 ± 0.07	35.61 ± 0.53	111.79 ± 9.38
Top Cr 1-jet	5.52 ± 1.92	6.76 ± 2.32	12.09 ± 3.64	18.23 ± 4.67	10.24 ± 3.18	8.25 ± 3.61	1.98 ± 0.06	0.43 ± 0.06	63.50 ± 8.21
SS 1-jet	0.00	0.00	0.77 ± 0.77	0.00	0.00	1.02 ± 1.02	0.12 ± 0.01	0.00 ± 0.00	1.91 ± 1.28
2-jet	72.58 ± 7.20	74.34 ± 7.17	117.67 ± 11.60	167.60 ± 16.68	90.56 ± 9.07	111.67 ± 13.57	71.68 ± 0.33	38.37 ± 0.50	744.46 ± 27.98

FIGURE E.2: Cut flow of the signal samples of the EFT coupling analysis

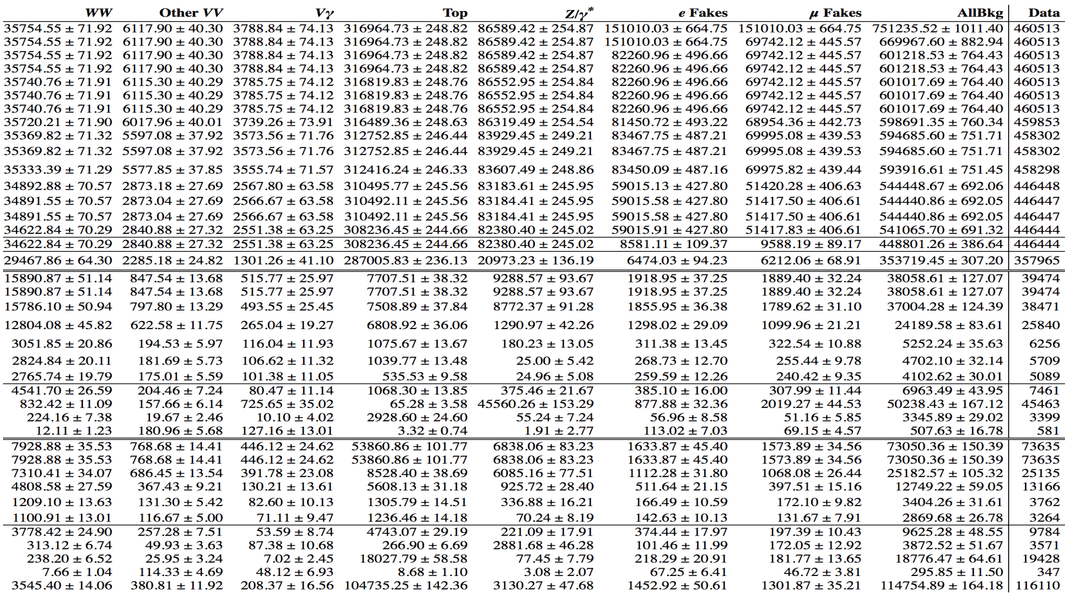

WW	Other VV	$V\gamma$	Top	Z/γ^*	e Fakes	μ Fakes	AllBkg	Data
35754.55 ± 71.92	6117.90 ± 40.30	3788.84 ± 74.13	316964.73 ± 248.82	86589.42 ± 254.87	151010.03 ± 664.75	151010.03 ± 664.75	751235.52 ± 1011.40	460513
35754.55 ± 71.92	6117.90 ± 40.30	3788.84 ± 74.13	316964.73 ± 248.82	86589.42 ± 254.87	151010.03 ± 664.75	69742.12 ± 445.57	669967.60 ± 882.94	460513
35754.55 ± 71.92	6117.90 ± 40.30	3788.84 ± 74.13	316964.73 ± 248.82	86589.42 ± 254.87	82260.96 ± 496.66	69742.12 ± 445.57	601218.53 ± 764.43	460513
35754.55 ± 71.92	6117.90 ± 40.30	3788.84 ± 74.13	316964.73 ± 248.82	86589.42 ± 254.87	82260.96 ± 496.66	69742.12 ± 445.57	601218.53 ± 764.43	460513
35740.76 ± 71.91	6115.30 ± 40.29	3785.75 ± 74.12	316819.83 ± 248.76	86552.95 ± 254.84	82260.96 ± 496.66	69742.12 ± 445.57	601017.69 ± 764.40	460513
35740.76 ± 71.91	6115.30 ± 40.29	3785.75 ± 74.12	316819.83 ± 248.76	86552.95 ± 254.84	82260.96 ± 496.66	69742.12 ± 445.57	601017.69 ± 764.40	460513
35740.76 ± 71.91	6115.30 ± 40.29	3785.75 ± 74.12	316819.83 ± 248.76	86552.95 ± 254.84	82260.96 ± 496.66	69742.12 ± 445.57	601017.69 ± 764.40	460513
35720.21 ± 71.90	6017.96 ± 40.01	3739.26 ± 73.91	316489.36 ± 248.63	86319.49 ± 254.54	81450.72 ± 493.22	68954.36 ± 442.73	598691.35 ± 760.34	459853
35369.82 ± 71.32	5597.08 ± 37.92	3573.56 ± 71.76	312752.85 ± 246.44	83929.45 ± 249.21	83467.75 ± 487.21	69995.08 ± 439.53	594685.60 ± 751.71	458302
35369.82 ± 71.32	5597.08 ± 37.92	3573.56 ± 71.76	312752.85 ± 246.44	83929.45 ± 249.21	83467.75 ± 487.21	69995.08 ± 439.53	594685.60 ± 751.71	458302
35333.39 ± 71.29	5577.85 ± 37.85	3555.74 ± 71.57	312416.24 ± 246.33	83607.49 ± 248.86	83450.09 ± 487.16	69975.82 ± 439.44	593916.61 ± 751.45	458298
34892.88 ± 70.57	2873.18 ± 27.69	2567.80 ± 63.58	310495.77 ± 245.56	83183.61 ± 245.95	59015.13 ± 427.80	51420.28 ± 406.63	544448.67 ± 692.06	446448
34891.55 ± 70.57	2873.04 ± 27.69	2566.67 ± 63.58	310492.11 ± 245.56	83184.41 ± 245.95	59015.58 ± 427.80	51417.50 ± 406.61	544440.86 ± 692.05	446447
34891.55 ± 70.57	2873.04 ± 27.69	2566.67 ± 63.58	310492.11 ± 245.56	83184.41 ± 245.95	59015.58 ± 427.80	51417.50 ± 406.61	544440.86 ± 692.05	446447
34622.84 ± 70.29	2840.88 ± 27.32	2551.38 ± 63.25	308236.45 ± 244.66	82380.40 ± 245.02	59015.91 ± 427.80	51417.83 ± 406.61	541065.70 ± 691.32	446444
34622.84 ± 70.29	2840.88 ± 27.32	2551.38 ± 63.25	308236.45 ± 244.66	82380.40 ± 245.02	8581.11 ± 109.37	9588.19 ± 89.17	448801.26 ± 386.64	446444
29467.86 ± 64.30	2285.18 ± 24.82	1301.26 ± 41.10	287005.83 ± 236.13	20973.23 ± 136.19	6474.03 ± 94.23	6212.06 ± 68.91	353719.45 ± 307.20	357965
15890.87 ± 51.14	847.54 ± 13.68	515.77 ± 25.97	7707.51 ± 38.32	9288.57 ± 93.67	1918.95 ± 37.25	1889.40 ± 32.24	38058.61 ± 127.07	39474
15890.87 ± 51.14	847.54 ± 13.68	515.77 ± 25.97	7707.51 ± 38.32	9288.57 ± 93.67	1918.95 ± 37.25	1889.40 ± 32.24	38058.61 ± 127.07	39474
15786.10 ± 50.94	797.80 ± 13.29	493.55 ± 25.45	7508.89 ± 37.84	8772.37 ± 91.28	1855.95 ± 36.38	1789.62 ± 31.10	37004.28 ± 124.39	38471
12804.08 ± 45.82	622.58 ± 11.75	265.04 ± 19.27	6808.92 ± 36.06	1290.97 ± 42.26	1298.02 ± 29.09	1099.96 ± 21.21	24189.58 ± 83.61	25840
3051.85 ± 20.86	194.53 ± 5.97	116.04 ± 11.93	1075.67 ± 13.67	180.23 ± 13.05	311.38 ± 13.45	322.54 ± 10.88	5252.24 ± 35.63	6256
2824.84 ± 20.11	181.69 ± 5.73	106.62 ± 11.32	1039.77 ± 13.48	25.00 ± 5.42	268.73 ± 12.70	255.44 ± 9.78	4702.10 ± 32.14	5709
2765.74 ± 19.79	175.01 ± 5.59	101.38 ± 11.05	535.53 ± 9.58	24.96 ± 5.08	259.59 ± 12.26	240.42 ± 9.35	4102.62 ± 30.01	5089
4541.70 ± 26.59	204.46 ± 7.24	80.47 ± 11.14	1068.30 ± 13.85	375.46 ± 21.67	385.10 ± 16.00	307.99 ± 11.44	6963.49 ± 43.95	7461
832.42 ± 11.09	157.66 ± 6.14	725.65 ± 35.02	65.28 ± 3.58	45560.26 ± 153.29	877.88 ± 32.36	2019.27 ± 44.53	50238.43 ± 167.12	45463
224.16 ± 7.38	19.67 ± 2.46	10.10 ± 4.02	2928.60 ± 24.60	55.24 ± 7.24	56.96 ± 8.58	51.16 ± 5.85	3345.89 ± 29.02	3399
12.11 ± 1.23	180.96 ± 5.68	127.16 ± 13.01	3.32 ± 0.74	1.91 ± 2.77	113.02 ± 7.03	69.15 ± 4.57	507.63 ± 16.78	581
7928.88 ± 35.53	768.68 ± 14.41	446.12 ± 24.62	53860.86 ± 101.77	6838.06 ± 83.23	1633.87 ± 45.40	1573.89 ± 34.56	73050.36 ± 150.39	73635
7928.88 ± 35.53	768.68 ± 14.41	446.12 ± 24.62	53860.86 ± 101.77	6838.06 ± 83.23	1633.87 ± 45.40	1573.89 ± 34.56	73050.36 ± 150.39	73635
7310.41 ± 34.07	686.45 ± 13.54	391.78 ± 23.08	8528.40 ± 38.69	6085.16 ± 77.51	1112.28 ± 31.80	1068.08 ± 26.44	25182.57 ± 105.32	25135
4808.58 ± 27.59	367.43 ± 9.21	130.21 ± 13.61	5608.13 ± 31.18	925.72 ± 28.40	511.64 ± 21.15	397.51 ± 15.16	12749.22 ± 59.05	13166
1209.10 ± 13.63	131.30 ± 5.42	82.60 ± 10.13	1305.79 ± 14.51	336.88 ± 16.21	166.49 ± 10.59	172.10 ± 9.82	3404.26 ± 31.61	3762
1100.91 ± 13.01	116.67 ± 5.00	71.11 ± 9.47	1236.46 ± 14.18	70.24 ± 8.19	142.63 ± 10.13	131.67 ± 7.91	2869.68 ± 26.78	3264
3778.42 ± 24.90	257.28 ± 7.51	53.59 ± 8.74	4743.07 ± 29.19	221.09 ± 17.91	374.44 ± 17.97	197.39 ± 10.43	9625.28 ± 48.55	9784
313.12 ± 6.74	49.93 ± 3.63	87.38 ± 10.68	266.90 ± 6.69	2881.68 ± 46.28	101.46 ± 11.99	172.05 ± 12.92	3872.52 ± 51.67	3571
238.20 ± 6.52	25.95 ± 3.24	7.02 ± 2.45	18027.79 ± 58.58	77.45 ± 7.79	218.29 ± 20.91	181.77 ± 13.65	18776.47 ± 64.61	19428
7.66 ± 1.04	114.33 ± 4.69	48.12 ± 6.93	8.68 ± 1.10	3.08 ± 2.07	67.25 ± 6.41	46.72 ± 3.81	295.85 ± 11.50	347
3545.40 ± 14.06	380.81 ± 11.92	208.37 ± 16.56	104735.25 ± 142.36	3130.27 ± 47.68	1452.92 ± 50.61	1301.87 ± 35.21	114754.89 ± 164.18	116110

FIGURE E.3: Cut flow of the background samples

Bibliography

[1] Measurement of gluon fusion and vector boson fusion Higgs boson production cross-sections in the $H \rightarrow WW^* \rightarrow e\nu\mu\nu$ decay channel in pp collisions at $\sqrt{s} = 13$ TeV with the ATLAS detector. Technical Report ATLAS-CONF-2018-004, CERN, Geneva, Mar 2018. URL https://cds.cern.ch/record/2308392.

[2] D. Galbraith and Burgard C. The standard model of particle physics. URL http://davidgalbraith.org/portfolio/ux-standard-model-of-the-standard-model/.

[3] Wikipedia. Principle of least action. URL https://en.wikipedia.org/wiki/Principle_of_least_action.

[4] M. Thomson. *Modern Particle Physics*. 2013.

[5] E. Mobs. Cern complex. URL https://cds.cern.ch/record/2197559.

[6] The ATLAS Collaboration and G Aad et al. The atlas experiment at the cern large hadron collider. *Journal of Instrumentation*, 3(08):S08003, 2008. URL http://stacks.iop.org/1748-0221/3/i=08/a=S08003.

[7] M Capeans, G Darbo, K Einsweiller, M Elsing, T Flick, M Garcia-Sciveres, C Gemme, H Pernegger, O Rohne, and R Vuillermet. ATLAS Insertable B-Layer Technical Design Report. Technical Report CERN-LHCC-2010-013. ATLAS-TDR-19, Sep 2010. URL http://cds.cern.ch/record/1291633.

[8] Ana Maria Henriques Correia. The ATLAS Tile Calorimeter. Technical Report ATL-TILECAL-PROC-2015-002, CERN, Geneva, Mar 2015. URL https://cds.cern.ch/record/2004868.

[9] ATLAS muon spectrometer: Technical Design Report. 1997. URL https://cds.cern.ch/record/331068.

[10] J. Goodson. Atlas magnetic system. URL http://www.jetgoodson.com/images/thesisImages/magnetSystems.png.

[11] B.P. Kersevan and S. Campana. Atlas computing model evolution. URL https://indico.cern.ch/event/352570/contributions/828856/attachments/698253/958799/CHLEComputingModelEvolution.pdf.

[12] M. Aaboud et al. Performance of the ATLAS Track Reconstruction Algorithms in Dense Environments in LHC Run 2. *Eur. Phys. J.*, C77(10):673, 2017. doi: 10.1140/epjc/s10052-017-5225-7.

[13] E. Bouhova-Thacker, P. Lichard, V. Kostyukhin, W. Liebig, M. Limper, G. Piacquadio, P. Lichard, C. Weiser, and A. Wildauer. Vertex Reconstruction in the ATLAS Experiment at the LHC. 2009.

[14] Rebeca Gonzalez Suarez. Recent CMS results in top and Higgs physics. *Mod. Phys. Lett.*, A32(29):1730026, 2017. doi: 10.1142/S0217732317300269.

[15] Giada Mancini and Roberto Covarelli. Overview of the Higgs boson property studies at the LHC. Higgs boson properties in the Standard Model. *PoS*, PP@LHC2016:012. 9 p, 2016. URL https://cds.cern.ch/record/2292553.

[16] Morad Aaboud et al. Measurement of the Higgs boson coupling properties in the $H \to ZZ^* \to 4\ell$ decay channel at $\sqrt{s} = 13$ TeV with the ATLAS detector. *JHEP*, 03:095, 2018. doi: 10.1007/JHEP03(2018)095.

[17] L. Brenner. Character profile of the higgs boson. 2017.

[18] C.D. Burgard. Measurement of $H \to W^{\pm}W^{\mp} \to l^{-}\bar{\nu}_{l}l'^{+}\nu_{l'}$. 2017.

[19] Max Baak, Stefan Gadatsch, Robert Harrington, and Wouter Verkerke. Interpolation between multi-dimensional histograms using a new non-linear moment morphing method. *Nucl. Instrum. Meth.*, A771:39–48, 2015. doi: 10.1016/j.nima.2014.10.033.

[20] A morphing technique for signal modelling in a multidimensional space of coupling parameters. (ATL-PHYS-PUB-2015-047), Nov 2015. URL https://cds.cern.ch/record/2066980.

[21] P. Artoisenet et al. A framework for Higgs characterisation. *JHEP*, 11, 2013. doi: 10.1007/JHEP11(2013)043.

[22] Georges Aad et al. Observation of a new particle in the search for the Standard Model Higgs boson with the ATLAS detector at the LHC. *Phys. Lett.*, B716:1–29, 2012. doi: 10.1016/j.physletb.2012.08.020.

[23] Serguei Chatrchyan et al. Observation of a new boson at a mass of 125 GeV with the CMS experiment at the LHC. *Phys. Lett.*, B716:30–61, 2012. doi: 10.1016/j.physletb.2012.08.021.

[24] Giampiero Esposito. An Introduction to quantum gravity. In *Section 6.7.17 of the EOLSS Encyclopedia by UNESCO*, 2011. URL `https://inspirehep.net/record/924147/files/arXiv:1108.3269.pdf`.

[25] James Bedford. An Introduction to String Theory. 2011.

[26] Dah-Wei Chiou. Loop Quantum Gravity. *Int. J. Mod. Phys.*, D24(01):1530005, 2014. doi: 10.1142/S0218271815300050.

[27] N. Fornengo. Dark matter overview. In *25th European Cosmic Ray Symposium (ECRS 2016) Turin, Italy, September 04-09, 2016*, 2016. URL `https://inspirehep.net/record/1507426/files/arXiv:1701.00119.pdf`.

[28] Farinaldo S. Queiroz. Dark Matter Overview: Collider, Direct and Indirect Detection Searches. In *Proceedings, 51st Rencontres de Moriond on Electroweak Interactions and Unified Theories: La Thuile, Italy, March 12-19, 2016*, pages 427–436. ARISF, ARISF, 2016. URL `https://inspirehep.net/record/1466249/files/arXiv:1605.08788.pdf`.

[29] Erik P. Verlinde. Emergent Gravity and the Dark Universe. *SciPost Phys.*, 2(3):016, 2017. doi: 10.21468/SciPostPhys.2.3.016.

[30] Yue-Yao Xu and Xin Zhang. Comparison of dark energy models after Planck 2015. *Eur. Phys. J.*, C76(11):588, 2016. doi: 10.1140/epjc/s10052-016-4446-5.

[31] R. Rattazzi. The path integral approach to quantum mechanics. URL `http://www.pd.infn.it/~feruglio/rattazzi.pdf`.

[32] M.A. Luty. Correlation functions and diagrams. URL `https://www.physics.umd.edu/courses/Phys851/Luty/notes/diagrams.pdf`.

[33] S.S. Seahra. Path integrals in quantum field theory. URL `http://www.math.unb.ca/~seahra/resources/notes/path_integrals.pdf`.

[34] A. Zee. *Quantum Field Theory in a Nutshell*. 2010.

[35] Denner A. Scherrer P. Böhm, M. and H. Joos. *Gauge Theories of the Strong and Electroweak Interaction*. 2001.

[36] Golowich E. Donoghue, J.F. and B.R. Holstein. *Dynamics of the Standard Model*. 2014.

[37] D. Griffiths. *Introduction to Elementary Particles*. 2004.

[38] M.D. Schwartz. *Quantum Field Theory and the Standard Model*. 2014.

[39] M. Szleper. The Higgs boson and the physics of WW scattering before and after Higgs discovery. 2014.

[40] C. Hughes. A brief discussion on effective field theories. URL `http://www.damtp.cam.ac.uk/user/ch558/pdf/EFT.pdf`.

[41] J. Brehmer. Higgs effective field theory. URL `http://www.thphys.uni-heidelberg.de/~gk_ppbsm/lib/exe/fetch.php?media=students:lectures:student_lecture_eft.pdf`.

[42] C. P. Burgess. Introduction to Effective Field Theory. *Ann. Rev. Nucl. Part. Sci.*, 57:329–362, 2007. doi: 10.1146/annurev.nucl.56.080805.140508.

[43] Nikolina Ilic. ATLAS and CMS Higgs Mass and Spin/CP Measurement. (ATL-PHYS-PROC-2015-159), Nov 2015. URL `https://cds.cern.ch/record/2109253`.

[44] Michael Dine. Naturalness Under Stress. *Ann. Rev. Nucl. Part. Sci.*, 65:43–62, 2015. doi: 10.1146/annurev-nucl-102014-022053.

[45] Durmus Demir. Naturalizing Gravity of the Quantum Fields, and the Hierarchy Problem. 2017.

[46] A. V. Gurskaya, M. V. Dolgopolov, and E. N. Rykova. Higgs bosons in standard model extensions. *Phys. Part. Nucl.*, 48(5):822–826, 2017. doi: 10.1134/S1063779617050215. [Fiz. Elem. Chast. Atom. Yadra48,no.5(2017)].

[47] Igor P. Ivanov. Building and testing models with extended Higgs sectors. *Prog. Part. Nucl. Phys.*, 95:160–208, 2017. doi: 10.1016/j.ppnp.2017.03.001.

[48] G. C. Branco, P. M. Ferreira, L. Lavoura, M. N. Rebelo, Marc Sher, and Joao P. Silva. Theory and phenomenology of two-Higgs-doublet models. *Phys. Rept.*, 516: 1–102, 2012. doi: 10.1016/j.physrep.2012.02.002.

[49] Abdelhak Djouadi, Adam Falkowski, Yann Mambrini, and Jeremie Quevillon. Direct Detection of Higgs-Portal Dark Matter at the LHC. *Eur. Phys. J.*, C73(6): 2455, 2013. doi: 10.1140/epjc/s10052-013-2455-1.

[50] Martin Hoferichter, Philipp Klos, Javier Menéndez, and Achim Schwenk. Improved limits for Higgs-portal dark matter from LHC searches. *Phys. Rev. Lett.*, 119(18): 181803, 2017. doi: 10.1103/PhysRevLett.119.181803.

[51] Roberto Contino. The Higgs as a Composite Nambu-Goldstone Boson. pages 235–306, 2011. doi: 10.1142/9789814327183_0005. URL `https://inspirehep.net/record/856065/files/arXiv:1005.4269.pdf`.

[52] Neil D. Christensen, Tao Han, and Shufang Su. MSSM Higgs Bosons at The LHC. *Phys. Rev.*, D85:115018, 2012. doi: 10.1103/PhysRevD.85.115018.

[53] Archil Kobakhidze and Matthew Talia. Supersymmetric Naturalness Beyond MSSM. 2018.

[54] ATLAS magnet system: Technical Design Report, 1. 1997. URL https://cds.cern.ch/record/338080.

[55] Aranzazu Ruiz-Martinez and ATLAS Collaboration. The Run-2 ATLAS Trigger System. (ATL-DAQ-PROC-2016-003), Feb 2016. URL https://cds.cern.ch/record/2133909.

[56] G Aad, M Ackers, F A Alberti, M Aleppo, G Alimonti, J Alonso, E C Anderssen, A Andreani, A Andreazza, J-F Arguin, K E Arms, D Barberis, M B Barbero, M Bazalova, R B Beccherle, K H Becks, P K Behera, F Bellina, J Beringer, K Bernardet, J B Biesiada, L Blanquart, J Boek, G R Boyd, P Breugnon, P Buchholz, B Butler, M Caccia, A C Capsoni, C Caso, D Cauz, M Cepeda, R Cereseto, M Cervetto, M L Chu, M Citterio, J C Clemens, Y C Coadou, M Cobal, A Coccaro, S Coelli, S Corréard, M Cristinziani, S Cuneo, S Dauria, M Dameri, G Darbo, S Dardin, B DeLotto, U De Sanctis, J B De Vivie De Regie, C del Papa, P Delpierre, B Di Girolamo, W Dietsche, F Djama, D Dobos, M Donega, J Dopke, K Einsweiler, A Eyring, D Fasching, L Feligioni, D Ferguson, W Fernando, P Fischer, M J Fisher, T Flick, G Gagliardi, E Galyaev, K K Gan, M García-Sciveres, N Garelli, G G Gariano, G G Gaycken, C Gemme, P Gerlach, M G D Gilchriese, M P Giordani, D Giugni, K W Glitza, C Gössling, T Golling, F Goozen, I Gorelov, G Gorfine, C Grah, H M Gray, I M Gregor, J Grosse-Knetter, K Grybel, P Gutíerrez, G D Hallewell, N Hartman, M Havranek, B Heinemann, T Henß, M R Hoeferkamp, D Hoffmann, M Holder, W Honerbach, C Horn, S Hou, G S Huang, F Huegging, E W Hughes, I Ibragimov, I Ilyashenko, M Imhaeuser, J M Izen, J Jackson, D Jana, R C Jared, P Jez, T Johnson, J Joseph, H Kagan, M Karagounis, R D Kass, M Keil, S Kersten, P Kind, J Klaiber-Lodewigs, L Klingbeil, R Klingenberg, A Korn, V V Kostyukhin, I Kostyukhina, O Krasel, H Krüger, K Krüger, J Kudlaty, T Kühl, O Kvasnicka, K Lantzsch, T Lari, S L Latorre, S C Lee, T Lenz, G Lenzen, J Lepidis, J Levêque, M Leyton, D Lopez Mateos, K F Loureiro, D Lüke, L Luisa, J Lys, R J Madaras, P Mättig, F M Manca, E Mandelli, M Marcisovsky, Z Marshall, G Martínez, L Masetti, M Maß, M Mathes, R McKay, G Meddeler, R Meera-Lebbai, C Meroni, J Metcalfe, W T Meyer, D W Miller, W Miller, S Montesano, M M Monti, P Morettini, J M Moss, T Mouthuy, P Nechaeva, W Ockenfels, G A Odino, M Olcese, B Osculati, F Parodi, A Pekedis, K Perez, I Peric, C Pizzorno, J Popule, R Post, F Ragusa, A M Rahimi, B Raith,

S Rajek, K Reeves, I Reisinger, J D Richardson, E I Rosenberg, L P Rossi, I Rottländer, A R Rovani, A Rozanov, O Runólfsson, E R Ruscino, A F Saavedra, F S Sabatini, M Saleem, S Sandvoss, B Sanny, L Santi, M I Scherzer, C Schiavi, A Schreiner, J Schultes, A Schwartzman, R Seibert, S C Seidel, H Severini, S Shanava, P Sícho, P Skubic, A C Smith, D S Smith, J Snow, T Stahl, T Stockmanns, S Strandberg, M Strauss, D Ta, F Tegenfeldt, P K Teng, R Ter-Antonian, J Thadome, T Tic, L Tomasek, M Tomasek, F Tomasi, K Toms, C Tran, J Treis, N Triplett, C Troncon, L Vacavant, S Vahsen, J Valenta, G Vegni, F Vernocchi, E Vigeolas, J Virzi, E Viscione, V Vrba, J Walbersloh, W Walkowiak, J Weber, T F Weber, J Weingarten, C Weldon, N Wermes, U Werthenbach, J S Wirth, R Witharm, B Witt, M Wittgen, J Wüstenfeld, R Wunstorf, J Wyckoff, W-M Yao, C Young, R Zaidan, M Zdrazil, F Zetti, J Zhong, M Ziolkowski, G Zizka, and M M Zoeller. ATLAS pixel detector electronics and sensors. *JINST*, 3:P07007, 2008. URL `https://cds.cern.ch/record/1119279`.

[57] ATLAS inner detector: Technical Design Report, 1. 1997. URL `https://cds.cern.ch/record/331063`.

[58] E. Abat et al. The ATLAS Transition Radiation Tracker (TRT) proportional drift tube: Design and performance. *JINST*, 3:P02013, 2008. doi: 10.1088/1748-0221/3/02/P02013.

[59] ATLAS liquid-argon calorimeter: Technical Design Report. 1996. URL `https://cds.cern.ch/record/331061`.

[60] Ringaile Placakyte. Parton Distribution Functions. In *Proceedings, 31st International Conference on Physics in collisions (PIC 2011): Vancouver, Canada, August 28-September 1, 2011*, 2011. URL `https://inspirehep.net/record/954990/files/arXiv:1111.5452.pdf`.

[61] F. Krauss, R. Kuhn, and G. Soff. AMEGIC++ 1.0: A Matrix element generator in C++. *JHEP*, 02:044, 2002. doi: 10.1088/1126-6708/2002/02/044.

[62] Tanju Gleisberg and Stefan Hoeche. Comix, a new matrix element generator. *JHEP*, 12:039, 2008. doi: 10.1088/1126-6708/2008/12/039.

[63] E. Boos, V. Bunichev, M. Dubinin, L. Dudko, V. Ilyin, A. Kryukov, V. Edneral, V. Savrin, A. Semenov, and A. Sherstnev. CompHEP 4.4: Automatic computations from Lagrangians to events. *Nucl. Instrum. Meth.*, A534:250–259, 2004. doi: 10.1016/j.nima.2004.07.096.

[64] Petros D. Draggiotis, Ronald H. P. Kleiss, and Costas G. Papadopoulos. Multijet production in hadron collisions. *Eur. Phys. J.*, C24:447–458, 2002. doi: 10.1007/s10052-002-0955-5.

[65] T. Stelzer and W. F. Long. Automatic generation of tree level helicity amplitudes. *Comput. Phys. Commun.*, 81:357–371, 1994. doi: 10.1016/0010-4655(94)90084-1.

[66] Mauro Moretti, Thorsten Ohl, and Jurgen Reuter. O'Mega: An Optimizing matrix element generator. pages 1981–2009, 2001.

[67] M. Bahr et al. Herwig++ Physics and Manual. *Eur. Phys. J.*, C58:639–707, 2008. doi: 10.1140/epjc/s10052-008-0798-9.

[68] Torbjörn Sjöstrand, Stefan Ask, Jesper R. Christiansen, Richard Corke, Nishita Desai, Philip Ilten, Stephen Mrenna, Stefan Prestel, Christine O. Rasmussen, and Peter Z. Skands. An Introduction to PYTHIA 8.2. *Comput. Phys. Commun.*, 191: 159–177, 2015. doi: 10.1016/j.cpc.2015.01.024.

[69] T. Gleisberg, Stefan. Hoeche, F. Krauss, M. Schonherr, S. Schumann, F. Siegert, and J. Winter. Event generation with SHERPA 1.1. *JHEP*, 02:007, 2009. doi: 10.1088/1126-6708/2009/02/007.

[70] Johannes Bellm et al. Herwig 7.0/Herwig++ 3.0 release note. *Eur. Phys. J.*, C76 (4):196, 2016. doi: 10.1140/epjc/s10052-016-4018-8.

[71] Torbjorn Sjostrand, Stephen Mrenna, and Peter Z. Skands. A Brief Introduction to PYTHIA 8.1. *Comput. Phys. Commun.*, 178:852–867, 2008. doi: 10.1016/j.cpc.2008.01.036.

[72] G. Aad et al. The ATLAS Simulation Infrastructure. *Eur. Phys. J.*, C70:823–874, 2010. doi: 10.1140/epjc/s10052-010-1429-9.

[73] Elzbieta Richter-Was, D Froidevaux, and Luc Poggioli. ATLFAST 2.0 a fast simulation package for ATLAS. Technical Report ATL-PHYS-98-131, CERN, Geneva, Nov 1998. URL `https://cds.cern.ch/record/683751`.

[74] E. Barberio et al. Fast simulation of electromagnetic showers in the ATLAS calorimeter: Frozen showers. *J. Phys. Conf. Ser.*, 160:012082, 2009. doi: 10.1088/1742-6596/160/1/012082.

[75] Federico Meloni. Primary vertex reconstruction with the ATLAS detector. Technical Report ATL-PHYS-PROC-2016-163. 12, CERN, Geneva, Oct 2016. URL `https://cds.cern.ch/record/2222390`.

[76] T. Cornelissen, M. Elsing, I. Gavrilenko, W. Liebig, E. Moyse, and A. Salzburger. The new ATLAS track reconstruction (NEWT). *J. Phys. Conf. Ser.*, 119:032014, 2008. doi: 10.1088/1742-6596/119/3/032014.

[77] R E Kwee. Minimum Bias Trigger in ATLAS. Technical Report ATL-DAQ-PROC-2010-055, CERN, Geneva, Dec 2010. URL `http://cds.cern.ch/record/1312194`.

[78] Jovan Mitrevski. Electron and Photon Reconstruction with the ATLAS Detector. *Nucl. Part. Phys. Proc.*, 273-275:2539–2541, 2016. doi: 10.1016/j.nuclphysbps.2015.09.452.

[79] Phillip George Hamnett. Performance of the photon reconstruction and identification in ATLAS. Aug 2015. URL `https://cds.cern.ch/record/2047801`.

[80] Electron identification measurements in ATLAS using $\sqrt{s} = 13$ TeV data with 50 ns bunch spacing. Technical Report ATL-PHYS-PUB-2015-041, CERN, Geneva, Sep 2015. URL `https://cds.cern.ch/record/2048202`.

[81] Georges Aad et al. Muon reconstruction performance of the ATLAS detector in proton–proton collision data at $\sqrt{s}$ =13 TeV. *Eur. Phys. J.*, C76(5):292, 2016. doi: 10.1140/epjc/s10052-016-4120-y.

[82] A. Hrynevich. ATLAS jet and missing energy reconstruction, calibration and performance in LHC Run-2. *JINST*, 12(06):C06038, 2017. doi: 10.1088/1748-0221/12/06/C06038.

[83] Felix Friedrich. Tau Lepton Reconstruction and Identification at ATLAS. 2012. doi: 10.1051/epjconf/20122812007. [EPJ Web Conf.28,2007(2012)].

[84] Performance of missing transverse momentum reconstruction for the ATLAS detector in the first proton-proton collisions at at $\sqrt{s}$= 13 TeV. Technical Report ATL-PHYS-PUB-2015-027, CERN, Geneva, Jul 2015. URL `https://cds.cern.ch/record/2037904`.

[85] Serguei Chatrchyan et al. Observation of a new boson with mass near 125 GeV in pp collisions at $\sqrt{s} = 7$ and 8 TeV. *JHEP*, 06:081, 2013. doi: 10.1007/JHEP06(2013)081.

[86] A. Nisati and G. Tonelli. The discovery of the Higgs boson at the Large Hadron Collider. *Riv. Nuovo Cim.*, 38(11):507–573, 2015. doi: 10.1393/ncr/i2015-10118-8.

[87] M. Aaboud et al. Evidence for the $H \to b\bar{b}$ decay with the ATLAS detector. *JHEP*, 12:024, 2017. doi: 10.1007/JHEP12(2017)024.

[88] Arun Kumar. Higgs boson measurements in WW, $\tau\tau$ and $\mu\mu$ channels with CMS. 2017. URL https://inspirehep.net/record/1630467/files/arXiv:1710.04424.pdf.

[89] Vardan Khachatryan et al. Constraints on the spin-parity and anomalous HVV couplings of the Higgs boson in proton collisions at 7 and 8 TeV. *Phys. Rev.*, D92 (1):012004, 2015. doi: 10.1103/PhysRevD.92.012004.

[90] M. Kado M. Carena, C. Grojean and V. Sharma (Particle Data Group). Status of higgs boson physics. URL http://pdg.lbl.gov/2017/reviews/rpp2017-rev-higgs-boson.pdf.

[91] Measurements of Higgs boson properties in the diphoton decay channel using 80 fb^{-1} of pp collision data at $\sqrt{s} = 13$ TeV with the ATLAS detector. Technical Report ATLAS-CONF-2018-028, CERN, Geneva, Jul 2018. URL https://cds.cern.ch/record/2628771.

[92] Combined measurement of differential and inclusive total cross sections in the $H \to \gamma\gamma$ and the $H \to ZZ^* \to 4\ell$ decay channels at $\sqrt{s} = 13$ TeV with the ATLAS detector. Technical Report ATLAS-CONF-2018-002, CERN, Geneva, Mar 2018. URL http://cds.cern.ch/record/2308390.

[93] Observation of $H \to b\bar{b}$ decays and VH production with the ATLAS detector. Technical Report ATLAS-CONF-2018-036, CERN, Geneva, Jul 2018. URL http://cds.cern.ch/record/2630338.

[94] Cross-section measurements of the Higgs boson decaying to a pair of tau leptons in proton–proton collisions at $\sqrt{s} = 13$ TeV with the ATLAS detector. Technical Report ATLAS-CONF-2018-021, CERN, Geneva, Jun 2018. URL http://cds.cern.ch/record/2621794.

[95] Ilaria Brivio and Michael Trott. The Standard Model as an Effective Field Theory. 2017.

[96] John Ellis, Christopher W. Murphy, Verónica Sanz, and Tevong You. Updated Global SMEFT Fit to Higgs, Diboson and Electroweak Data. *JHEP*, 06:146, 2018. doi: 10.1007/JHEP06(2018)146.

[97] Constraints on an effective Lagrangian from the combined $H \to ZZ^* \to 4\ell$ and $H \to \gamma\gamma$ channels using 36.1 fb^{-1} of $\sqrt{s} = 13$ TeV pp collision data collected with the ATLAS detector. Technical Report ATL-PHYS-PUB-2017-018, CERN, Geneva, Nov 2017. URL https://cds.cern.ch/record/2293084.

[98] Carlo Oleari. The POWHEG-BOX. *Nucl. Phys. Proc. Suppl.*, 205-206:36–41, 2010. doi: 10.1016/j.nuclphysbps.2010.08.016.

[99] Common analysis framework (caf). URL `https://atlas-caf.web.cern.ch/`.

[100] The fake factor method. URL `https://hep.uchicago.edu/~johnda/thesis/FakeFactorMethod.pdf`.

[101] Glen Cowan, Kyle Cranmer, Eilam Gross, and Ofer Vitells. Asymptotic formulae for likelihood-based tests of new physics. *Eur. Phys. J.*, C71:1554, 2011. doi: 10.1140/epjc/s10052-011-1554-0,10.1140/epjc/s10052-013-2501-z. [Erratum: Eur. Phys. J.C73,2501(2013)].

[102] Particle Data Group. Statistics review. URL `http://pdg.lbl.gov/2014/reviews/rpp2014-rev-statistics.pdf`.

[103] W. Verkerke and D. Kirkby. The RooFit toolkit for data modeling. *ArXiv Physics e-prints*, June 2003.